New Insights into High-T_c Superconductivity from Angle-Resolved Photoemission at Low Photon Energies

by

Nicholas Clark Plumb

B.A., Colorado College, 2002

A thesis submitted to the

Faculty of the Graduate School of the

University of Colorado in partial fulfillment

of the requirements for the degree of

Doctor of Philosophy

Department of Physics

2011

This thesis entitled:
New Insights into High-T_c Superconductivity from Angle-Resolved Photoemission at Low Photon Energies
written by Nicholas Clark Plumb
has been approved for the Department of Physics

Daniel S. Dessau

Asst. Prof. Kyle McElroy

Date

The final copy of this thesis has been examined by the signatories, and we find that both the content and the form meet acceptable presentation standards of scholarly work in the above mentioned discipline.

Plumb, Nicholas Clark (Ph.D., Physics)

New Insights into High-T_c Superconductivity from Angle-Resolved Photoemission at Low Photon Energies

Thesis directed by Prof. Daniel S. Dessau

Angle-resolved photoemission spectroscopy (ARPES) is one of the most direct and powerful probes for studying the physics of solids. ARPES takes a "snapshot" of electrons in momentum space (k-space) to reveal details of the dispersion relation $E(\boldsymbol{k})$, as well as information about the lifetimes of interacting quasiparticles. From this we learn not only where the electrons live, but also, if we are crafty, what they are doing. Beginning with work by our group in 2006 using a 6-eV laser, ARPES experiments have begun to make use of a new, low photon energy regime (roughly $h\nu$ = 6–9 eV). These low photon energies give drastic improvements in momentum resolution, photoelectron escape depths, and overall spectral sharpness. This has led to several important new findings in the intensively-studied problem of high-temperature superconductivity.

This thesis will focus on two of the latest results from our group using low-energy ARPES (LE-ARPES) to study the cuprate high-T_c superconductor $Bi_2Sr_2CaCu_2O_{8+\delta}$ (Bi2212). The first of these is an investigation into the nature of many-body interactions at a well-known energy scale ($\sim$ 60–70 meV) where the dispersion shows a large bend, or "kink". Using LE-ARPES measurements, the k-dependence of this kink is investigated in unprecedented detail. An attempt is then made to map the feature's k evolution into the scattering q-space of boson dispersions. In our analysis, the q-dispersion of the kink bears more resemblance to dispersive spin excitations than phonons — a surprising finding in light of previous evidence that the the kink originates from interactions with phonons. However, phonons cannot be ruled out, and the results may hint that both types of interactions contribute to the main nodal kink.

A second result is the discovery of a new ultralow ($<$ 10 meV) energy scale for electron interactions, corresponding to a distinct, smaller kink in the electron dispersion. The temperature

and doping dependence of this feature show not only that it turns on near T_c — signalling a possible relation to the mechanism of high-T_c superconductivity — but also that it leads to a subtle breakdown of the so-called "universal" Fermi velocity v_F along nodes of the anisotropic superconducting gap. Moreover, v_F is found to depend quite strongly on temperature, which may be an important factor in the physics of cuprates.

Dedication

To Bridget, who has true grace

Acknowledgements

The thesis of a previous student from our group begins with a quote from the sci-fi sage Yoda: "Do, or do not. There is no try" [Gromko, 2001]. I recall a profound sinking feeling when I first read this, because I entered graduate school with nearly the opposite mindset, which can be summed up as: "Go ahead and try, but just remember there's no shame if you come to find out that you can't hack it as a physicist." To me grad school amounted to a commitment to a multi-year experiment in probing the outer limits of my intellect and determination. I viewed failure as a an undesirable but quite possible outcome. In hindsight, it is quite clear to me that no one should be able to survive the challenges of earning a Ph.D. while maintaining such an attitude. Thus, I am here despite myself, and it is largely due to the assistance, advice, encouragement, and love of many people. They believed in me even when my self-confidence wavered.

My advisor, Dan Dessau, is one of these people. In all likelihood, I never would have gone to grad school in physics (and certainly would not have gotten into such a prestigious program) were it not for Dan. He has always shown utter confidence in my talents and potential, and this has fostered a deep mutual trust and respect. He is a mentor in the most profound sense of the word: someone who gives great advice to his students, who keeps them on track, who supports them when they need it, and who guides by example. Dan has rewired the synapses of my brain. He has shown me what it truly means to have "physical intuition" and to think like a physicist. He has made me better in Science and in Life.

My wife, Bridget, to whom this thesis is dedicated, is another such believer. I met her shortly before starting grad school. As the relationship progressed, I recall warning her that her timing was

really bad — not for me, but for her. The first two years of classes are notoriously time-consuming, but she insisted on hanging around anyway. I'm glad she did. My life is richer for having Bridget in it. She is the truest and most steadfast companion I have (will) ever had (have). She is a wellspring of joy, comfort, contentment, and beauty. And I promise, dear, there will be a honeymoon someday.

I of course owe a huge debt of thanks to my family — especially my parents, Preston and Judy, and my siblings, "Cinco," Kristen, and Nathan. My family did everything in its power to foster my early interest in science. Mom and Dad bankrolled the R&D of my childhood: microscopes, chemistry sets, encyclopedias, model rockets (actually, Cinco bought me the first one), erector sets, LEGOs, electronics kits, pinewood derby cars, subscriptions to Popular Science, summertime "College for Kids," the list goes on. At every juncture my parents went above and beyond the call of duty. Here's just one example: In sixth grade I wanted to do the Mendel experiment for the science fair. Bear in mind this is the experiment that involves cross-breeding fruit flies to test the inheritance of dominant and recessive genes. Mom made contact with a lab at San Diego State, somehow convinced them to loan us equipment (including a very nice Bausch & Lomb binocular microscope), and then helped her son raise a couple generations of fruit flies in his bedroom over the next several weeks. The point is there are perfectly wholesome, loving parents who would never go to such lengths for their kids. The fact that mine did really speaks to their love and devotion to their children.

I must thank my coworkers in the Dessau lab. Jake Koralek (now at UC Berkeley) built the first laser-based ARPES system, ushering in a new era in photoemission and thereby setting the stage for all the work presented in this thesis. Fraser Douglas (now at Intel) performed the isotope experiments that are foundational to my own work with isotope samples. Ted Reber has been focusing on cuprate analysis concurrent with my own studies. It was actually Ted who collected the data that is the foundation of Chapter 4. As our studies have progressed alongside each other, my work has benefitted immensely from the insights acquired by Ted. I only hope he can say the same about me. Zhe "Joe" Sun was a student and later a postdoc in our group, who just left for a position at the University of Science and Technology of China. Joe is a close approximation to

a living, breathing encyclopedia of ARPES on correlated electron systems. Qiang "Quinn" Wang is an enormously talented physicist, and it has been a pleasure to progress through grad school alongside him. Justin Griffith is our in-house mechanical designer and all-around lab jock. He is utterly indispensable and a great guy to boot. More recent members of our group — Yue "Scott" Cao, Steve Parham, Sunita Kannan, and Justin Waugh — are all outstanding, and it has been fun to work with them.

I have benefited from some excellent outside collaborations and assistance. In addition to the laser-based system in Colorado, ARPES data in this thesis comes from beamline 5-4 at Stanford Synchrotron Radiation Lightsource (SSRL) and beamline 9A of the HiSOR synchrotron of the Hiroshima Synchrotron Radiation Center (HSRC). Samples used in my work have come from Yoshihiro Aiura, Hiroshi Eisaki, and Yoshiyuki Yoshida at the National Institute of Advanced Industrial Science and Technology (AIST) in Tsukuba, Japan. Genda Gu at Brookhaven National Laboratory has also prepared very high-quality samples for us. On my visits to the HiSOR, I have had the wonderful opportunity to work closely with Aiura, Hideaki Iwasawa, Koji Sato (now at Hitachi), Kenya Shimada, and Masashi Arita. I am especially indebted to Aiura and Iwasawa, who are not only great scientific collaborators but also very kind and generous hosts. They have always made me feel welcome and comfortable in Japan. Arigatou gozaimasu.

Outside of formal collaborations, I have also enjoyed many helpful and informative conversations with other researchers in the field of high-T_c superconductivity. I am especially grateful to Tom Devereaux, Steve Johnston, Sasha Balatsky, and two of my Ph.D. committee members, Dmitry Reznik and Kyle McElroy.

Lastly, I would like to thank my dear friend Jason Underwood, who used to work across the hall from our lab but currently is down the street as a NRC postdoctoral fellow at NIST. He introduced me (via his wife, Margie) to many other good friends, and he is one of the forces that helped keep me (relatively) sane these past few years. To paraphrase my brother, What are the odds of finding two physicists who both enjoy the band Faraquet? Indeed.

To everyone, thanks.

Contents

Chapter

1 Introduction 1

2 The Technique of Angle-Resolved Photoemission Spectroscopy 4

2.1 Introduction 4

2.2 Energetics of the photoemission process 5

2.3 Angle-resolved photoemission 6

2.4 Modern ARPES spectrometers 10

2.4.1 Hemispherical analyzer 11

2.4.2 Electron lens 13

2.4.3 Detector 15

2.4.4 Light source 17

2.4.5 Vacuum chamber, surface preparation, and cryostat manipulator 19

2.5 Theory of the spectral function 20

2.6 Interpretation and analysis of ARPES data 23

2.6.1 Momentum and energy distribution curves 23

2.6.2 Many-body self-energy 24

2.6.3 Matrix elements 29

2.7 ARPES in the low photon energy regime 31

2.7.1 Momentum and energy resolution 32

2.7.2 Improved bulk material sensitivity 33
2.7.3 The sudden approximation and the validity of LE-ARPES 35

3 High-Temperature Superconductivity in Layered Cuprates 38
3.1 Introduction 38
3.2 Conventional superconductivity: The BCS theory 40
3.3 The cuprate high-T_c superconductors 43
3.3.1 Structure 43
3.3.2 Phase diagram 44
3.3.3 Fermi surface 47
3.3.4 d-wave gap 50
3.3.5 Energy scales and kinks 51

4 Momentum Dependence of the Main Nodal Kink 55
4.1 Introduction 55
4.2 The effective self-energy in the nodal region 57
4.2.1 Experimental 57
4.2.2 k-space evolution of the self-energy 57
4.3 Electron-boson interactions 61
4.3.1 Mapping the interactions in q-space 61
4.4 Discussion 69

5 A New Energy Scale for Interactions: ~ 10 meV 75
5.1 Introduction 75
5.2 Observing the nodal kink near 10 meV 76
5.2.1 Experimental 76
5.2.2 Direct observation of the 10-meV kink 78
5.2.3 Dispersion measurement distortions due to resolution 80

5.2.4 Deconvolution and the Richardson-Lucy Technique 83
5.2.5 Full temperature dependence of the kink behavior 85
5.3 Possible origins 87
5.3.1 Acoustic phonon mode coupling 88
5.3.2 *c*-axis optical phonons 90
5.3.3 Backscattering in a 2D Fermi liquid 91
5.3.4 Ruled out 93
5.4 Breaking the universal Fermi velocity 95
5.5 Recent developments and future directions of study 97

6 Summary and discussion 100

Bibliography 103

Appendix

A Electron-boson interactions: Kink energy location in the presence of an anisotropic gap 120

B Simulating the effects of energy resolution on the measured v_F 124

Figures

Figure

2.1 Energy schematic of the photoemission process 7

2.2 Momentum components of the photoelectron 9

2.3 Schematic of a hemispherical ARPES analyzer 12

2.4 Electron trajectories through an electron lens operating in angular mode 14

2.5 The ARPES spectral function in an interacting system. 22

2.6 Momentum and energy distribution curves 25

2.7 Self-energy in ARPES spectra 27

2.8 Symmetry considerations of the matrix elements 30

2.9 Comparison of ARPES from Bi2212 at $h\nu = 6$ eV, 28 eV, and 52 eV 32

2.10 Comparison of EDCs and MDCs from Bi2212 at $h\nu = 6$ eV, 28 eV, and 52 eV 34

2.11 "Universal curve" of mean free paths of electrons in solids 35

3.1 Timeline of the progression of T_c 40

3.2 BCS superconducting gap in the single-particle excitation spectrum 42

3.3 Primitive unit cells of the Bi-based family of cuprates 44

3.4 Generic phase diagram of the high-T_c cuprates 46

3.5 Sketch of the generic cuprate Fermi surface 47

3.6 Fermi surface complications in cuprates 49

3.7 d-wave symmetry of the superconducting gap 50

3.8 Large nodal kink near 60–70 meV as seen in Bi2212 by LE-ARPES 53
3.9 Antinodal kink at the 30–40 meV energy scale 54

4.1 Momentum evolution of the nodal dispersion in Bi2212 58
4.2 Momentum dependence of $\Sigma_{\text{eff}}(\omega)$ in the nodal region of Bi2212 59
4.3 Boson energies under assumed scattering scenarios 63
4.4 Calculations of electron-phonon matrix elements 65
4.5 q-space dispersions of Ω_{kink} and Ω^*_{boson} 67
4.6 Evidence for horizontal/vertical scattering by the Cu-O bond-stretching phonon . . . 68
4.7 INS measurements of the "hourglass" dispersion of spin fluctuations in Bi2212 . . . 70
4.8 Momentum-resolved view of the magnetic resonance in YBCO 71
4.9 Comparison between Σ'_{eff} and the magnetic resonance peak in Bi2212 72
4.10 Calculations of electron-phonon coupling around the Fermi surface 74

5.1 LE-ARPES data at the node in Bi2212 78
5.2 Direct observation of the nodal 10-meV kink at $T = 50$ K 79
5.3 10-meV kink seen in the temperature dependence of the nodal dispersion 81
5.4 Understanding the resolution effect in MDC fitting 82
5.5 Richardson-Lucy deconvolution applied to ARPES data 85
5.6 Temperature and doping dependence of low-energy band velocities and kink strength 86
5.7 Temperature dependence of $\Sigma'(E)$ of the 10-meV kink 87
5.8 Examples of allowed electron-boson scattering vectors for the 10-meV kink 88
5.9 Evidence for acoustic phonon coupling as a possible origin of the 10-meV kink 90
5.10 Low-energy A_{1g} mode in Bi2212. 92
5.11 Lowest-order Feynman diagram for electron-electron scattering 94
5.12 Earlier claim of a universal nodal Fermi velocity 96

A.1 Simple picture for the location of the ARPES kink 122

A.2 ARPES kink location in the presence of an anisotropic gap 123

B.1 Simulations of energy resolution effects on v_F 125

Chapter 1

Introduction

Angle-resolved photoemission (ARPES) is a technique that exploits the photoelectric effect in order to gain information about the electronic structures of materials. By mapping the kinetic energies and emission angles of the photoemitted electrons, the electron dispersion (energy-vs.-momentum) relations can be obtained. The features of the dispersions contain information about all the complicated many-body interactions of the system.

The energy and momentum resolution of ARPES has recently been substantially improved thanks to the development of systems using low-energy photons (6–9 eV). This low-energy ARPES (LE-ARPES) was first performed using lasers [Koralek et al., 2006], and it is rapidly growing in popularity and now employs a variety of additional lightsources. Along with ultrahigh resolution, the low photon energy regime reduces spectral background and markedly improves the bulk material sensitivity of the probe. As a result, LE-ARPES is capable of obtaining spectra that are close to intrinsic and which reveal new, ultrafine details of the interacting electrons in solids.

In this thesis we will explore the use of LE-ARPES at low photon energies to study $Bi_2Sr_2CaCu_2O_{8+\delta}$ (Bi2212), which, as a member of the cuprate family of high-temperature (high-T_c) superconductors, is a system of enormous theoretical and practical importance. An understanding of the high-T_c mechanism could foreseeably pave the way to engineering room-temperature superconductors, as well as give new insights into other related systems of interest. The unique ability of ARPES to probe the interactions experienced by electrons as a function of both energy and momentum makes it an ideal tool to uncover the origins of high-T_c superconductivity. In par-

ticular, ARPES reveals electron dispersion anomalies ("kinks") which signal specific energy scales where interactions are happening. Presumably certain kinks are related to the forces that drive — or perhaps compete with — superconductivity.

ARPES has already extensively studied many aspects of the electronic structure of Bi2212 and of cuprates in general. Over the last 20 years or so, conventional ARPES has acquired a vast amount of information about these materials. Still, the advent of LE-ARPES has in many respects leap-frogged higher-energy ARPES and quickly made many discoveries that were virtually unattainable by previous experiments. The work presented here will detail some of the new insights into the physics of high-T_c cuprates made possible by LE-ARPES — results which highlight the tremendous power of the technique, and which will hopefully be of some use in the quest to understand high-temperature superconductivity.

Chapter 2 presents a broad overview of ARPES covering the theory and technology behind the experiment. The meaning of the ARPES spectral function will be discussed, as well as how the data can be analyzed to extract signatures of many-body interactions. LE-ARPES will be introduced, and we will describe its many technical advantages and the reasons for them.

Chapter 3 begins with a very brief introduction to conventional and high-T_c superconductivity and overviews relevant aspects of cuprates that will be of importance in this thesis — e.g., the Fermi surface, the phase diagram, and the d-wave superconducting gap. Particular attention is paid to various interaction energy scales that have been identified by the existence of ARPES dispersion kinks. The detailed investigation of these anomalies makes up the bulk of the remainder of this thesis.

Chapter 4 investigates the detailed momentum dependence of a large and well-known dispersion anomaly along the "nodal" $(0,0)$–(π,π) line. Nominally located about 60–70 meV below E_F, we reveal that this feature's energy location smoothly evolves in momentum space while its strength intensifies dramatically in certain regions. These observations are interpreted in the context of some simple assumptions about the scattering of electrons due to interactions with bosons. In certain respects the results of the analysis are qualitatively consistent with interactions due to

dispersive spin excitations. However, the role of phonons cannot be ruled out. The findings suggest the possibility that both phonons and spin fluctuations contribute to the main nodal kink, yet they also highlight the difficulties inherent to inferring the underlying interactions from ARPES data in cuprates.

Chapter 5 describes the recent discovery of a very low-energy electronic dispersion feature, just 10 meV or so below the Fermi energy. The observation of this low-energy kink would have been virtually impossible without the resolution of LE-ARPES. Studying different dopings, we find that the kink has an onset that appears to be related to T_c. The resulting strong temperature dependence of the Fermi velocity has implications for previous notions about the insensitivity of the nodal dispersion to changes in doping. Some theories of the kink's origin will be discussed.

Finally, the findings of chapters 4 and 5 will be summarized in chapter 6.

Chapter 2

The Technique of Angle-Resolved Photoemission Spectroscopy

2.1 Introduction

Neglecting interactions, non-core-level electrons in a solid can be completely characterized by just three parameters: energy, momentum, and spin. As will be discussed later, in an interacting picture, the electrons can be cast in terms of "dressed" composite particles which acquire an additional property: lifetime. Angle-resolved photoemission spectroscopy (ARPES) is unique among materials science probes in that it is in principle capable of measuring all[1] of these properties directly and simultaneously. This makes ARPES one of the most powerful experimental techniques available to condensed matter physicists.

The bulk of this chapter attempts to draw a broad overview of ARPES, covering the basic physics and technology behind the technique, as well as the theory, meaning, and interpretation of the acquired spectra. We will conclude with a discussion of the emerging and powerful subtechnique of low photon energy ARPES (LE-ARPES), where "low" means roughly 6–9 eV. LE-ARPES is the central experimental probe employed in this thesis. Compared with more traditional photon energies ($\sim$ 20–100 eV), vast improvements in momentum and energy resolution and overall spectral sharpness are possible in the low-energy regime. Moreover, LE-ARPES ejects electronic states from deeper within the sample than conventional ARPES, which is typically regarded as a

[1] While an ARPES system can be configured with a spin detector (e.g., a so-called Mott detector), spin resolution comes at the expense of a huge fraction of the signal (almost all of it, in fact), which, naturally, is disadvantageous for high-resolution studies of the remaining parameters that characterize the electrons. Hence spin-resolved ARPES is not used in the work presented here. For the curious, a review of spin-ARPES has been written by P. D. Johnson [Johnson, 1997].

surface probe.

While discussing ARPES, there will be a number of opportunities to point out that while the technique is useful for the study of materials ranging from the simple to the complex, it is especially suited to the study of high-T_c cuprates. Or, rather, it might be better to say that the cuprates are especially suited to ARPES. As we shall discuss shortly, the quasi-2D nature of layered cuprates greatly simplifies their analysis. Additionally, these materials can be cleaved in vacuum (certainly some more easily than others) to reveal clean, smooth surfaces, and this property greatly improves the overall quality of the spectra that can be obtained.

Photoemission in primitive forms has existed for roughly a century, and ARPES specifically has been around since at least the 1970s [Smith and Kevan, 1992]. Inevitably, it is impossible, to cover the full breadth of such a mature experimental technique. Further reading can be found in a number of excellent books, reviews, and articles [Inglesfield and Plummer, 1992,Louie, 1992,Hüfner et al., 1999,Hüfner, 2003,Damascelli et al., 2003,Damascelli, 2004,Reinert and Hüfner, 2005,Reinert and Hüfner, 2007].

2.2 Energetics of the photoemission process

When short-wavelength light (beginning in the ultraviolet) strikes a metal, electrons are ejected. If the wavelength of the light is too long, however, nothing happens. Albert Einstein's explanation of this phenomenon was largely responsible for his 1921 Nobel Prize in Physics. The success of his theory marked a major milestone in the history of quantum mechanics. By now, however, quantum mechanics is so foundational to modern physics that the essence of the photoelectric effect seems downright trivial to contemporary physicists: (i) The light is quantized into photons whose energies depend on the wavelength; (ii) an electron can absorb a photon and acquire its energy; (iii) if the combined energy of the electron and photon is high enough, the electron can escape from the material. The kinetic energy of the ejected electron is simply

$$E_{\text{kin}} = E_i + h\nu - (E_F + \Phi) \tag{2.1}$$

where E_i is the initial energy of the electron in the solid, E_F is the Fermi level, $h\nu$ is the photon energy, and Φ is the work function of the material — the energy required to remove the electron with $E_i = E_F$ infinitely far from the sample. The quantity $E_F + \Phi$ is referred to as the vacuum level E_{vac}. Photoemission will occur for electrons excited above this energy. Values of Φ are material-dependent but for the most part fall within a small range, about 4–5 eV [Kittel, 1996], setting a lower limit on the photon energies capable of inducing photoemission. E_F and Φ are determined empirically from ARPES. The kinetic energy corresponding to E_F is established by observing the kinetic energy of the Fermi edge from, e.g., a polycrystalline gold sample. Φ, meanwhile, can be found by optimizing its value to give the correct periodicity of dispersion features — e.g., the periodicity of multiple Brillouin zones.

The spectrum of E_i corresponds to the density of states arising from the band structure and core levels of the material. Electrons fill these states obeying the Pauli exclusion principle, with the highest occupied state at $T = 0$ being E_F.[2] A schematic energy diagram of the photoexcitation process is shown in Fig. 2.1. The measurement of the number of emitted electrons as a function of kinetic energy, $I(E)$, depicted in the upper-right set of axes, constitutes photoemission spectroscopy (PES), sans the "angle-resolved" part.

2.3 Angle-resolved photoemission

The addition of angular resolution to PES allows the emission angles of an electron to be mapped to its crystal momentum states $\boldsymbol{k}$. As an electron leaves the sample, its momentum parallel to the surface, $\boldsymbol{k}_{\parallel}$, is conserved, while a portion of its perpendicular momentum component, $\boldsymbol{k}_{\perp}$, is lost to overcoming the sample work function. The total momentum of the emitted electron outside the sample is

$$|\boldsymbol{p}| = \sqrt{2mE_{\mathrm{kin}}} \tag{2.2}$$

[2] In the limit $E_i \to E_F$, $E_{\mathrm{kin}}^{\mathrm{max}} = h\nu - \Phi$. This is, strictly speaking, what Einstein described [Reinert and Hüfner, 2005].

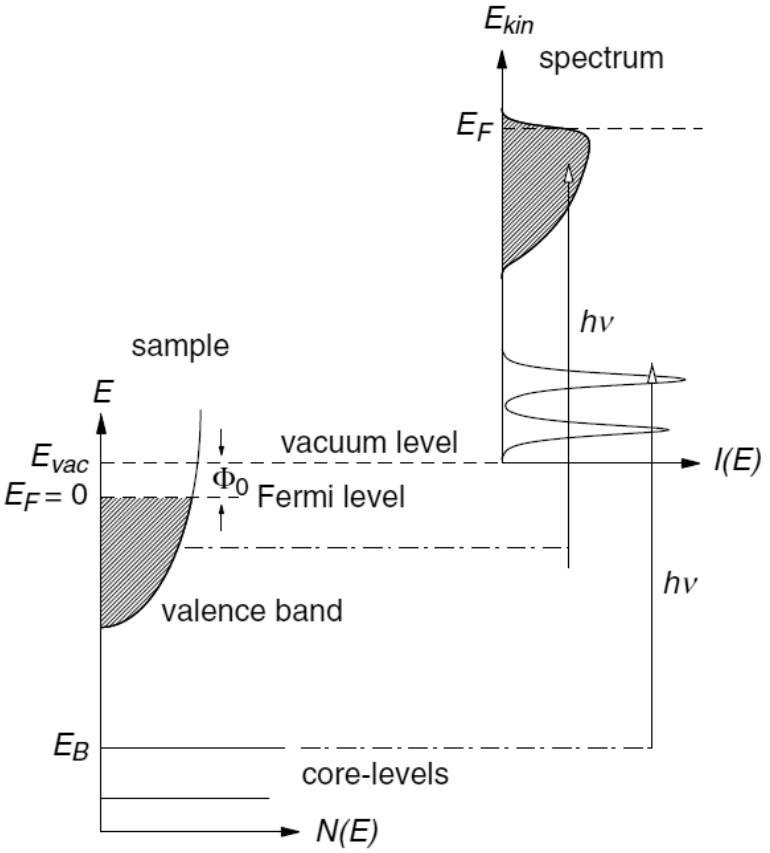

Figure 2.1: Energy schematic of the photoemission process. Electrons with binding energies E_i are excited by monochromatic photons with energy $h\nu$. If $E_i + h\nu > E_F + \Phi$, then they are emitted from the sample with kinetic energy given by (2.1). The example of a core level state with $E_i = E_B$ is highlighted. Measuring the spectrum of emitted electrons $I(E)$ constitutes (non-angle-resolved) photoemission spectroscopy (PES). $I(E)$ is intimately related to the intrinsic electron density spectrum $N(E)$, though it is in general not an exact image of $N(E)$ due to broadening and matrix element effects, which will be discussed. From [Reinert and Hüfner, 2005].

and its momentum parallel to the surface is

$$|\boldsymbol{p}_{\|}| = |\boldsymbol{k}_{\|}| = \sqrt{2mE_{\mathrm{kin}}/\hbar^2}\sin\alpha \tag{2.3}$$

where α is the angle between the surface normal and ejected photoelectron. The emission angle and conservation of $\boldsymbol{k}_{\|}$ are depicted in Fig. 2.2(a).

As it stands, Eq. (2.2) is not very practical; it is necessary to know the components of $\boldsymbol{k}_{\|}$ in

the sample coordinates system. In a typical ARPES experimental setup, the sample can be tilted in two dimensions by coupled orthogonal rotational stages θ and ϕ, allowing the experimenter to choose the particular $\boldsymbol{k}_{\|}$ pointing into the analyzer. (Some setups include a third angle, η, allowing in-plane rotation of the sample, which merely spins the orientation of the Brillouin zone and does not otherwise affect the calculation of momentum components in units of Å^{-1}.) To compute the components of $\boldsymbol{k}_{\|}$, it is easiest to consider an equivalent problem, where instead of rotating the sample by (θ, ϕ), the momentum vector $\boldsymbol{p}$ of the detected electron — which by definition always points to the analyzer entrance — is rotated by $(-\theta, -\phi)$. Suppose that the geometry is defined such that for $\theta = \phi = 0$, the sample surface is normal to the analyzer along the z axis (i.e., $\boldsymbol{p} = p\hat{\boldsymbol{z}}$). θ is defined as the polar angle from the z axis, and ϕ is the azimuthal angle in the $y-z$ plane. The geometry is illustrated in Fig. 2.2(b). $\boldsymbol{p}$ is transformed to $\boldsymbol{p'}$ under rotation via

$$\boldsymbol{p'} = R_x(-\phi)R_y(-\theta)\boldsymbol{p} \tag{2.4}$$

where

$$\begin{gathered} R_x(\phi) = \begin{pmatrix} 1 & 0 & 0 \\ 0 & \cos\phi & \sin\phi \\ 0 & -\sin\phi & \cos\phi \end{pmatrix}, \; R_y(\theta) = \begin{pmatrix} \cos\theta & 0 & -\sin\theta \\ 0 & 1 & 0 \\ \sin\theta & 0 & \cos\theta \end{pmatrix}, \\ \text{and } \boldsymbol{p} = \tfrac{\sqrt{2mE_{\text{kin}}}}{\hbar} \begin{pmatrix} 0 \\ 0 \\ 1 \end{pmatrix} \end{gathered} \tag{2.5}$$

Keeping in mind $\boldsymbol{p}_{\|} = \boldsymbol{k}_{\|}$, the surface parallel momentum components of $\boldsymbol{p}$ are thus:

$$\begin{aligned} k_x &= \sqrt{2mE_{\text{kin}}/\hbar^2}\cos\theta\sin\phi, \\ k_y &= -\sqrt{2mE_{\text{kin}}/\hbar^2}\sin\theta. \end{aligned} \tag{2.6}$$

While $\boldsymbol{k}_{\|}$ is obtained directly by ARPES in "one shot" as a result of the conservation of parallel momentum, the determination of $\boldsymbol{k}_{\perp}$ is far less straightforward. The problem is essentially that $\boldsymbol{k}_{\perp}$ depends on the details of the band structure at the final state energy E_f of the photoexcited electron, which is not known a priori. Some techniques have been developed for absolute determination

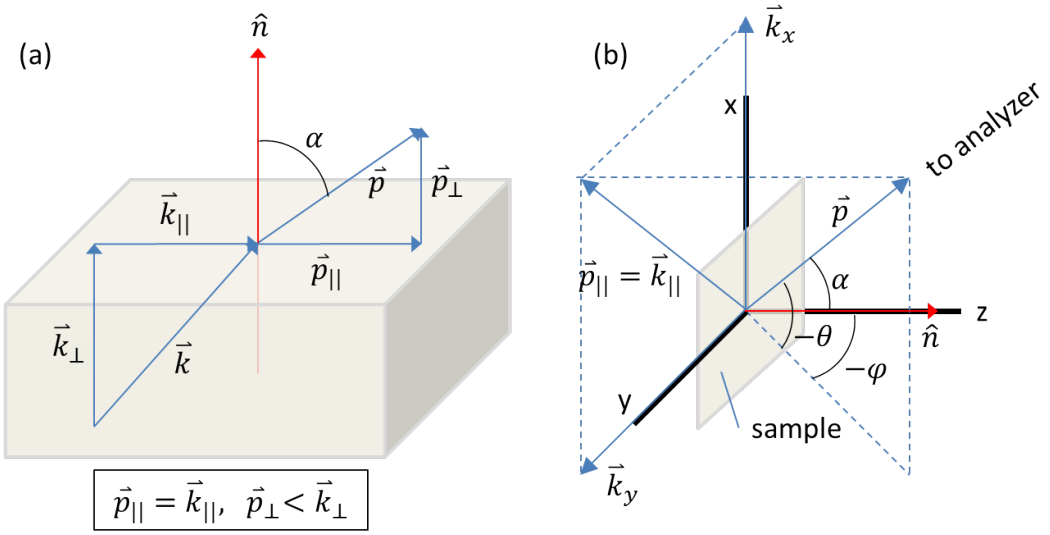

Figure 2.2: Momentum components of the photoelectron. (a) Conservation of parallel momentum as the photoelectron leaves the sample. $\boldsymbol{k}$ and $\boldsymbol{p}$ are the momenta of the photoexcited electron inside and outside the sample, respectively. α is the angle with the surface normal. (b) Geometry for computing the components of $\boldsymbol{k}_{||}$ as described in the text. Rotating the sample by polar angle θ and azimuthal ϕ corresponds to rotating the vector pointing to the analyzer by $-\theta$ and $-\phi$. At $\theta = \phi = 0$ the sample is set to be normal to the analyzer along the z axis. The components $\boldsymbol{k_x}$ and $\boldsymbol{k_y}$ of the total surface-parallel momentum $\boldsymbol{k}_{||}$ are found from Eq. 2.6.

of $\boldsymbol{k}_\perp$ (e.g., [Strocov et al., 1997]). Still, the workhorse equation for studying $\boldsymbol{k}_\perp$ is based on the assumption that the final states are free-electron-like (i.e., have parabolic dispersion). The kinetic energy of the excited electron inside the sample is $E_{\text{kin}}^{\text{sample}} = E_f - E_0$, where E_0 is the bottom of the valence band. Assuming free-electron final states, $E_f(\boldsymbol{k}) = \hbar^2\boldsymbol{k}^2/(2m) + E_0 = \hbar^2(\boldsymbol{k}_{||}^2 + \boldsymbol{k}_\perp^2)/(2m) + E_0$. By noting $E_F = E_{\text{kin}} + \Phi$ and combining with Eq. 2.3, the perpendicular momentum is

$$k_\perp = \sqrt{2m(E_f - E_0)/\hbar^2} - k_{||} = \sqrt{2m\left(E_{\text{kin}}\cos^2\alpha + V_0\right)/\hbar^2} \tag{2.7}$$

where $V_0 = E_F + \Phi - E_0$ is referred to as the "inner potential". A common trick for determining V_0, and hence $\boldsymbol{k}_\perp$, is to scan through $h\nu$ to probe the periodicity of $E(\boldsymbol{k})$ over multiple Brillouin

zones. V_0 can then be determined by a fit to this periodicity.

Though it has been included here for completeness, $\boldsymbol{k}_\perp$ will not factor into this thesis in any significant way. The reason is that the Brillouin zone of cuprate superconductors, whose unifying structural components are layered CuO_2 sheets, may essentially be regarded as two-dimensional. This greatly simplifies the study of cuprates by ARPES, since it more-or-less eliminates the $\boldsymbol{k}_\perp$ parameter space from the experiments. Cuprates, it turns out, are uncommonly suited to probing via ARPES.

As a final parting point on the topic of angle-to-$\boldsymbol{k}$ mapping in ARPES, notice that the photon momentum has been left out of the above equations. This is intentional; Photon momentum is negligible in the present work, and indeed in most ARPES experiments. For example, for a fairly conventional photon energy of $h\nu = 20$ eV, photon momentum is just 0.01 Å^{-1}. In cuprates, where the tetragonal lattice constant in the a-b plane is around $a = 3.8$ Å, this photon momentum amounts to merely 0.01 π/a (0.5% of the full $2\pi/a$-wide Brillouin zone). For the low photon energies typically used in this thesis, the photon momentum is obviously even smaller – e.g., just 0.2% of the cuprate Brillouin zone for $h\nu = 7$ eV. Photon momentum eventually becomes non-negligible for very high photon energies. This is the case in soft X-ray ARPES performed at specialized synchrotron beamlines whose photon energies extend well into the keV range [Saitoh et al., 2000, Strocov et al., 2010].

2.4 Modern ARPES spectrometers

From a technology standpoint, ARPES today bears little resemblance to photoemission spectroscopy's earliest implementations. Various crude means of angular resolution have long existed [Smith and Kevan, 1992], but the term ARPES nowadays connotes something far more powerful — a multiplexing probe that can truly "see" in two dimensions (E and k) simultaneously, on a video monitor, right before our very eyes. This section overviews the instrumentation that makes it possible.

2.4.1 Hemispherical analyzer

Modern ARPES experiments typically employ one of two types of analyzers: hemispherical or time-of-flight (TOF). The two analyzer configurations use essentially the same electron lens technology to obtain angular resolution. However, hemispherical analyzers achieve energy resolution via curved capacitor plates, whereas TOFs determine the electrons' kinetic energies by discerning the time it takes for an electron to travel from the sample to the detector (requiring a pulsed light source). This section will focus on hemispherical analyzers, which are sometimes referred to as hemispherical deflector analyzers (HDAs). Currently HDAs are far more common than TOFs, and state-of-the-art instruments have claimed energy resolution in the sub-meV range [Kiss et al., 2005], as well as angular resolution on the order of 0.1° [VG Scienta AB, 2009]. All of the data presented in this thesis was collected with hemispherical analyzers [Scienta SES-2002 and R4000 models (VG Scienta)].

A cross section of a generic HDA is shown in Fig. 2.3. The analyzer consists of two concentric metal hemispheres, the space between them forming a channel for the traveling photoelectrons. A narrow slit aligned out of the page is positioned at the entrance to this channel, and a 2D electron detector is at the exit. The incoming photoelectrons are (ideally) collimated and normal to the entrance plane. A net positive voltage applied to the inner hemisphere sets up a $1/r$ potential (neglecting fringe fields), and hence photoelectrons entering through the slit travel along Keplerian (i.e., elliptical) orbits [Zouros and Benis, 2002]. There is a particular electron kinetic energy, called the pass energy E_p, at which the orbit will actually be circular along the central radius r_0. This energy is set by the hemisphere voltages according to $E_p = (r_1V_1 - r_2V_2)/[2(r_2 - r_1)]$, where r_1 and r_2 are the radii of the inner and outer hemispheres, respectively, and V_1 and V_2 are the corresponding voltages on the hemispheres. Electrons will arrive at the detector at radii r according to $r = r_0[1 + 2\Delta E/E_p + 4(\Delta E/E_p)^2 + \ldots]$ [Wannberg, 2009]. Here $\Delta E = E'_{\text{kin}} - E_p$, and E'_{kin} is the photoelectron kinetic energy inside the analyzer.[3]

[3] A distinction is made between E'_{kin} and E_{kin}. The latter, recall, is the photoelectron kinetic energy prior to entering the analyzer. These typically differ, because quite often a retarding/accelerating voltage is applied to the electron in the lens system prior to entering the analyzer. This will be addressed in the next section (2.4.2).

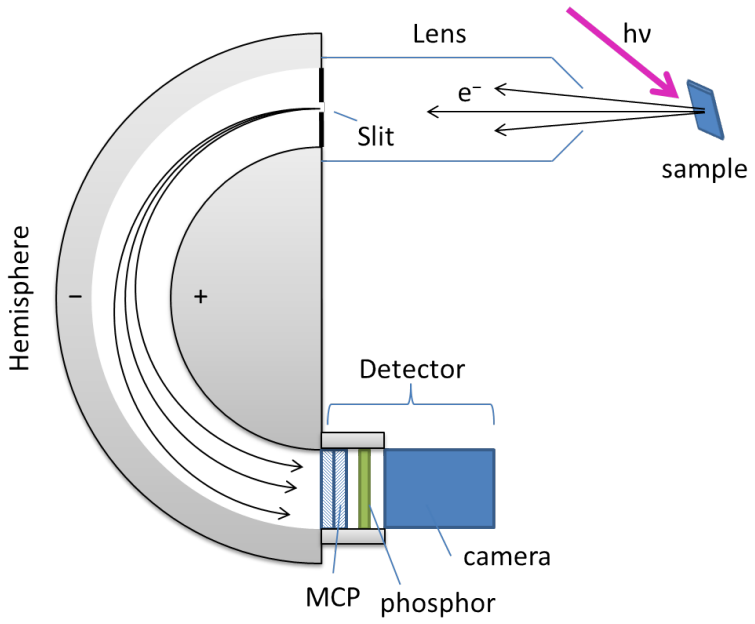

Figure 2.3: Schematic of a hemispherical ARPES analyzer. Details of the electrons' paths through the lens are not shown. See Fig. 2.4 and discussion.

We see from this that electrons with identical kinetic energy, but which enter the analyzer at various positions along the entrance slit, will land at the detector forming an arc of radius r. To decouple the energy and angle axes of the detector, the arc must be transformed to a straight line. This is actually simple to accomplish: Either make the the entrance slit curved with radius r_0, or correct the curvature on the detector with software. Having done this, a photoelectron's arrival position at the detector — measured along the axis perpendicular to the slit — signals its kinetic energy. Meanwhile, the arrival position in terms of the slit axis indicates from where along the slit the photoelectron originated.

Thus the hemispherical analyzer equipped with an entrance slit and a 2D detector can simultaneously map kinetic energy and entrance position. ARPES, however, seeks a method of

Additionally, and at the risk of going into too much detail, there is the subtle and less-often considered fact that the analyzer possesses its own work function Φ_a, which affects E'_{kin} — even with no applied retardation or acceleration voltage. Fortunately, Φ_a is a constant of the system, and there are only rare instances where it needs to be taken into account.

angular resolution, not spatial resolution. It is therefore necessary to map the emission angles of the photoelectrons to positions along the slit, prior to their entrance into the hemisphere. This is accomplished by the use of an electron lens system operating in so-called angular mode.

2.4.2 Electron lens

The electron lens system used in ARPES is comprised of a set of axially symmetric electrostatic elements. It serves two key purposes: (i) Retarding/accelerating the electrons so that a certain range of E_{kin} can be studied at a given E_p, and (ii) mapping the electrons' emission angles to positions along the entrance slit (at a specified magnification). The angle-to-position mapping operational mode is often referred to as "angular mode" to distinguish it from "transmission mode" in which the photoelectrons undergo a position-to-position mapping. The angular mapping is (ideally) irrespective of the particular position on the sample from which each electron is emitted. Fig. 2.4 illustrates electron trajectories through an electron lens in angular mode. The paths are ray tracing simulations by Wannberg [Wannberg, 2009] for electrons emitted from the sample at regular intervals of the emission angle.

In general, the design and operation of the lens is quite complicated [Kevan, 1983, Wannberg, 2009]. The lens element voltages must be adjusted depending on the voltages of the hemispheres, necessitating a software table that specifies the lens settings appropriate to the choice of retarding ratio E_{kin}/E_p. Lens tables are calculated by the analyzer manufacturer using ray-tracing software. In the very low kinetic energy range, some manual refinements to these tables might be necessary. These adjustments can be made with the use of a calibration device inserted into the path of the electrons, casting a shadow of regularly-spaced stripes onto the detector [Koralek, 2006, Koralek et al., 2007].

The VG Scienta analyzers have popularized a "swept" data collection mode where E_p is held constant, and the retarding voltage is smoothly varied so that a wide range of E_{kin} passes over the detector. As this happens, the counts are integrated into E_{kin} bins. This acquisition mode has the advantage of being able to scan over an arbitrary range of E_{kin} while maintaining a constant

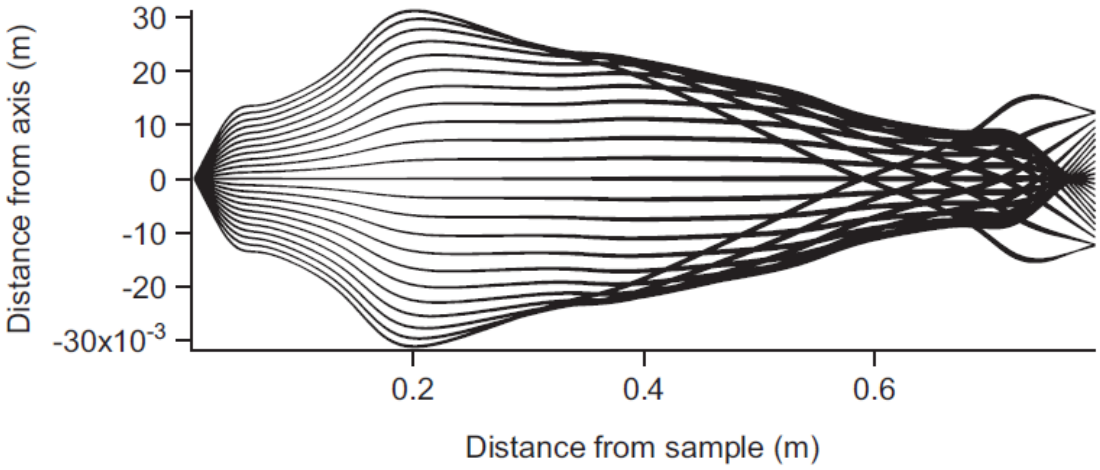

Figure 2.4: Electron trajectories through an electron lens system operating in angular mode. The vertical axis is the position along the slit, measured from the center line. The horizontal position is the distance traveled down the length of the lens, starting from the sample surface. The traces are calculated at regular intervals of the emission angle: $0°, \pm 2°, \pm 4°, \ldots, \pm 22°$. From [Wannberg, 2009]. Reprinted with permission from Elsevier, copyright 2009.

energy resolution (which can be shown to be proportional to E_p). Additionally, the counts at each E_{kin} are integrated over the whole detector, which eliminates any complications due to a possibly inhomogeneous response of the detector along the E axis. The swept acquisition mode only became possible after many advances in lens technology and the implementation of software lens voltage tables. One noteworthy disadvantage of swept mode is that the E_{kin}-vs-angle imaging of the lens at each retarding ratio inevitably features some subtle image "warping" due to abberations and some energy dependence of the lens magnification. By constantly varying the retarding ratio, the warping evolves as the image is swept over E_{kin}, which worsens the angular resolution when the counts are binned. Recently analyzers made by SPECS GmbH are using de-warping algorithms to correct this effect at each value of the retarding ratio, and VG Scienta is moving in this direction

as well [Wannberg, 2009].

2.4.3 Detector

The past several years have witnessed key refinements in hemisphere and electron lens design that have greatly improved the angle and energy resolution of ARPES spectrometers. On the other hand, the final element of the spectrometer — the detector — has at least managed to keep up with the pace of improvements in CCD technology, but otherwise has changed very little. Recently, as our group's research has tested the performance boundaries of state-of-the-art ARPES systems, we have encountered unexpected hindrances due to some detector systems. In many cases the difficulties are inconsequential, but when attempting certain highly detailed analyses, complications can certainly arise. For this reason, an unusual amount of time will be devoted to describing the detector. Hopefully the near future will see improvements to these systems.

A three-element detection system is used to capture the 2D image of photoelectrons arriving at the output of the analyzer. First, the electrons are accelerated by high voltage through a microchannel plate (MCP). The MCP consists of many small pores (μm-scale "microchannels") that pass through the plate at an angle. When an electron strikes the wall of a microchannel, the collision knocks several other electrons free. These electrons, in turn, accelerate through the microchannel, striking the walls, and leading to an exponential cascade of electrons, thus greatly amplifying the signal of just a single electron. In other words, an MCP operates somewhat like a standard photomultiplier tube, but with 2D spatial resolution. In most ARPES detectors, two MCPs are stacked in series with the microchannels at an angle to each other, and the combined gain is often something like 10^6.

Once the electrons leave the MCP stack, they are accelerated again by high voltage toward the second element of the detector, a phosphor-coated screen. The impact of the electrons on the phosphor causes a fluorescent flash that is detected by the final detector element, a CCD camera.

The design of the detector system is one of the most crucial aspects of a high-resolution spectrometer, as the detector is a source of signal noise, resolution, and potential nonlinearity.

Detectors can suffer from readout and thermal noise in the CCD. Additionally, the MCP has a large spread in signal gain (perhaps a factor of 10^2), due to the range of distances an electron may travel down a microchannel before triggering an electron cascade. Meanwhile "blooming" of the fluorescence on the phosphor screen and repulsion between the electrons while traveling in the space between the MCP and the phosphor can broaden the signal and worsen the overall resolution. (Generally the CCD pixel size is smaller than the spot size of a single event on the phosphor screen, and thus the CCD contributes little to the resolution.) Concerning this resolution broadening, it can be mitigated to some degree by careful selection of MCP and screen voltages, and by minimizing the distance between the screen and MCP (which ultimately is limited by the voltage between these elements). As for the noise, the vast majority of it can be removed by the use of a high-quality (possibly cooled) camera combined with a background removal algorithm. Another issue is that MCPs deteriorate over time from being bombarded with electrons, and this can result in an inhomogeneous response across the detector. Fortunately, spectrometer manufactures are lately more attention to this ageing and are attempting to slow it. Also VG Scienta's "swept" acquisition mode (which smoothly scans E_{kin} over the detector) essentially makes detector inhomogeneity a non-issue along the E axis, although the angle axis remains a concern.

Unfortunately, nonlinearity of the signal response is a persistent and potentially sinister problem. Under certain measurement conditions, this is a matter of great concern. While the nonlinearity of ARPES detectors has been known for some time at high count rates due to saturation [Seah and Tosa, 1992, Seah et al., 1999], researchers have more recently come to realize that a positive-inflection response in measured vs. real counts (i.e., an increasing detector gain) can exist at low count rates [Mannella et al., 2004]. The very detailed analysis of some very recent and high-quality data — particularly near E_F where counts diminish rapidly — has prompted a return to this problem. For a full treatment of nonlinearity issues in the context of the most modern ARPES experiments, the reader should refer to forthcoming work to be published by T. J. Reber et al. [Reber et al., 2010a]. Wherever applicable in this thesis, the raw ARPES data has been corrected to account for nonlinearity, or — at the very least — analysis results have been verified

to be robust against a "worst case" assumption for the detector response.

It is worth noting that virtually all complications due to broadening, noise, and nonlinearity can in principle be (nearly) eliminated by switching to a signal processing method that counts individual electrons (pulse-counting mode), rather than the light intensity at the CCD (ADC mode).[4] The key drawback of pulse-counting is that the photoelectron flux at the detector must be reduced such that there is very low probability that two events will fall within the detector's spatial resolution of each other within the time of a single camera exposure. If such a flux rate is exceeded, multiple events can be lumped together by the counting algorithm, thus introducing a (potentially huge) nonlinearity. Given the spatial resolution of the MCP/phosphor system coupled with present frame rates of high-resolution CCD cameras, pulse-counting currently demands a significant sacrifice in terms of photoelectron flux, which is a major impediment to its usage in most experiments. As a result, at the moment it is rarely employed in ARPES, and all the data presented in this thesis was collected in ADC mode.

Presently there is increasing interest in applying advances in high-speed cameras and data processing to the task of high-flux 2D pulse-counting [Vos et al., 2009]. As technology advances to the point where pulse-counting systems can compete with the flux rates of ADC systems, pulse-counting will become widely viable, and this should represent one of next great leaps in the technique of ARPES.

2.4.4 Light source

A variety of light sources have been developed for ARPES: gas discharge lamps, synchrotron beamlines, and, recently, lasers. Each light source possesses a unique combination of advantages and disadvantages in terms of size, cost, and photon energy and polarization tunability. Of these, synchrotron beamlines are clearly the most versatile, and also the largest and most costly. Depending on design, they can in principle achieve fully tunable polarization and also an enormous range of tunable photon energies ($\sim 10^1$–10^4 eV). One key drawback in terms of performance is

[4] The name comes from the common acronym for analog-to-digital conversion.

the presence of higher-order background light from the monochromator. Another problem is the instability of the photon flux due to the time-decay of the particle current in the storage ring. Increasingly, synchrotrons are being built (or upgraded) to operate in "top-off mode" to virtually eliminate this instability.

Lasers, by contrast, have the advantage of highly stable photon energy and output power, fully and easily tunable polarization, and high photon flux in an extremely narrow bandwidth. Moreover, they are obviously far less costly than synchrotrons. Lasers suitable for ARPES have only recently been developed by making use of advances in nonlinear optics. These systems are not broadly tunable in energy, and so far only exist at a small number of discrete, low photon energies – e.g., 6 eV [Koralek et al., 2007] and 7 eV [Kiss et al., 2005].

Gas discharge lamps are the simplest and cheapest light sources. They emit discrete, stable photon energies at various transition lines, and they can reach Doppler-limited resolution. The light is generally unpolarized. One disadvantage of lamps is that the light can contain unwanted background from ancillary transition lines. Furthermore, the photon flux tends to be low relative to other light sources. Nevertheless, gas discharge lamps perform quite well for many ARPES applications, and they have been used to obtain very high energy resolution from angle-integrated PES [Chainani et al., 2000, Yokoya et al., 2000, Yokoya et al., 2001]. Helium lamps using the 21.2-eV He-Iα line have been especially popular for ARPES.

Prompted by the success of laser-based photoemission [Kiss et al., 2005, Koralek et al., 2006], there has recently been a push to develop more light sources in the sub-10-eV range. These photon energies offer several advantages which will be detailed in section 2.7. A small number of ARPES synchrotron beamlines are now configured to operate in this energy range (e.g., SSRL BL5-4 and HiSOR BL-9A). Also, a xenon lamp with emission down to $h\nu = 8.437$ eV has recently been developed [Souma et al., 2007].

2.4.5 Vacuum chamber, surface preparation, and cryostat manipulator

ARPES experiments are typically carried out in an ultrahigh vacuum (UHV) chamber with pressure on the order of 10^{-11} Torr — i.e., about 10^{-13} (one ten-thousandth of one billionth) of atmospheric pressure. The low pressure prevents contamination of the sample surface by gas molecules. This is critical, because the escape depth of the photoelectrons is rather shallow (as will be discussed shortly), and hence the quality and chemical composition of the surface greatly affects the measured spectra. Clean, smooth sample surfaces are typically achieved by some sort of in vacuo surface preparation. For the studies done here on bismuth-based cuprate superconductors, the surfaces are prepared by cleaving off the top layers of the samples after they have been transferred into the UHV environment. Bi-based cuprates in general cleave fairly nicely, and the compound $Bi_2Sr_2CaCu_2O_{8+\delta}$ (Bi2212) is widely considered the best-cleaving cuprate superconductor. This is the key reason why Bi2212 is the focus of this thesis.

It is crucial that the vacuum chamber provide good shielding from stray magnetic fields, as they will deflect the photoelectrons and hurt the accuracy of the measurements. This becomes an especially strong concern for electrons with low kinetic energies. To combat stray fields, the chamber is typically lined with μ-metal shielding. μ-metal is a nickel-based alloy with very high magnetic permeability, making it an ideal magnetic shield. In the laser-ARPES system at Colorado, the chamber actually has two layers of this shielding which tie into μ-metal that lines the electron lens. At the sample position, stray magnetic fields are reduced to only about 1 mG [Koralek et al., 2007].

For study, a sample is affixed to the end of a cryostat manipulator. A typical manipulator nowadays has at least five degrees of freedom: the Cartesian x, y, and z coordinate axes, as well as polar and azimuthal angles θ and ϕ, respectively. This allows the sample to be positioned at the focus of the electron lens and scanned over the $\boldsymbol{k}_{\parallel}$ momentum space.

Cryostat temperature control is typically accomplished by flowing a liquid cryogen (almost always liquid He) to a heat-sink that is thermally coupled to the sample stage. A heater and

temperature-sensing diode connected near the stage allow an arbitrary temperature to be maintained at the sample — usually by a "PID" temperature controller. Well-designed cryostat manipulators used in ARPES can typically achieve sample temperatures near or below 10 K and can maintain sub-K stability.

2.5 Theory of the spectral function

The discussion up to this point has focused on how ARPES measures the energy and momenta of photoelectrons, but there has been no attempt so far to decipher what this information actually means or what to do with it. To get a handle on the understanding and analysis of photoemission data, a three-step model is typically employed. This model is discussed in many sources. A particularly clean and modern treatment of the theory is presented by Damascelli [Damascelli et al., 2003, Damascelli, 2004], and the discussion here follows especially along the lines of these works. The steps are simply: (i) the electron absorbs a photon, exciting it to a bulk final state; (ii) the electron travels to the sample surface; and (iii) it is transmitted through the surface to the vacuum. The aim of the model is to condense all the "real physics" into the excitation process of step (i). Any interactions that might occur post-excitation between the photoelectron and the remaining $(N-1)$ system in (ii) will (ideally) manifest as only a minor and easily-dealt-with background, while the transmission rate at the surface will (ideally) only negligibly modulate over the momentum and energy range of interest. A great simplification of the physics in step (i) is typically made by invoking the "sudden approximation", which treats the excitation step as instantaneous. This allows the N-electron wavefunction to be factorized into a single-electron wavefunction $|\phi_f^{\boldsymbol{k}}\rangle$ and the remaining $(N-1)$-electron state $|\Psi_f^{N-1}\rangle$:

$$|\Psi_\alpha^N\rangle = |\phi_\alpha^{\boldsymbol{k}}\rangle|\Psi_\alpha^{N-1}\rangle = |\phi_\alpha^{\boldsymbol{k}}\rangle\hat{c}_{\boldsymbol{k}}|\Psi_\alpha^N\rangle. \tag{2.8}$$

Here $\alpha = i$ or f signifies the initial or final state. The rightmost side optionally rewrites $|\Psi_f^{N-1}\rangle$ in terms of the particle annihilation operator $\hat{c}_{\boldsymbol{k}}$ acting on $|\Psi_f^N\rangle$. It is understood that the states in the above equation are properly antisymmetrized for fermions.

In the lowest-order t-dependent perturbation theory, the transition rate w_{fi} for $|\Psi_i^N\rangle \rightarrow |\Psi_f^N\rangle$ is

$$w_{fi} \propto |\langle \Psi_f^N | \hat{H}_1 | \Psi_i^N \rangle|^2 \delta(E_f^N - E_i^N - h\nu) \tag{2.9}$$

where $\hat{H}_1 = \frac{e}{2mc}(\boldsymbol{A}\cdot\hat{\boldsymbol{p}} + \hat{\boldsymbol{p}}\cdot\boldsymbol{A} + \frac{e}{c}A^2)$ is the radiation interaction term of the total Hamiltonian. $\boldsymbol{A}$ and $\hat{\boldsymbol{p}}$ are the usual vector potential and momentum operator, respectively. E_i^N and E_f^N are the respective energies of the $|\Psi_i^N\rangle$ and $|\Psi_f^N\rangle$ states. In the dipole approximation, which is frequently invoked, $\hat{H}_1 = \frac{e}{2mc}(\boldsymbol{A}\cdot\hat{\boldsymbol{p}})$. Using Eq. 2.8 and decomposing $|\Psi_f^{N-1}\rangle$ into its eigenstates (labeled by m), the transition rate can be written as

$$w_{fi} \propto |\langle \phi_f^{\boldsymbol{k}} | \hat{H}_1 | \phi_i^{\boldsymbol{k}} \rangle|^2 \sum_m |\langle \Psi_m^{N-1} | \hat{c}_{\boldsymbol{k}} | \Psi_i^N \rangle|^2 \delta(E_{\text{kin}}^{\text{sample}} + E_m^{N-1} - E_i^N - h\nu) \tag{2.10}$$

with total photocurrent proportional to the sum over all w_{fi}'s. The first squared term is familiar: It is the famous Fermi Golden Rule matrix element $M_{fi} = \langle \phi_f^{\boldsymbol{k}} | \hat{H}_1 | \phi_i^{\boldsymbol{k}} \rangle$ for the probability of the single-electron $i \rightarrow f$ transition. The δ-function is also familiar as satisfying the requirement of energy conservation. But what, then, is the remaining summation term?

An understanding of this term is obtained from the Green's function formalism of many-body quantum theory [Fetter and Walecka, 1971, Mahan, 2000]. The Green's function $G(\boldsymbol{k}, t'-t)$ represents the probability of a particle remaining in state $\boldsymbol{k}$ after time $t'-t$. The Fourier-transformed Green's function $G(\boldsymbol{k}, E)$ for the problem of removing an electron from the N-electron system is

$$G(\boldsymbol{k}, E) = \sum_m \frac{\left|\left\langle \Psi_m^{N-1} \left| \hat{c}_{\boldsymbol{k}} \right| \Psi_i^N \right\rangle\right|^2}{E - E_m^{N-1} + E_i^N - i\eta} \tag{2.11}$$

η is a convergence factor to be evaluated as $\eta \rightarrow 0^+$. One of the great advantages of the Green's function formalism is that once $G(\boldsymbol{k}, E)$ has been written down, it is a simple matter to compute the corresponding spectral function (i.e., the probability distribution of states as a function of $\boldsymbol{k}$ and E). It turns out to be just

$$A(\boldsymbol{k}, E) = -\frac{1}{\pi}\text{Im}G(\boldsymbol{k}, E). \tag{2.12}$$

This quantity, $A(\boldsymbol{k}, E)$, is equivalent to the summation term of Eq. (2.10). To see this, one uses the identity that $(x - i\eta)^{-1} = \mathit{P}\int x dx + i\pi\delta(x)$ in the limit $\eta \rightarrow 0^+$, where P signifies principal

value integration.

$A(\boldsymbol{k}, E)$, the single-particle removal spectral function, contains a veritable wealth of information — indeed the complete information of all the interactions of the many-body system. In fact, the Green's function can be formally rewritten as

$$G(\boldsymbol{k}, E) = \frac{1}{E - \epsilon(\boldsymbol{k}) - \Sigma(\boldsymbol{k}, E)}, \tag{2.13}$$

where $\Sigma(\boldsymbol{k}, E) = \Sigma'(\boldsymbol{k}, E) + i\Sigma''(\boldsymbol{k}, E)$ is known as the "self-energy". It is a many-body quantity that contains all of the interactions of the electron with the system as a whole (electron-electron, electron-phonon, etc.). The self-energy is reflected in the spectral function as

$$A(\boldsymbol{k}, E) = \frac{1}{\pi} \frac{\Sigma''(\boldsymbol{k}, E)}{\left[E - \epsilon(\boldsymbol{k}) - \Sigma'(\boldsymbol{k}, E)\right]^2 + \left[\Sigma''(\boldsymbol{k}, E)\right]^2} \tag{2.14}$$

where $\epsilon(\boldsymbol{k})$ is the electron dispersion (the "bare band") of the noninteracting system.

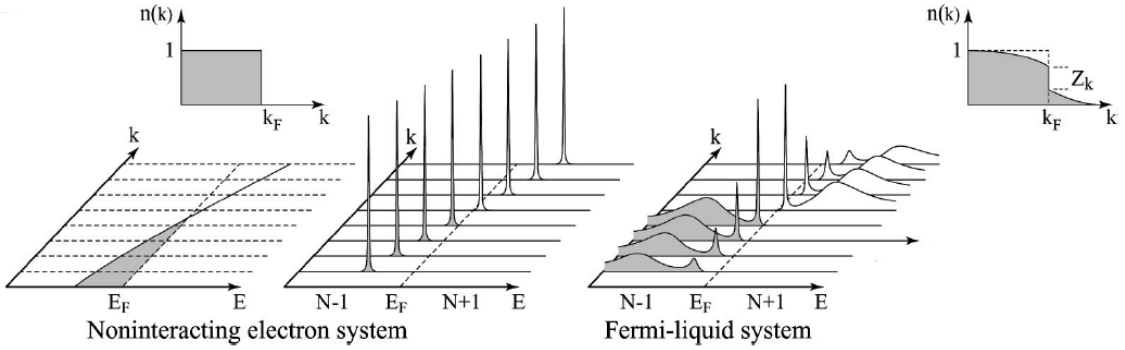

Figure 2.5: The ARPES spectral function in an interacting system. The lefthand figures show the electronic dispersion $\epsilon(\boldsymbol{k})$ and spectral function $A(\boldsymbol{k}, E) = \delta[E - \epsilon(\boldsymbol{k})]$, as well as the distribution function $n(\boldsymbol{k})$, of an idealized noninteracting system. The righthand figures illustrate that the presence of interations (i.e., $\Sigma \neq 0$), as in a Fermi liquid, leads to $A(\boldsymbol{k}, \omega)$ with finite width (i.e., finite lifetime of the excitations) and a possible redistribution of spectral weight away from the "coherent" peak due to energy loss features excited in the photoemission process. Additionally, the dispersion is altered and the spectral peaks shift away from the noninteracting $\epsilon(\boldsymbol{k})$. From [Damascelli et al., 2003]. Reprinted with permission. Copyright 2003 by the American Physical Society.

Recalling that $A(\boldsymbol{k}, E)$ is identified with the summation term of Eq. 2.10, the photoemission intensity measured at a given $(\boldsymbol{k}, E)$ is thus

$$I(\boldsymbol{k}, E) \propto |M_{fi}|^2 \, A(\boldsymbol{k}, E) f(E, T) \tag{2.15}$$

where the final term, $f(E,T) = 1/\exp[(E - E_F)/(k_B T)] + 1$, is the Fermi-Dirac distribution function at temperature T, representing the filling of the Fermi sea.

From Eq. 2.14 it is already evident that $\Sigma'(\boldsymbol{k}, E)$ is manifested as a shift of the peak of $A(\boldsymbol{k}, E)$ away from $\epsilon(\boldsymbol{k})$, while $\Sigma''(\boldsymbol{k}, E)$ broadens $A(\boldsymbol{k}, E)$. Moreover, finite $\Sigma''(\boldsymbol{k}, E)$ broadens $A(\boldsymbol{k}, E)$, which would otherwise be a δ-function, meaning that the excitations have finite lifetimes. The evolution of $A(\boldsymbol{k}, E)$ from a noninteracting to interacting system is sketched in Fig. 2.5. We will investigate in the next section the deeper meaning of $\Sigma'(\boldsymbol{k}, E)$ and $\Sigma''(\boldsymbol{k}, E)$ and how they can be extracted from ARPES data.

We should note here that $I(\boldsymbol{k}, E)$ is the idealized measured spectrum neglecting instrument resolution $R(\boldsymbol{k}, E)$, background $B(\boldsymbol{k}, E)$ from extrinsic (i.e., post-excitation) scattering processes, statistical Poisson noise $P(I)$, and a very small amount of isotropic noise I_{noise} from the detector. The "real-life" spectral function is more like as follows:

$$I_{\text{real-life}}(\boldsymbol{k}, E) = P\left\{\left[|M_{fi}|^2 \, A(\boldsymbol{k}, E) f(E, T)\right] \oplus B(\boldsymbol{k}, E)\right\} \otimes R(\boldsymbol{k}, E) + I_{\text{noise}}. \tag{2.16}$$

Here $\otimes$ denotes convolution while $\oplus$ represents the more complicated process of the redistribution of spectral weight from $I(\boldsymbol{k}, E)$ to $B(\boldsymbol{k}, E)$ due to extrinsic scattering. Section 2.7 will discuss how the use of low photon energies can minimize $B(\boldsymbol{k}, E)$ and $R(\boldsymbol{k}, E)$, leading to measurements which approach the ideal, intrinsic $I(\boldsymbol{k}, E)$. Thus, we will largely be able to overlook background and resolution in this thesis, with one notable exception to be encountered in Ch. 5.

2.6 Interpretation and analysis of ARPES data

2.6.1 Momentum and energy distribution curves

In order to extract meaningful quantities from the measured photoelectron intensity $I(\boldsymbol{k}, E)$, it is common practice to slice up the E-vs.-k spectrum along lines of constant k (called energy

distribution curves, or EDCs) and/or lines of constant E (called momentum distribution curves, or MDCs). The two types of slices are illustrated in Fig. 2.6. While it may prove rewarding to analyze EDCs in the context of testing particular theoretical models [Casey et al., 2008], MDCs have emerged as the preferred analysis tool for modern ARPES.[5] This is a consequence of the fact that if Σ is nearly constant over the momentum width of a band (i.e., $\partial\Sigma/\partial k \approx 0$), then Eq. 2.14 — evaluated at a fixed E — reduces to a Lorentzian in k:

$$A_E(k) = \frac{1}{\pi} \frac{\Sigma''(E)}{\left[E - \epsilon(k) - \Sigma'(E)\right]^2 + \left[\Sigma''(E)\right]^2}. \tag{2.17}$$

(Vector boldface has been dropped in this context, because k is now one-dimensional along the direction of the analyzer's entrance slit.) There is generally no analogous simplification for EDCs; $\Sigma(\boldsymbol{k}, E)$ tends to evolve with E and/or inelastically scattered background complicates the spectrum, leading to a sort of "bastardized" Lorentzian lineshape (multiplied by the Fermi-Dirac distribution). As a result, proper EDC lineshape fitting requires one to assume some particular model for the form of $\Sigma(E)$.

As long as the matrix elements $|M_{fi}|^2$ do not vary too severely, the Lorentzian lineshape of $A_E(k)$ will be be reflected in the measured MDC, $I_E(k)$. Empirically, these conditions on the self-energy and matrix elements are frequently met. In cuprates, no convincing evidence (that the author is aware of) has yet emerged to suggest that the MDC lineshape substantively differs from Lorentzian.

2.6.2 Many-body self-energy

Owing to their simple lineshape, the MDCs are ideal for least-squares fitting. Valuable information about the dispersion and the nature of the many-body $\Sigma(\boldsymbol{k}, E)$ over the full range of energy and momentum space can, in principle, be extracted from MDC analysis.

For a concrete example of how $\Sigma(\boldsymbol{k}, E)$ can be extracted from $I(\boldsymbol{k}, E) \propto A(\boldsymbol{k}, E)$, assume, for the moment, that $\epsilon(\boldsymbol{k})$ can be well-represented by a linear function $\epsilon(\boldsymbol{k}) = v_F^0(k - k_F)$ along some

[5] Valla et al. [Valla et al., 2000] may have been the first to employ Lorentzian MDC fitting in analyzing cuprate spectra, and this especially seemed to have set off interest in the technique.

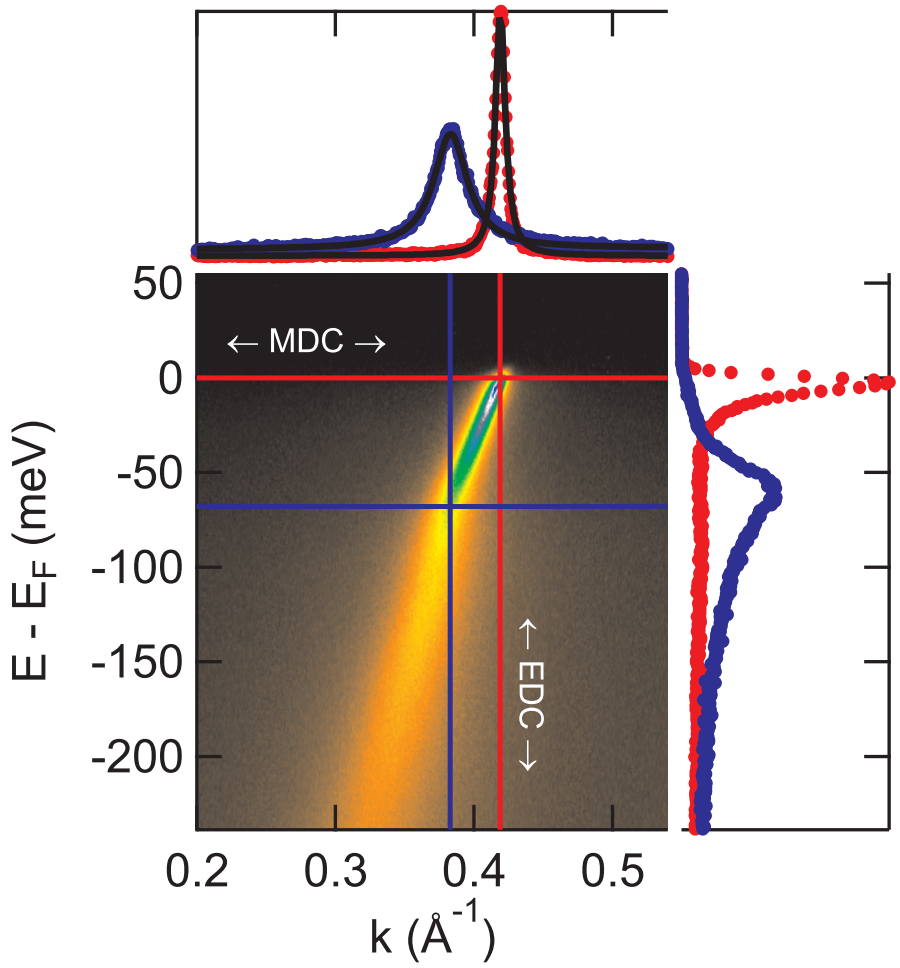

Figure 2.6: Momentum and energy distribution curves (MDCs and EDCs, respectively). The image is ARPES data showing a portion of a band dispersion from Bi2212. The color scale indicates count rate intensity. The locations of two different MDC slices are indicated by horizontal lines, with the corresponding curves plotted on the top set of axes. Likewise, EDC slices are designated by vertical lines, and the corresponding curves are plotted on the righthand set of axes. Lorentzian fits (black) are overlaid on the MDCs, illustrating their simple form. In general, no such simple lineshape exists for the EDCs.

region of E and k studied by ARPES. Based on the Lorentzian form of an MDC slice of $A(k, E)$, the components of the self-energy are

$$\Sigma'(E) = E - v_F^0(k_0 - k_F) \tag{2.18}$$

and

$$\Sigma''(E) = v_F^0 W(E) \tag{2.19}$$

where k_0 is the peak location of the Lorentzian, and $W(E)$ is the HWHM of the MDC. The significance of equations 2.18 and 2.19 in terms of the measured ARPES data is illustrated in Fig. 2.7.

It is now clear from the above equations how $\Sigma(\boldsymbol{k}, E)$ alters the dynamics that would otherwise exist in the noninteracting system. $\Sigma'(\boldsymbol{k}, E)$ shifts ("renormalizes") the dispersion, reflecting a change in effective mass $m^* = \hbar^2(\nabla^2_{\boldsymbol{k}} E)^{-1}$. Meanwhile $\Sigma''(\boldsymbol{k}, E)$ broadens the spectrum, which is related to the inverse lifetime (scattering rate) of the interacting state via $1/\tau = 2\Sigma''(E)/\hbar$. Without self-energy, the spectrum would simply be infinitely sharp and follow along $\epsilon(\boldsymbol{k})$ — in other words, $A(\boldsymbol{k}, E) = \delta[E - \epsilon(\boldsymbol{k})]$.

The noninteracting $\epsilon(\boldsymbol{k})$ is required for an exact determination of the self-energy from the data. Unfortunately, in complex systems such as the cuprates, it is not clear that valid calculations of $\epsilon(\boldsymbol{k})$ can reliably be obtained under all circumstances from first principles. Thus, the bare dispersion is not known to the experimenter a priori. Various techniques attempting to circumvent this difficulty exist [Ingle et al., 2005, Kordyuk et al., 2005, Meevasana et al., 2008, Veenstra et al., 2010].

One such technique is based on Kramers-Kronig analysis of the self-energy. Since the self-energy is a type of response function, it must obey causality. It follows, then, that its real and imaginary parts can be transformed into each other by the Kramers-Kronig relations. These are

$$\begin{aligned} \Sigma'(E) &= \frac{1}{\pi} P \int_{-\infty}^{\infty} \frac{\Sigma''(E)}{E' - E} dE' \\ \Sigma''(E) &= -\frac{1}{\pi} P \int_{-\infty}^{\infty} \frac{\Sigma'(E)}{E' - E} dE' \end{aligned} \tag{2.20}$$

where P again indicates principal value integration. In principle the Kramers-Kronig relations can be used together to determine $\epsilon(\boldsymbol{k})$ experimentally, and this has been attempted in some cases [Kordyuk et al., 2005]. Unfortunately, the relations are based on integration from $-\infty$ to

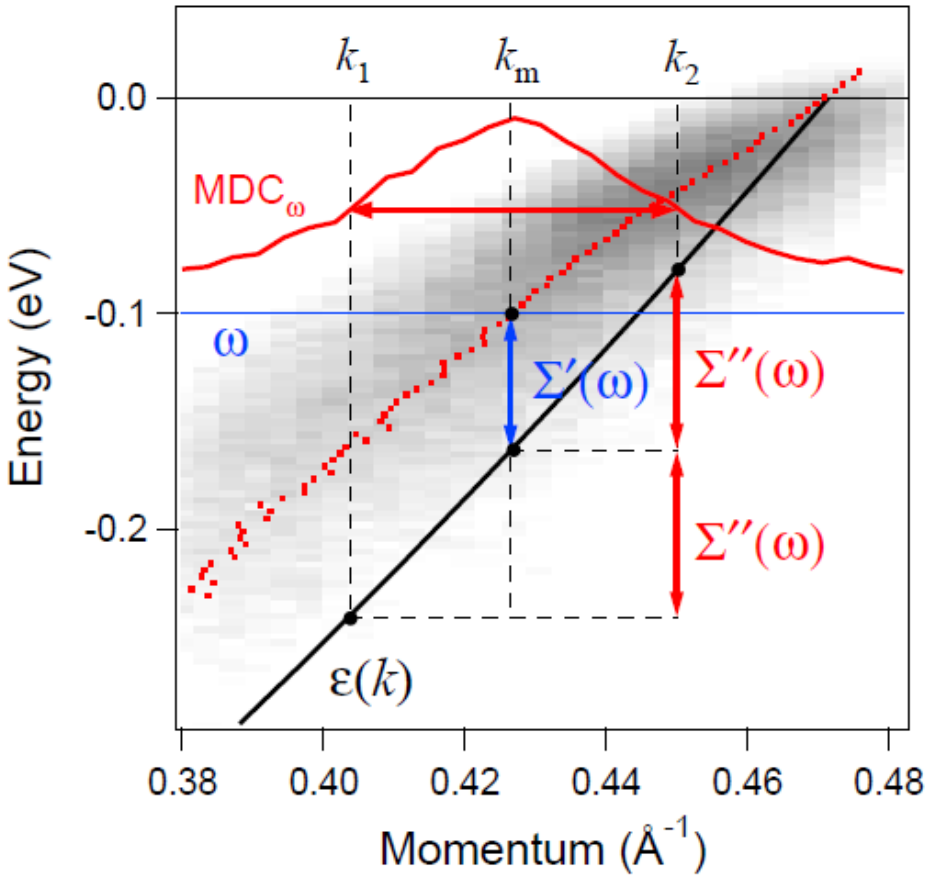

Figure 2.7: Self-energy in ARPES spectra. $\Sigma'(E)$ corresponds to the deflection of the measured MDC dispersion away from the bare dispersion. $\Sigma''(E)$, meanwhile, relates to the width of the spectrum. This figure shows, in particular, a linear bare dispersion with Lorentzian MDC lineshapes, in which case the self-energy is given by equations 2.18 and 2.19. Note the k_m corresponds to the measured location of the MDC peak, and k_1 and k_2 are the momenta at half-maximum. $\omega = E - E_F$. From [Kordyuk and Borisenko, 2005]. Reprinted with the authors' permission.

$+\infty$, while obviously the experimental range of E must be finite. It turns out this would actually not be a problem were $\Sigma''(E)$ to at least flatten out approaching the endpoints of the dataset, but, alas, this is typically not the case. Additionally, useful data cannot be obtained for energies much higher than E_F, due to low thermal occupation of these states. As a result, one typically assumes electron-hole symmetry of $\Sigma(E)$ with respect to E_F, but recently there is some question as to whether cuprates obey this symmetry [Hashimoto et al., 2010].

An alternative approach, used extensively in this thesis, is to simply assume $\epsilon(\boldsymbol{k})$ is smooth (e.g., linear in the region being studied) and to choose it so as to connect two points on the measured dispersion that contain some feature of interest between them. The result is not claimed to be the true self-energy, but rather an effective self-energy Σ_{eff} that captures the most interesting physics of the system. One key advantage of this approach is that it tends to filter out any smoothly varying contribution to $\Sigma(E)$ (e.g., presumably electron-electron interactions and impurity scattering) while highlighting those that are sharper in energy (e.g., as electron-phonon interactions might be expected to be) [Ingle et al., 2005]. For this reason, as well as its simplicity, the effective bare band method has been employed in several recent studies [Johnson et al., 2001, Shi et al., 2004, Zhou et al., 2005, Iwasawa et al., 2008, Zhang et al., 2008b, Plumb et al., 2010, Vishik et al., 2010].

Supposing that a straight line with slope v_F^{eff} is chosen as the effective bare band, then the calculation of $\Sigma'_{\text{eff}}(E)$ follows straightforwardly by replacing v_F^0 with v_F^{eff} in Eq. 2.18. $\Sigma''_{\text{eff}}(E)$ is sometimes found in an analogous manner using Eq. 2.19. While this can provide a useful estimate of $\Sigma''_{\text{eff}}(E)$ in certain circumstances, it is important to note that $\Sigma''_{\text{eff}}(E)$ computed in this manner is not consistent with the definition of $\Sigma'_{\text{eff}}(E)$. This is due to the fact that v_F^{eff} was chosen so as to remove most of the slow-moving contributions from $\Sigma'(E)$ in order to isolate just $\Sigma'_{\text{eff}}(E)$. However, no such subtraction has been applied to the MDC widths, which still contain the contributions of all the interactions that had been removed from the real part of the self-energy. Fortunately, all is not lost. The freedom to choose the effective bare band means that $\Sigma'_{\text{eff}}(E)$ may be constructed to go to zero at deep energy. In this case, the spectrum is well-behaved at its endpoints, and with high-quality data it becomes possible to compute $\Sigma''_{\text{eff}}(E)$ by numerical Kramers-Kronig transformation

of $\Sigma'_{\text{eff}}(E)$ (Eq. 2.20).

2.6.3 Matrix elements

Photoexcitation matrix elements $|M_{fi}|^2$ have so far been left out of most of the discussion, but they can play an important role in ARPES. In theory, strong transitions in the behavior of $|M_{fi}|^2$ as a function of $\boldsymbol{k}$ and E may severely alter the measured spectra, making the interpretation of the data quite difficult. A recent famous example is the observation by ARPES of a large dispersion anomaly at high binding energy in cuprates [Graf et al., 2007, Valla et al., 2007], which is thought to be greatly complicated by matrix element effects [Basak et al., 2009,Moritz et al., 2010] (perhaps in concert with non-negligible background scattering) — possibly to the extent that the supposed dispersion feature is completely artificial [Inosov et al., 2007b, Inosov et al., 2008, Zhang et al., 2008a, Wang et al., 2009]. In this thesis, which focuses on energies closer to E_F, we will not encounter any matrix element effects in cuprates that distort the spectra nearly as dramatically as is seen at deeper binding energy. Still, the experimenter must keep the possibility of such effects in mind, and to that end, it is certainly worth having at least a very elementary understanding of matrix element behavior.

While the matrix elements depend on the details of the radiation field $\boldsymbol{A}$ and the overlap of the single-electron initial and final states, there is nevertheless at least one universal behavior of the matrix elements that arises from symmetry and bears mentioning: If the final state $\langle\phi_f^{\boldsymbol{k}}|$ has odd symmetry about the mirror plane of the analyzer (perpendicular to the slit), it cannot be detected, since it will be zero everywhere in the plane where the detector lies. Hence any final state that is actually detected is necessarily even with respect to the mirror plane. A consequence of this is that the photocurrent at the detector will be zero if the righthand side of the dipole matrix element, $\boldsymbol{A}\cdot\boldsymbol{p}|\phi_i^{\boldsymbol{k}}\rangle$, is odd. Since $\boldsymbol{A}\cdot\boldsymbol{p}\propto\hat{\boldsymbol{\varepsilon}}\cdot\boldsymbol{r}$, where $\hat{\boldsymbol{\varepsilon}}$ is the polarization vector, the dipole operator has even or odd parity if $\hat{\boldsymbol{\varepsilon}}$ lies in the plane (p-polarized) or out of the plane (s-polarized), respectively. This leads to matrix elements which are zero for odd $|\phi_i^{\boldsymbol{k}}\rangle$ studied with s-polarized light, and for even $|\phi_i^{\boldsymbol{k}}\rangle$ studied with p-polarized light. These conditions under which $M_{fi}=0$ can be expressed

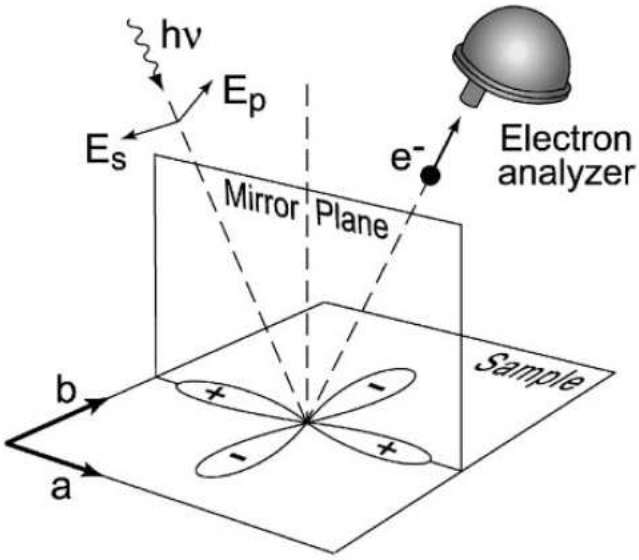

Figure 2.8: Symmetry considerations of the matrix elements. In this example, a sample is oriented so that the $d_{x^2-y^2}$ orbital along its surface is even with respect to the mirror plane. In this configuration, photoemission from s-polarized light is disallowed by symmetry (see Eq. (2.21)). From [Damascelli et al., 2003]. Reprinted with permission. Copyright 2003 by the American Physical Society.

as

$$\langle \phi_f^{\boldsymbol{k}} | \hat{\boldsymbol{\varepsilon}} | \phi_i^{\boldsymbol{k}} \rangle = 0 \text{ for } \begin{cases} \langle + | + | - \rangle \\ \langle + | - | + \rangle \end{cases} \tag{2.21}$$

where "+" and "−" stand for even and odd symmetry about the mirror plane, respectively. The geometry of this problem is illustrated in Fig. 2.8. The example of a $d_{x^2-y^2}$ orbital parallel to the sample surface is shown, with the sample oriented such that the orbital is even with respect to the mirror plane. Under these circumstances, Eq. (2.21) shows that if the incoming light is s-polarized, then $M_{fi} = 0$.

2.7 ARPES in the low photon energy regime

Aside from some early PES work [Feuerbacher and Fitton, 1972], researchers in photoemission largely abandoned the low photon energy range below 10 eV in favor of higher energies — typically 20–100 eV or so. This was probably driven in large part by the substantial difficulty of studying slow-moving photoelectrons (which can very easily be deflected by stray magnetic fields) and concerns about the validity of the sudden approximation at low energies, as well as by other practical considerations such as the design of beamline monochromators. However, over the past decade or so, lasers with low photon energies began to be adopted for high-resolution time-resolved [Wolf, 1997] and direct photoemission [Kiss et al., 2005, Shimojima et al., 2005], but, like previous low-$h\nu$ work, the experiments were not angle-resolved, which perhaps reflected lingering concerns about the extreme difficulty of measuring the emission angles of such slow-moving photoelectrons. Whatever the reasons, these experiments were still lacking one of the key benefits of ARPES with low-energy photons: ultrahigh momentum resolution.

Currently there has been growing enthusiasm for low photon energy ARPES (LE-ARPES). Much of the excitement was sparked by Koralek et al.'s work using laser-based ARPES at 6-eV photon energy, which studied $Bi_2Sr_2CaCu_2O_{8+\delta}$ (Bi2212) and found that even at such low energy, the sudden approximation did not suffer any catastrophic breakdown [Koralek et al., 2006]. Moreover, the data obtained in those experiments, shown in Fig. 2.9, was absolutely unparalleled, and it revealed that the spectral peaks in cuprates are intrinsically much sharper than many had previously thought — sharp enough, in fact, to open the possibility they can be described in terms of Fermi-liquid-type quasiparticles.[6] As we will see, LE-ARPES has certain advantages over conventional ARPES, and there is good reason to believe the spectra from cuprates studied by LE-ARPES represent something approaching the unadulterated, intrinsic properties of these systems.

[6] The term quasiparticle is somewhat open to interpretation, and its meaning is often a matter of context. However, in Landau's Fermi liquid theory — a generic model of electron-electron interactions in an uncorrelated system — the interaction-dressed electron states near E_F must satisfy $|\Sigma''(E)| \leq |E - E_F|$. The result from Koralek finds that this condition is satisfied in Bi2212.

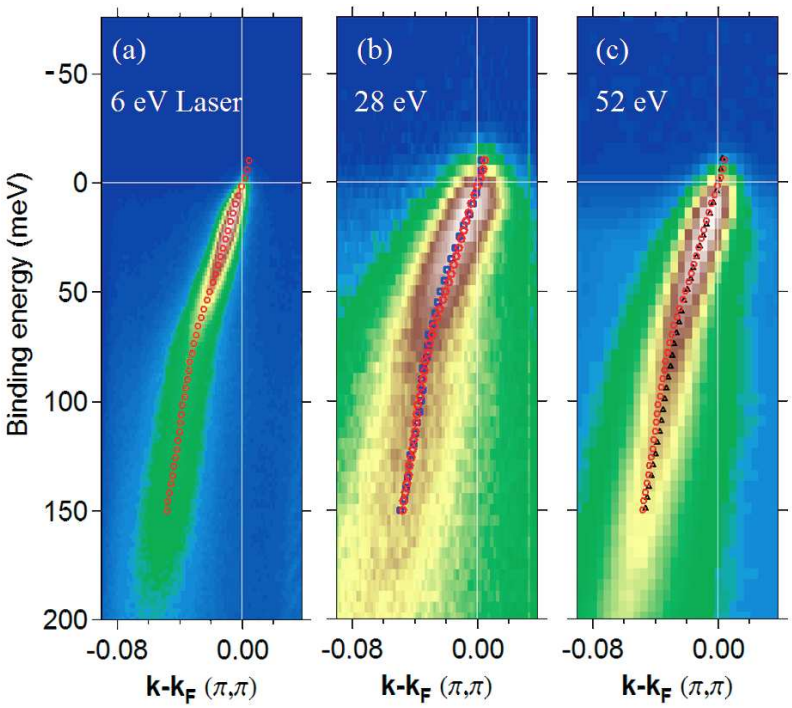

Figure 2.9: Comparison of ARPES from Bi2212 at (a) $h\nu = 6$ eV, (b) 28 eV, and (c) 52 eV. The data are taken along the $(0,0) - (\pi,\pi)$ direction of the Brillouin zone. The 6-eV photons were produced from a laser source [Koralek et al., 2007], while synchrotron radiation was used for the 28- and 52-eV spectra. The dispersions obtained from Lorentzian MDC fits (section 2.6) to the 6-eV data (red circles) agree well with the same dispersions extracted from the 28- and 52-eV data (blue squares and black triangles, respectively). Hence, there is little evidence of any catastrophic breakdown of the sudden approximation for photon energies down to at least 6 eV. While the sudden approximation thus appears to remain valid, the spectrum at 6 eV is dramatically sharper than for the other photon energies. This is due to a combination of advantages in the low photon energy regime: improved momentum resolution, increased bulk sensitivity, and reduced background scattering. From [Koralek et al., 2006]. Reprinted with permission. Copyright 2006 by the American Physical Society.

2.7.1 Momentum and energy resolution

From Eq. 2.3, it is clear that the momentum resolution $dk_{\|}/d\alpha$ at fixed α behaves like $\sqrt{E_{\rm kin}}$. Thus momentum resolution improves ($dk_{\|}$ gets smaller) as $h\nu$ is lowered. This corresponds to the slower photoelectrons being refracted more as they cross the sample surface, thereby spreading a smaller amount of k-space over a larger solid angle of the detector. The improvement in resolution can be dramatic: For the case of ARPES with 6-eV photons versus 52-eV photons, the momentum

resolution is better by about a factor of seven. This improvement can account for much of the increase in spectral sharpness seen in the 6-eV data in Figs. 2.9 and 2.10.

In addition to the parallel momentum resolution advantage of LE-ARPES, there is also an advantage in perpendicular momentum resolution. This arises from the increased photoelectron escape depth of the low kinetic energy electrons, which will be discussed in the the next section. Based on the position-momentum uncertainty relation, the deeper escape depth implies that LE-ARPES samples a smaller range of perpendicular momenta $\Delta \boldsymbol{k}_{\perp}$, and it is believed that even in the quasi-2D cuprates, this effect may lead to a noticeable improvement in the spectral sharpness [Smith et al., 1993, Sahrakorpi et al., 2005].

An additional advantage of LE-ARPES is that better energy resolution is a typical side-benefit of lowering the photon energy. For instance, the use of photon energies from about 6 to 7 eV opens up the possibility of using lasers as light sources, and lasers, of course, can have extremely narrow bandwidths. A 7-eV KBBF-based laser, for example, has demonstrated sub-meV resolution in ARPES [Kiss et al., 2005]. Meanwhile, in the case of monochromated light sources such as synchrotron beamlines, low photon energy photon energy goes hand-in-hand with improved energy resolution, since for a grating monochromator $d\nu \propto \nu$. Recently it has been possible to achieve total energy resolution of the combined analyzer and light source (while retaining reasonable photon flux) down to about 3–4 meV at the best low-energy synchrotron beamlines (SSRL BL5-4, HiSOR BL-9A), which is a notable improvement over the resolutions typical of experiments in the conventional photon energy range (usually 10 meV, if not much larger).

2.7.2 Improved bulk material sensitivity

ARPES at conventional synchrotron photon energies of roughly 20–100 eV is predominantly a surface probe. This is due to the fact that electrons in this kinetic energy range have very short inelastic mean free paths λ_0 in the sample. In a broad range of materials, in fact, λ_0 is at a minimum for kinetic energies expected for $h\nu \approx$ 20–100 eV. This is illustrated in Fig. 2.11, which shows data from the "universal curve" of electron inelastic mean free paths from Seah and Dench [Seah and

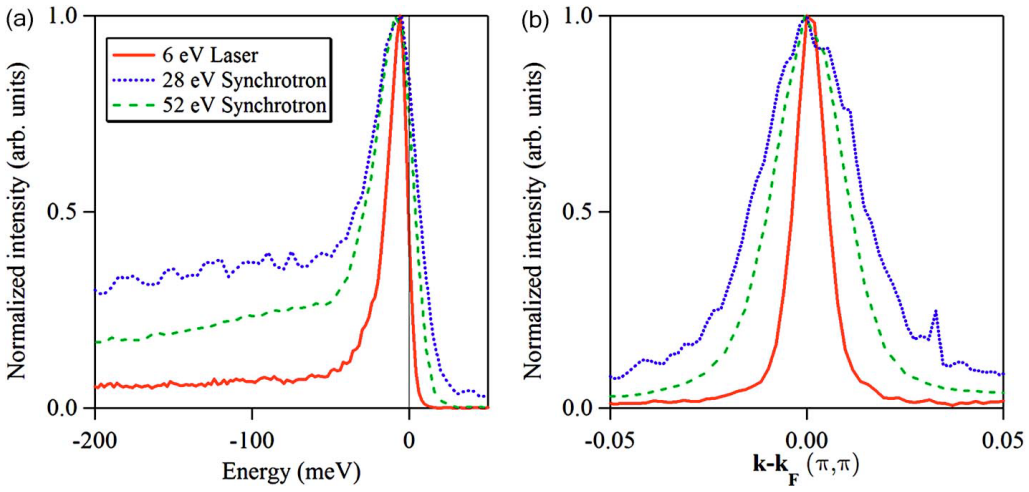

Figure 2.10: Comparison of (a) EDCs and (b) MDCs from Bi2212 at $h\nu = 6$ eV, 28 eV, and 52 eV. The curves come from the 2D ARPES spectra in Fig. 2.9. The EDCs are taken at k_F, and the MDCs are at E_F. From [Koralek et al., 2007]. Reprinted with permission. Copyright 2007, American Institute of Physics.

Dench, 1979]. The data were compiled from experiments on many different materials (elements, as well as organic and inorganic compounds) over an electron kinetic energy range of 0–10,000 eV, using a variety of experimental methods variously based on x-ray photoemission spectroscopy (XPS), low-energy electron diffraction (LEED), and Auger electron spectroscopy (AES) [Powell, 1974].

From Fig. 2.11, it is clear that in typical materials, λ_0 is expected to be roughly one order of magnitude larger than in the conventional photon energy range. Whether electron mean free paths in cuprates follow the universal curve behavior is not strictly known. However, the sharp spectra obtained in the low-$h\nu$ regime (Figs. 2.9 and 2.10) are consistent with the notion that λ_0 follows a universal-curve-like behavior in cuprates, which allows LE-ARPES to probe bulk states with greater sensitivity compared to conventional ARPES.

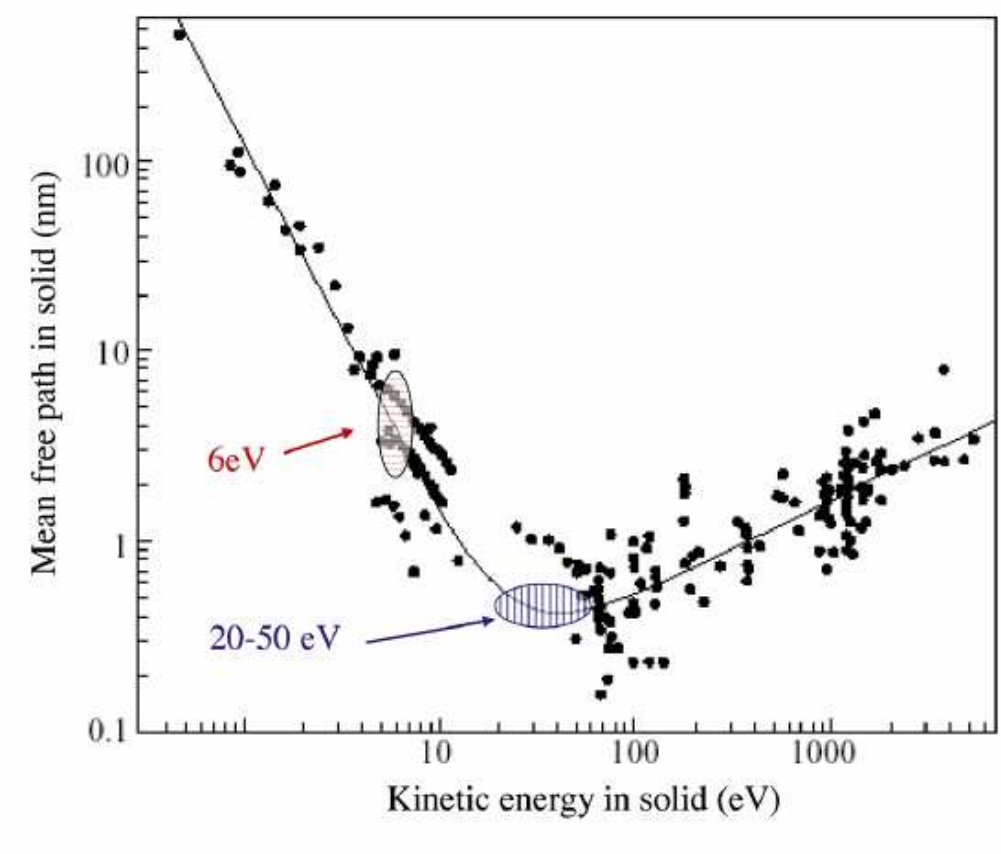

Figure 2.11: "Universal curve" of mean free paths of electrons in solids. For photoemission in the low photon energy regime ($h\nu$ = 6–7 eV), electrons are expected to have nearly one order of magnitude greater inelastic mean free paths than for conventional photoemission in the range of $h\nu$ = 20–100 eV. (20–50 eV is highlighted in here, because this range in particular has been employed frequently in ARPES studies of cuprates.) Thus LE-ARPES should be somewhat more sensitive to the bulk electronic states than conventional ARPES, which is primarily a surface probe. From the Ph.D. thesis of J. D. Koralek [Koralek, 2006], based on data from Seah and Dench [Seah and Dench, 1979]. Reprinted with the author's permission.

2.7.3 The sudden approximation and the validity of LE-ARPES

The drastically increased sharpness of LE-ARPES spectra from cuprates compared to conventional ARPES seems almost too good to be true and merits some discussion as to the validity of the spectra in the low photon energy regime. The gravest concern for LE-ARPES is whether or not

the sudden approximation (section 2.5) remains valid down to very low kinetic energies. The data shown in Fig. 2.9 strongly supports the conclusion that a breakdown of the sudden approximation is not a major concern in cuprates. The measured band dispersion at $h\nu = 6$ eV is almost unchanged from measurements at 28 and 52 eV. Moreoever, the overall trend in the progression of the MDC widths as a function of energy is qualitatively reproduced. The only noteworthy difference is simply that the 6-eV data is much sharper than its higher-energy counterparts. Additionally, this result is consistent with — and indeed expected from — the known behavior of the universal curve of electron inelastic mean free paths (Fig. 2.11). This curve suggests that although a slow-moving photoelectron spends longer in the sample bulk prior to escape, below a kinetic energy of about 10 eV, it is nevertheless less likely to experience a scattering event. Ostensibly, this is telling us that on kinematic and quantum mechanical grounds, the likelihood that a photoelectron will excite some loss mode such as a phonon or plasmon is diminished at very low E_{kin}.

One final consideration is whether the spectra from LE-ARPES might somehow be artificially sharp. There are at least three reasons that artificial sharpening might occur. Based on our studies using LE-ARPES, these possible complications can all be ruled out.

- *Detector nonlinearity.* Artificially sharp spectra could arise from nonlinearity in the detector response. Our own detailed investigations into detector nonlinearity have repeatedly found that while the response of the detector can be a concern for certain types of quantitative analysis, any such effect is not actually significant enough to account for the acute sharpness of LE-ARPES data from cuprates [Reber et al., 2010a].

- *Kinematic compression.* There is an effect known as "kinematic compression" that arises from the kinematic constraints in ARPES combined with the details of the band structure [Smith et al., 1993]. Under some unusual circumstances, the effect can actually lead to the counterintuitive observation of linewidths that are sharper than the inverse lifetimes of the states [Hansen et al., 1998]. This effect can be ruled out as a cause of the sharp cuprate spectra from LE-ARPES. A compression factor C relates the observed linewidth to the

intrinsic one ($\Gamma_{\rm obs} = C\Gamma_i$). In a 2D system such as the cuprates, the expression for the compression factor reduces to $C = 1/|1 - mv_{i\|} \sin^2\alpha/(\hbar k_\|)|$, where $v_{i\|} = \hbar^{-1}\partial E_i/\partial k_\|$ is the group velocity parallel to the surface. Based on experimental values from nodal Bi2212, $C \approx 1.4$ at E_F (the sharpest point on the dispersion) for $h\nu = 6$ eV. Thus kinematic compression can be excluded as a cause of the sharp spectra seen in this material via LE-ARPES.

- *Sudden approximation violation.* Finally, it has been argued that a breakdown of the sudden approximation could conceivably redistribute the spectral weight of a peak in a manner such that the some of the counts at deeper energy shift farther up the peak, closer to E_F [Sawatzky, 2005]. This type of process could sharpen the peaks, but it would do so asymmetrically, thus shifting the peak of the band dispersion. As can be seen in Fig. 2.9, this does not appear to be happening to any significant degree. Band dispersions measured at 6, 28, and 52 eV all quite similar.

There is so far no strong evidence to suggest that ARPES data from cuprates obtained by photon energies as low as 6 eV are in any way invalid or grossly misrepresentative of the physics of the electrons — neither on the grounds of a breakdown of the sudden approximation, nor based on some mechanism of artificial spectral sharpening. To the contrary, the data support the notion that the low photon energy regime has led to spectra that approach the intrinsic lineshapes in these materials. We must conclude, then, that LE-ARPES is a remarkable probe for studying cuprates and other complex materials, providing a pathway to new insights and new discoveries.

Chapter 3

High-Temperature Superconductivity in Layered Cuprates

3.1 Introduction

Superconductivity — the total lack of resistance to the flow of electricity — is nearly ubiquitous in simple metals, but it requires very cold temperatures. It is unsurprising then that it was the first person to liquify helium (with a boiling point of about 4 K), Heike Kamerlingh Onnes, who also became the first to witness superconductivity (in mercury, which superconducts below a critical temperature, T_c, of 4.15 K) [van Delft and Kes, 2010]. Amazing as it must have been for Kamerlingh Onnes to see liquid helium in 1908, it is still harder to fathom what must have been his utter astonishment in 1911 upon finding that the resistivity of mercury was zero below T_c.

And for all intents and purposes, the resistivity is, in fact, zero. So zero that in 1932 Kamerlingh Onnes's assistant flew from Leiden to London transporting a dewar containing a lead ring submersed in liquid helium and carrying a persistent current of 200 A.[1] [van Delft and Kes, 2010] So zero that the modern experimental lower bound on the lifetime of a current in a superconductor is 10^5 years, and theoretical predictions expect 10^{100} years [$\approx$(age of the universe)^{10}, otherwise known as "forever"] [Tinkham, 1996].

Superconductivity presented an immense challenge to theoretical physics that stood for nearly 50 years. The same physical models that could explain so much about the basic properties of simple materials (e.g., why some are metals, others semiconductors, and others insulators) were completely insufficient to explain why electricity should ever flow without resistance. The difficulty,

[1] Clearly these were the days before airport security screening.

in essence, arose from the fact that the electrons in a superconductor no longer act independently of each other, and they can no longer be regarded as merely single particles awash in a bath of averaged interactions. This was finally explained in 1957 by Bardeen, Cooper, and Schrieffer (BCS) whose enormously successful, Nobel-winning theory posited that superconductivity is the result of interacting pairs of electrons that form bound states (now called Cooper pairs) [Bardeen et al., 1957]. Beyond accounting for zero resistivity, many other unique phenomenological aspects of superconductors — e.g., the expulsion of magnetic fields from the superconductor (diamagnetism) known as the Meissner effect,[2] the breakdown of superconductivity above a critical magnetic field H_c, the existence and temperature dependence of a gap in the single-particle excitation spectrum, and even why T_c itself is typically so low — can ultimately be explained by the BCS theory or extensions thereof.

Given the success of the BCS theory, it came as a shock when in 1986 Bednorz and Müller discovered that a rather bizarre compound (composed of La, Ba, Cu, and O) went superconducting at a surprisingly high temperature around 30 K [Bednorz and Müller, 1986]. Within about a year, other new, related copper oxides (collectively called cuprates) achieved T_c's around 100 K [Müller and Bednorz, 1987, Bednorz and Müller, 1988] (see Fig. 3.1). At first glance, these unusual new materials would not appear to be good candidates for metals, let alone superconductors. Black, brittle ceramics made of sandwiched CuO_2 planes, they are actually insulators until electrons are chemically added or removed. BCS was at a loss to explain such high transition temperatures in the cuprates, and thus arguably the most active subfield of contemporary physics was born. Despite intense investigation over the last 25 years, including the discovery of a second family of high-T_c superconductors based on iron [Kamihara et al., 2006, Kamihara et al., 2008], today there is still no accepted theory of high-temperature superconductivity.

[2] In "type I" superconductors, the diamagnetism is perfect, but in "type II", fields penetrate into the sample. Both behaviors are now well-understood, with the latter due the formation discrete localized flux vortices [Tinkham, 1996]. Cuprate high temperature superconductors are "type II".

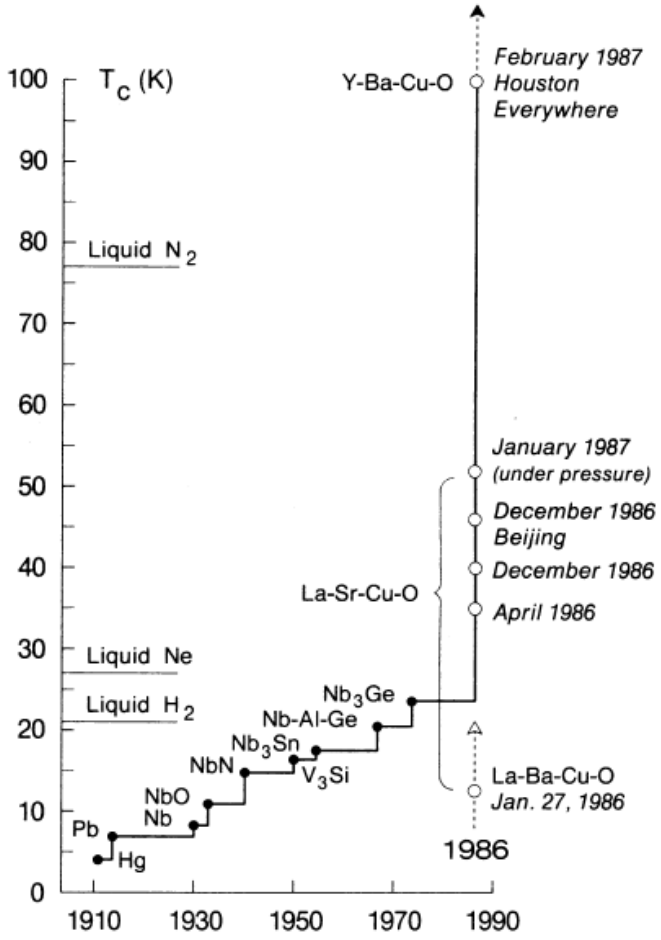

Figure 3.1: Timeline of the progression of T_c. From [Müller and Bednorz, 1987].

3.2 Conventional superconductivity: The BCS theory

The BCS theory is discussed in countless references, so only a skeleton of the theory will be outlined here. It begins by considering interactions between pairs of electrons. This is modeled by a reduced Hamiltonian of the form

$$H = \sum_{\boldsymbol{k},\sigma} \epsilon_{\boldsymbol{k}} n_{\boldsymbol{k},\sigma} + \sum_{\boldsymbol{k},\boldsymbol{k}'} V_{\boldsymbol{k},\boldsymbol{k}'} b^\dagger_{\boldsymbol{k}'} b_{\boldsymbol{k}}. \tag{3.1}$$

The first term just describes the filling of the band $\epsilon_{\boldsymbol{k}}$ where $n_{\boldsymbol{k},\sigma} = c^\dagger_{\boldsymbol{k},\sigma} c_{\boldsymbol{k},\sigma}$ is the number operator composed of conventional fermion creation (annihilation) operators $c^\dagger_{\boldsymbol{k},\sigma}$ ($c_{\boldsymbol{k},\sigma}$) for an electron with

momentum $\boldsymbol{k}$ and spin σ. The operator $b^\dagger_{\boldsymbol{k}} = c^\dagger_{\boldsymbol{k},\uparrow} c^\dagger_{-\boldsymbol{k},\downarrow}$ creates a spin-singlet electron pair scattered into opposite momentum states. Naturally, the complex conjugate $b_{\boldsymbol{k}}$ destroys such a pair. $V_{\boldsymbol{k},\boldsymbol{k'}}$ is the potential through which these pairs interact.

Following some careful reasoning, BCS searched for a variational ground state wavefunction for Eq. 3.1 of the form

$$|\Psi_0\rangle = \prod_{\boldsymbol{k}} u_{\boldsymbol{k}} + v_{\boldsymbol{k}} b^\dagger_k |0\rangle \tag{3.2}$$

where $|0\rangle$ is the vacuum state and $u_{\boldsymbol{k}}$ and $v_{\boldsymbol{k}}$ are "coherence factors" satisfying $|u_{\boldsymbol{k}}|^2 + |v_{\boldsymbol{k}}|^2 = 1$. From this a set of equations are then found that describe the values of the coherence factors that minimize the energy of this wavefunction. It turns out that the solution involves a function

$$E_{\boldsymbol{k}} = \sqrt{(\epsilon_{\boldsymbol{k}} - E_F)^2 + \Delta^2_{\boldsymbol{k}}} \tag{3.3}$$

where $\Delta_{\boldsymbol{k}}$ satisfies

$$\Delta_{\boldsymbol{k}} = \sum_{\boldsymbol{k'}} V_{\boldsymbol{k},\boldsymbol{k'}} \frac{\Delta_{\boldsymbol{k'}}}{2E_{\boldsymbol{k'}}}. \tag{3.4}$$

BCS superconductivity merely requires that $V_{\boldsymbol{k},\boldsymbol{k'}} < 0$. Considering, for instance, $V_{\boldsymbol{k},\boldsymbol{k'}} = -V$ in some window of $E_{\boldsymbol{k}}$ centered about E_F (set, say, by the Debye energy) and $V = 0$ otherwise, then the BCS theory finds that the ground state energy of the system with interacting pairs is lower than that of the normal state Fermi sea. The pairs are evidently bound.

The normal state dispersion $\epsilon_{\boldsymbol{k}}$ is then replaced by the gapped dispersion relation $E_{\boldsymbol{k}} = \pm\sqrt{(\epsilon_{\boldsymbol{k}} - E_F)^2 + \Delta^2_{\boldsymbol{k}}}$ (Eq. 3.3) with separation 2Δ between branches. The appearance of this gap in the spectrum $A(\boldsymbol{k}, E)$ is illustrated in Fig. 3.2. The gapping is the result of Cooper pair formation, with $\Delta_{\boldsymbol{k}}$ corresponding to the minimum energy required to break a pair. It is this binding energy which shields the paired electrons from (non-pair) scattering and which effectively sets the energy scale for T_c. This is the essence of superconductivity.

It is very reasonable to ask why $V_{\boldsymbol{k},\boldsymbol{k'}}$ should ever be attractive, given that the electrons will mutually repel each other. In the conventional BCS superconductors, the answer comes from considering the vibrations of the ion lattice (phonons): An electron can scatter off an ion, exciting a phonon in the lattice. Somewhere else in the material, another electron can be weakly attracted

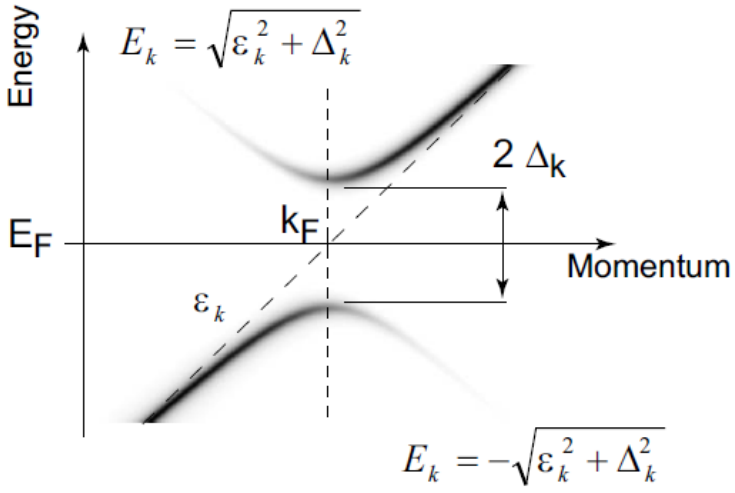

Figure 3.2: BCS superconducting gap in the single-particle excitation spectrum. From [Balatsky et al., 2009]. Reprinted with permission. Copyright 2009 by the American Physical Society.

by the charge modulation due to the phonon. Energetically, then, the first electron is emitting a phonon, and the second electron is absorbing it in a scattering process that conserves energy and momentum. The electrons are thus bound in a sort of spatially-delocalized dance of phonon exchange.

The phonon-mediated pairing has been rigorously experimentally verified for conventional superconductors, but there is nothing to exclude the possibility that other types of interactions could in principle lead to superconductivity. In fact, in systems where the superconducting gap is anisotropic (as in cuprates, see section 3.3.4) the pairing interactions are not even necessarily required to be attractive [Bulut and Scalapino, 1996, Tsuei and Kirtley, 2008]. Hence there is much ongoing debate over what type(s) of interactions act as the pairing "glue" in high-T_c superconductors. ARPES gives us the ability to probe the signatures of these interactions as they are manifested in the electronic dispersion. We will return to this in section 3.3.5, and chapters 4 and 5 will be devoted to the detailed analysis of two interaction energy scales seen in ARPES.

3.3 The cuprate high-T_c superconductors

3.3.1 Structure

The high-T_c cuprates encompass a broad range of materials with a key unifying feature: planes of CuO_2. These planes dominate the electronic properties of cuprates, which exhibit strong quasi-two-dimensionality as a result. This 2D nature is evidenced not only by the Fermi surfaces measured by ARPES, but also by the anisotropy of transport measurements. Resistance is substantially larger in the c-axis than in the a-b plane of CuO_2 layers. This anisotropy can be as large as four orders of magnitude [Iye, 1992].

The bismuth-based family of cuprates have composition $Bi_2Sr_2Ca_{n-1}Cu_nO_{2n+4}$ with $n = 1, 2, 3$ being the number of CuO_2 planes per unit cell. These structures are shown in Fig. 3.3. The single-, bi-, and tri-layer systems are called Bi2201, Bi2212, and Bi2223, respectively. Holes are doped into the samples by non-stoichiometric addition of oxygen, usually denoted by δ (e.g., $Bi_2Sr_2CaCu_2O_{8+\delta}$). Bi2201 and Bi2212 are widely studied in ARPES, because high-quality single crystals can be readily produced, and because the samples cleave exceptionally well (between the Bi-O planes). Bi2212, in particular, is generally considered to be the best-cleaving cuprate. As such, it is probably the single most-studied material within ARPES, and it has yielded the sharpest spectra of any cuprate to date. Since the aim of this thesis is to explore the fine details of the electronic structure of cuprates using ultrahigh-resolution LE-ARPES, it makes sense to study the most spectroscopically clean material, Bi2212. This spectral cleanliness comes at the cost of some complexity in the Fermi surface, as we will see in section 3.3.3. Fortunately, the experiments here will largely dodge and/or mitigate these complications.

A more challenging issue is that Bi2212, while easily obtained in single crystal sizes large enough for ARPES, does not tend to yield crystals large enough for study by inelastic neutron scattering (INS), which can give direct information about the dispersions of phonons and spin fluctuations. INS instead prefers more robust samples — precisely those that cleave terribly and are thus ill-suited for ARPES. The lack of material overlap between these two experiments will

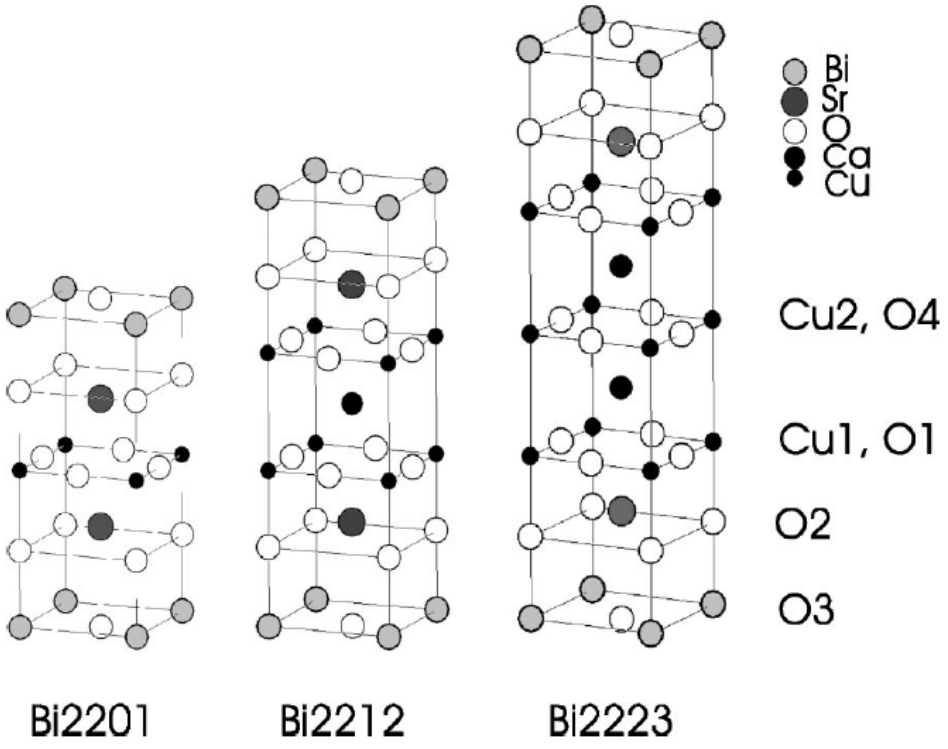

Figure 3.3: Primitive unit cells of the Bi-based family of cuprates. The tetragonal lattice structures have $a = b = 3.814$ Å and c-axis lengths 24.6, 30.6, and 37.1 Å for the single-, bi-, and tri-layer systems, respectively. From [Kovaleva et al., 2004]. Reprinted with permission. Copyright 2004 by the American Physical Society.

show up in Ch. 4, where some attempts at direct comparisons between ARPES and INS data will be made. Still, even relatively dissimilar cuprates generally are not so different from each other in terms of many key properties (e.g., their in-plane phonon dispersions), and the comparisons are presumably valid on a qualitative level.

3.3.2 Phase diagram

The undoped parent compounds of the superconducting cuprates are antiferromagnetic insulators. In particular, they are so-called Mott insulators, which means that they are expected to be (half-filled) metals based on a simple single-electron band structure calculation. However, due

to electron-electron correlations (i.e., on-site Coulomb repulsion of the electrons), these materials are instead insulators.

By doping holes into the cuprates, they leave the antiferromagnetic insulator phase and transition through a number of other phases which are shown schematically in Fig. 3.4. The line T^* is the onset of what is called the pseudogap. This is a poorly-understood state of matter characterized by diminished spectral weight at E_F, somewhat similar to a superconducting gap, yet lacking superconductivity [Loeser et al., 1996, Ding et al., 1996b, Loeser et al., 1997, Fedorov et al., 1999]. At present there is much debate as to whether the pseudogap represents phase-incoherent pre-pairing of the electrons [Ding et al., 1996b, Yang et al., 2008, Nakayama et al., 2009], or whether it is in fact a second gap due to some order (such as a charge or spin density wave) which competes with superconductivity [Le Tacon et al., 2006, Tanaka et al., 2006, Li et al., 2006, Lee et al., 2007, Kondo et al., 2007, Boyer et al., 2007, Ma et al., 2008].

Below T_c is of course the superconducting state. The illustration notes that this is "d-wave" superconductivity, which refers to the symmetry of the gap function in k-space (section 3.3.4). The hole doping corresponding to the highest T_c (the top of the superconducting "dome") is called optimal doping, while to the left and right of that level are termed under- and overdoping, respectively. T_c at optimal doping in Bi2212, the material studied in this thesis, is typically slightly over 90 K.

Toward the heavily overdoped side of the phase diagram, the cuprates exhibit Fermi liquid[3] behavior, which is to say that they act like normal metals with resistivity that scales like T^2 [Iye, 1992]. Above T_c (and/or T^*) but to the left of the Fermi liquid regime is considered a "strange metal" with T-linear resistivity [Iye, 1992].

There are a number of subtleties to the phase diagram: The dip in T_c near 1/8 hole doping is seen in many cuprates [Adachi et al., 2001] and is generally attributed to a phase of alternating "stripes" of holes and antiferromagnetically aligned spins on the Cu sites [Tranquada et al., 1995, Ando et al., 2002]; "QCP" refers to a hypothesized quantum critical point (quantum fluctuation-driven $T = 0$ phase transitions) [Broun, 2008]; The dashed line of T^* is meant to signify that the

[3] Fermi liquid theory will be addressed (very cursorily) in later chapters on an as-needed basis.

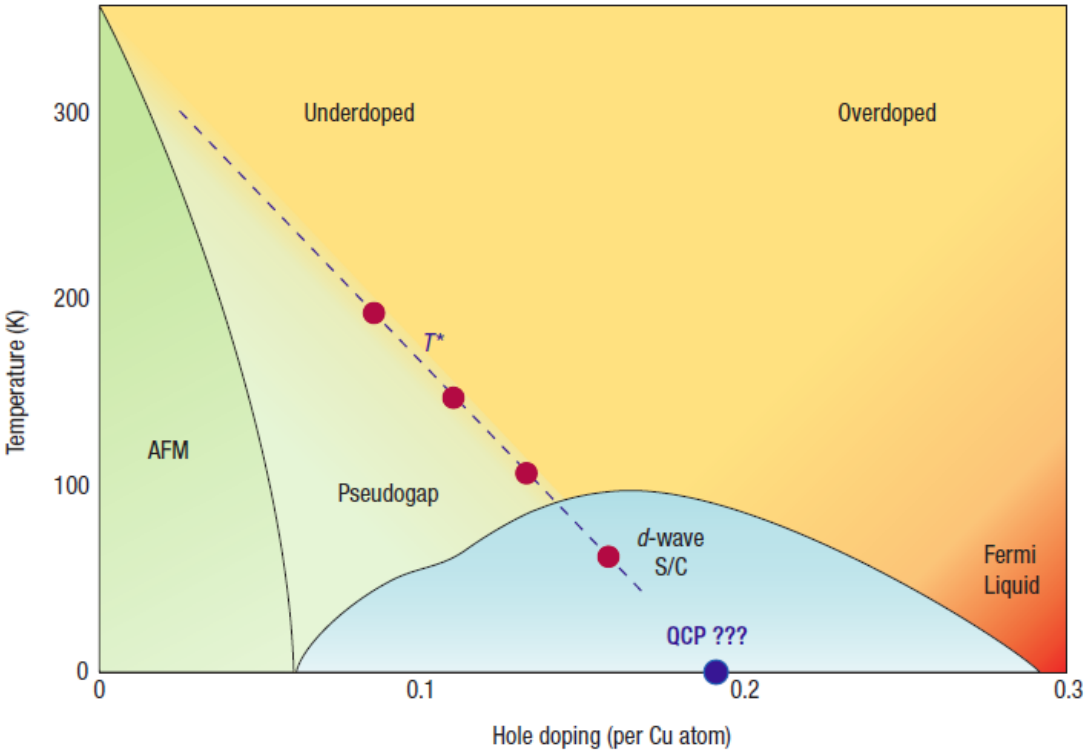

Figure 3.4: Generic phase diagram of the high-T_c cuprates. AFM = antiferromagnetic (Mott) insulator. QCP = possible quantum critical point. d-wave S/C = d-wave superconductivity (section 3.3.4). From [Broun, 2008]. Reprinted by permission from Macmillan Publishers Ltd., copyright 2008.

exact onset of the pseudogap is not precisely known, nor is the point where the T^* line intersects (or doesn't intersect) with T_c, nor is it clear that the pseudogap regime even constitutes a phase in the proper sense.

Finally, while the studies here will not deal with electron-doped cuprates, they do exist. The electron-doped side of the phase diagram (very) loosely resembles a mirror image of the hole-doped side, except with a larger antiferromagnetic Mott insulator phase, a smaller superconducting dome, and possibly no pseudogap [Orenstein and Vishwanath, 2010].

3.3.3 Fermi surface

The generic 2D Fermi surface of the cuprates is four-fold symmetric and comprised of four corner-centered hole pockets, as sketched in Fig. 3.5. This is a somewhat idealized picture of the Fermi surface, and complications appear in many materials. These are illustrated in Fig. 3.6. The first panel depicts a (π, π)-replica "shadow" Fermi surface commonly observed by ARPES [Aebi et al., 1994, Osterwalder et al., 1995]. It has been argued that the shadow reflects Brillouin zone folding due to antiferromagnetic order [Kampf and Schrieffer, 1990, Langer et al., 1995, Chubukov, 1995, Borisenko et al., 2000], but much evidence has accumulated to suggest that it has a structural origin due to a small orthorhombic distortion of the tetragonal unit cell [Schabel et al., 1998,Koitzsch et al., 2004b, Nakayama et al., 2006, Nakayama et al., 2007, Mans et al., 2006].

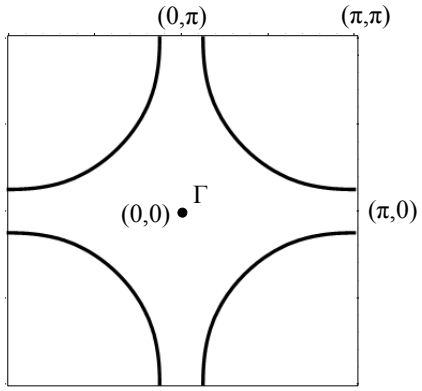

Figure 3.5: Sketch of the generic cuprate Fermi surface.

Another modification to the generic Fermi surface is the appearance of so-called superstructure bands. These bands, shown in the middle panel of Fig. 3.6 are unique to the Bi-based cuprates

and are generally attributed to a superlattice formation due to mismatch between the bismuth- and copper-oxygen planes [Withers et al., 1988, Yamamoto et al., 1990]. In Bi2212 the diffracted Fermi surfaces of the superstructure are found at spacings of $\approx 0.2(\pi, \pi)$ and along only one of the diagonals. In bilayer cuprates such as Bi2212 there is yet another added feature: bonding-antibonding splitting of the band structure due to the close proximity of the bilayer CuO_2 planes [Chuang et al., 2001, Feng et al., 2001, Gromko et al., 2003, Kordyuk et al., 2004, Borisenko et al., 2006, Yamasaki et al., 2007]. This is illustrated in the righthand panel, which is adapted from [Iwasawa et al., 2008].

Fortunately, in the work in chapters 4 and 5, the complications of the shadow and superstructure bands will not come into play due to the region of k-space that will be studied (along the superstructure axis and in the vicinity of the node). Furthermore, a truly fortuitous advantage of performing LE-ARPES on Bi2212 with photon energies in the range of 6–7 eV is that the matrix elements are such that only the antibonding band is visible [Iwasawa et al., 2008], making the data much simpler to analyze.[4] In the nodal region, recent work has indicated that the bonding and antibonding bands behave qualitatively similarly in terms of their dispersion features [Yamasaki et al., 2007, Anzai et al., 2010], and therefore it appears that results obtained from studying the antibonding band alone should largely be applicable to the antibonding as well. We would not be so lucky if we were studying the antinodal k-space region, where bonding and antibonding band dispersions exhibit markedly different behavior [Gromko et al., 2003], or if the photon energy were only slightly (~ 0.5 eV) higher, at which point both bands appear [Yamasaki et al., 2007].

One could be forgiven for assuming that after more than a decade of rigorous study by ARPES, the Fermi surface of the cuprates would be fully and confidently established across the full phase diagram. However, this is not the case. Lately some controversy has surrounded the makeup of the Fermi surface in the underdoped portion of the phase diagram. The dispute stems in large part from quantum oscillation experiments which use very high magnetic fields to observe the Landau levels of electrons orbiting the Fermi surface. From this, in principle, highly precise measurements

[4] Unfortunately, we are so far not aware of any photon energy range capable of isolating just the bonding band.

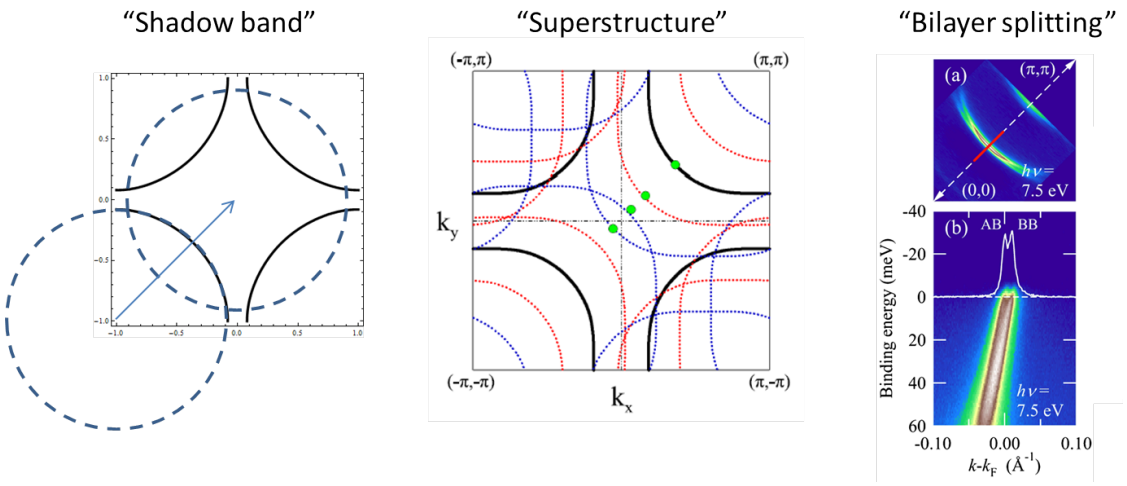

Figure 3.6: Fermi surface complications in cuprates. Left: The (π, π)-replica "shadow" Fermi surface. Middle: Superstructure in Bi-based cuprates. The main (zeroth-order) Fermi surface is shown as solid black curves. The dotted red and blue curves are first- and second-order superstructure-induced Fermi surface replicas, respectively. In Bi2212 the superstructure orders are spaced by approximately $0.2(\pi, \pi)$. Right: Bilayer splitting seen in the first quadrant of the Brillouin zone of Bi2212. The splitting corresponds to bonding (BB) and antibonding (AB) bands of the coupled CuO_2 planes. The righthand panel comes from [Iwasawa et al., 2008]. Reprinted with permission. Copyright 2008 by the American Physical Society.

of the Fermi surface can be made. In underdoped samples, these experiments claim that the hole pockets are much smaller than observed by ARPES [Doiron-Leyraud et al., 2007, LeBoeuf et al., 2007]. At relatively heavy underdoping, ARPES sees a large Fermi surface, or arguably even open, disconnected "Fermi arcs" [Norman et al., 1998, Shen et al., 2005, Kanigel et al., 2006], not small Fermi pockets.[5] While the possibility of a reconstruction of the Fermi surface into small pockets has drawn some theoretical attention [Norman, 2010], a common refrain in the ARPES community is that the quantum oscillation technique is a high-field (10^1–10^2 T) probe that might substantially alter the system under study. In any event, the arc/pocket controversy is a debate still playing out in high-T_c research.

[5] There are some experimental exceptions to this, which have claimed to see evidence for Fermi pockets [Yang et al., 2008, Chang et al., 2008]. One paper in particular made the claim that there are coexisting Fermi arcs and pockets in heavily underdoped La-Bi2201 [Meng et al., 2009]. However, this conclusion has been disputed by King et al., who strongly argue that the supposed pockets have a structural origin [King et al., 2011, Zhou et al., 2010].

3.3.4 *d*-wave gap

The superconducting gap in high-T_c cuprates is anisotropic in k-space. The gap follows a $d_{x^2-y^2}$ symmetry $\Delta(\boldsymbol{k}) = \frac{\Delta_0}{2}|\cos k_x - \cos k_y|$ [Wells et al., 1992, Shen et al., 1993, Ding et al., 1996a]. Data illustrating this symmetry is shown in Fig. 3.7. Conventional BCS superconductors, by contrast, have isotropic gap functions. The *d*-wave function is zero along diagonals of the Brillouin zone and maximal at midpoints of the zone edges. The locations of these zero points and maxima are referred to as nodes and antinodes, respectively.

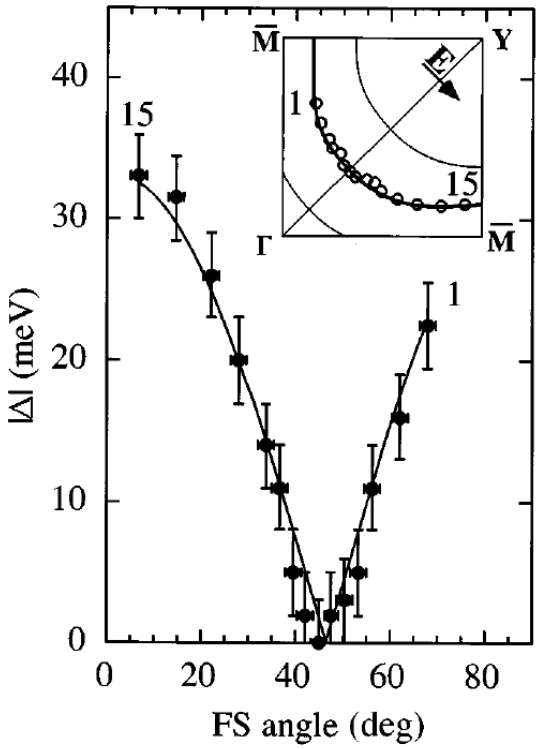

Figure 3.7: *d*-wave symmetry of the superconducting gap. The inset labels the locations of the data points along the Fermi surface. From [Ding et al., 1996a]. Reprinted with permission. Copyright 1996 by the American Physical Society.

The *d*-wave form of the gap reflects an underlying superconducting order parameter of the

same symmetry. This order parameter is the Ginsburg-Landau (pseudo-)wavefunction $\Psi(\boldsymbol{r})$ which describes the local superfluid density $n_s(\boldsymbol{r}) = |\Psi(\boldsymbol{r})|^2$. Various phase-sensitive probes have confirmed the order parameter obeys the $\cos k_x - \cos k_y$ form [Tsuei and Kirtley, 2008].

The d-wave gap symmetry has profound implications for the electron pairing mechanism in cuprates. This can be seen from Eq. 3.4, which intimately connects the form of the pairing potential to that of $\Delta(\boldsymbol{k})$. A counterintuitive result is that when the gap has d-wave form, pairing does not even require that the interaction be attractive. In essence, a fully-repulsive potential can offset the interaction $V(\boldsymbol{k}, \boldsymbol{k'})$ without affecting the conditions for superconductivity in the $d_{x^2-y^2}$ channel [Bulut and Scalapino, 1996, Tsuei and Kirtley, 2008]. By contrast, conventional s-wave superconductivity must be mediated by a attractive interaction.

3.3.5 Energy scales and kinks

A small number of interaction energy scales signalled by ARPES dispersion kinks have been established in the cuprates. Generally these kinks, or mass enhancements/renormalizations, are interpreted as indicators of electrons coupled to bosonic modes — particularly either phonons or spin fluctuations. However, it has also been suggested that kinks could arise due to purely electronic mechanisms in strongly-correlated systems [Byczuk et al., 2007], although presently this does not seem to be a widely-held view. In any regard, as it currently stands, there is not a single kink seen in cuprates whose claimed origin is broadly accepted. Disputes surrounding these dispersion features — including even whether some of them are "real" or mere experimental artifacts — lie at the center of much of the controversy over the theory of superconductivity in cuprates. Presumably if the causes of various dispersion anomalies can be pinned down, we will have advanced a great deal of the way toward finding the interactions behind d-wave pairing and high-T_c superconductivity. Accordingly, chapters 4 and 5 are devoted to analyzing fine details of the dispersion and corresponding self-energy in Bi2212.

Perhaps the most famous of the kinks seen in cuprates is a sizeable dispersion anomaly about 60–70 meV below E_F along the nodal $(0,0)$–(π,π) line [Bogdanov et al., 2000, Lanzara

et al., 2001, Kaminski et al., 2001, Johnson et al., 2001, Gromko et al., 2003]. This kink is shown in Fig. 3.8. By now it is well established that this feature strengthens with decreasing T and decreasing hole doping [Bogdanov et al., 2000, Johnson et al., 2001, Gromko et al., 2003, Borisenko et al., 2006]. Notably, there is some question as to whether this is actually a distinct energy scale of a single interacting mode, or whether it may be comprised of multiple modes (e.g., from separate phonon branches) [Zhou et al., 2005, Meevasana et al., 2006, Lee et al., 2008]. From the ultrahigh-resolution, bulk-sensitive LE-ARPES data presented in this thesis — particularly in Ch. 5 where we investigate the T dependence of the nodal self-energy — there so far is no clear evidence to support the multimode hypothesis. A detailed study of the evolution of this kink around the nodal region of momentum space will be presented in Ch. 4 where some of the analysis regards the kink as a single-mode energy scale.

The kink at 60–70 meV has been explained in terms of either phonon [Devereaux et al., 2004, Ruiz and Badía-Majós, 2009] or spin fluctuation interactions [Manske et al., 2001, Chubukov and Norman, 2004, Inosov et al., 2007a, Dahm et al., 2009]. Experiments have not fared much better than theory in discerning the cause of the kink. For example, a careful LE-ARPES study has noted a small isotope shift of the kink's location [Iwasawa et al., 2008], which supports the phonon explanation. However, as will be discussed in Ch. 4, the k-space evolution of the kink energy and strength is more consistent with spin fluctuations. The cause of this dispersion feature is therefore still strongly debated despite much work.

A much newer discovery of a nodal dispersion anomaly near or below the 10-meV scale is the focus of Ch. 5. This very low-energy kink was first reported by us (in an `arXiv` eprint and later published as [Plumb et al., 2010]) and rapidly independently confirmed by three other groups [Rameau et al., 2009, Vishik et al., 2010, Anzai et al., 2010]. For reasons that will be discussed in that chapter, the observation of this kink required the kind of ultrahigh resolution only recently obtained by the use of LE-ARPES.

Another well-established energy scale at roughly 30–40 meV is seen in ARPES spectra taken near the antinodal $(\pi, 0)$ region [Gromko et al., 2003, Kim et al., 2003]. This kink is shown in

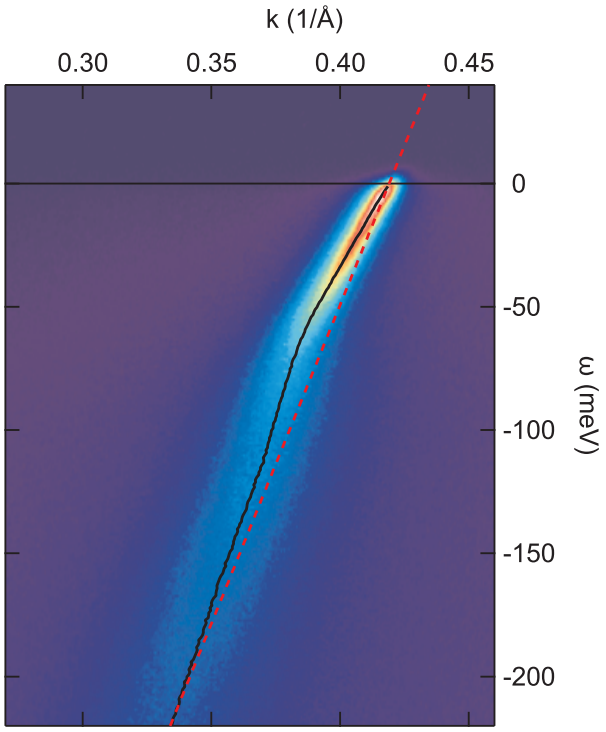

Figure 3.8: Large nodal kink near 60–70 meV as seen in Bi2212 by LE-ARPES. The black curve is the MDC dispersion. The red dashed line is an assumed "bare" band dispersion to highlight the kink. The sample shown is near optimal doping. The data was collected along the $(0,0)$–(π,π) direction with $h\nu = 7$ eV at $T = 10$ K.

Fig. 3.9. As with the 70-meV nodal kink, the antinodal renormalization strengthens below T_c and also appears to intensify with underdoping. Likewise, theories are divided as to whether it results from the coupling of phonons [Devereaux et al., 2004, Cuk et al., 2004] or spin fluctuations [Inosov et al., 2007a, Dahm et al., 2009].

Finally, some other energy scales are suggested by ARPES data but are less clearly established. As alluded to in section 2.6.3, a very large dispersion anomaly is seen at deep binding energy roughly 400 meV below E_F [Graf et al., 2007, Valla et al., 2007], but whether this is a true kink or merely an artifact of complicated ARPES matrix element effects is hotly contested [Inosov et al., 2007b, Inosov et al., 2008, Zhang et al., 2008a, Wang et al., 2009, Basak et al., 2009, Moritz et al.,

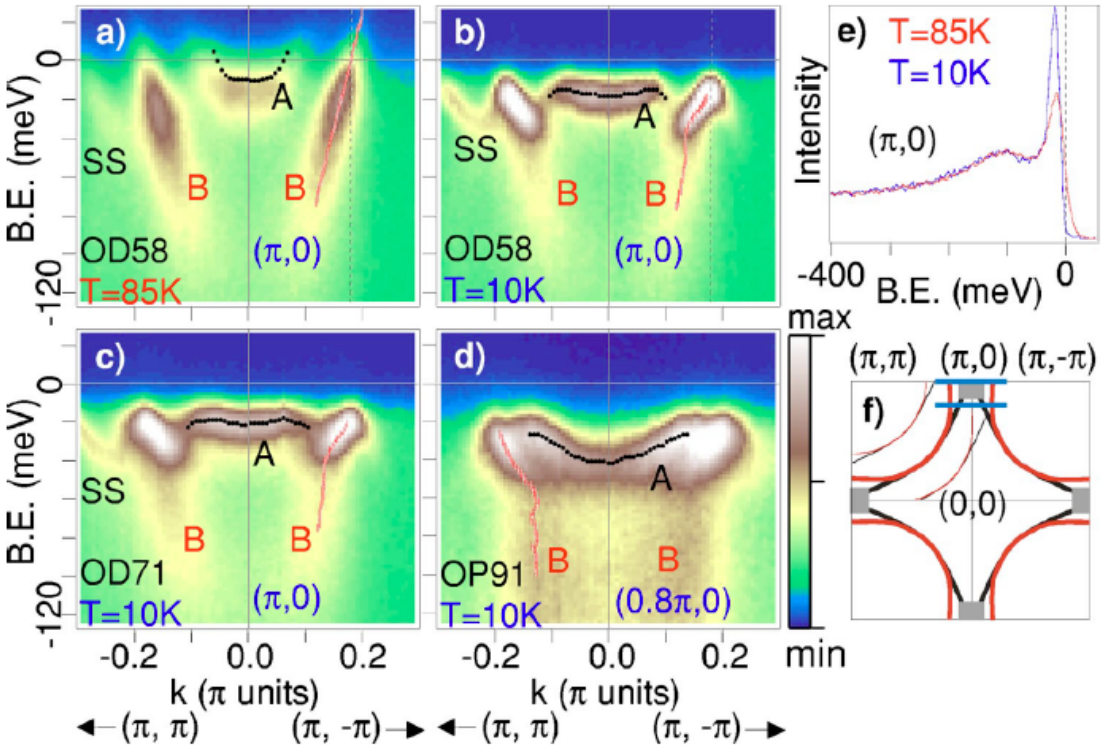

Figure 3.9: Antinodal kink at the 30–40 meV energy scale. (a) ARPES dispersion data from an overdoped ($T_c = 58$ K) Bi2212 sample studied above T_c. (b) The same spectrum below T_c. (c) A less-overdoped sample ($T_c = 71$ K) studied below T_c. (d) An optimally-doped ($T_c = 91$ K) sample studied below T_c and slightly away from $(\pi, 0)$. (e) Antinodal EDC's from panels (a) and (b). (f) Locations of the ARPES image cuts. In all images, "SS" labels superstructure bands and "A" and "B" are bonding and antibonding bands (see section 3.3.3). From [Gromko et al., 2003]. Reprinted with permission. Copyright 2003 by the American Physical Society.

2010]. More recently it has been suggested that there are features in the nodal dispersion located at about 115 meV and 150 meV [Zhang et al., 2008b]. There is some possible confirmation of the 150-meV scale [Anzai et al., 2010], but not of the one at 115 meV.

Chapter 4

Momentum Dependence of the Main Nodal Kink

4.1 Introduction

This chapter presents a detailed study of the momentum dependence of the kink found roughly 60–70 meV below E_F along the nodes of the d-wave superconducting gap in cuprates (section 3.3.5) [Bogdanov et al., 2000, Lanzara et al., 2001, Johnson et al., 2001, Kaminski et al., 2001]. This kink is a large, well-known mass enhancement that is distinct from the smaller, newly-discovered kink near 10 meV (which will be the subject of Ch. 5), and it represents a sizeable feature in the self-energy spectrum $\Sigma(\boldsymbol{k}, \omega)$ of the electrons due to many-body interactions.[1] As a result, there is significant speculation within the high-T_c community that this kink may be a key clue regarding the interactions leading to superconductivity in cuprates, and detailed studies of the kink may shed light on the high-T_c mechanism. While several prior studies of this "main" kink have investigated its evolution in k-space [Kaminski et al., 2001, Ino et al., 2002, Kordyuk et al., 2002, Bogdanov et al., 2002, Kaminski et al., 2005, Graf et al., 2008, Bok et al., 2010, Garcia et al., 2010], none has offered the same combination of detail, resolution, and precision as the data here, nor has previous data been analyzed in quite this same manner.

Using LE-ARPES, we hone our attention on Bi2212 near optimal doping in the superconducting state. Thanks to the ultrahigh-resolution spectra obtainable by the low-energy photons, the energy location of the kink can be precisely traced as a function of momentum in the Brillouin zone. After extracting an effective self-energy $\Sigma_{\text{eff}}(\boldsymbol{k}, \omega)$, LE-ARPES is able to reveal that the peak

[1] For convenience, this chapter will adopt the common convention $\omega = E - E_F$.

in $\Sigma'_{\text{eff}}(\boldsymbol{k}, \omega)$, which corresponds to the location of the kink, smoothly shifts closer to E_F as the spectra progress from the node toward the antinode.

Prompted by our ability to so clearly resolve the kink and its evolution in k-space, we attempt to infer the scattering q-space ($\boldsymbol{q} = \boldsymbol{k'} - \boldsymbol{k}$) dispersion of a boson that might couple to the electrons. This involves considering a variety of simple scattering scenarios while taking care to account for $\boldsymbol{q}$-dependent shifts in the location of the kink that occur in the presence of the d-wave superconducting gap. The extracted q-space dispersions are in relatively poor agreement with most known boson dispersions, with only two notable exceptions: (i) a limited q-space region of overlap with a Cu-O bond-stretching phonon mode and (ii) a resemblance to a high-energy branch of spin fluctuations.

The data is analyzed in further detail by studying the intensity and sharpness of the self-energy of the main kink as a function of momentum. The height and width of the peak in Σ'_{eff} is roughly a constant over much of the near-nodal region but begins to rise sharply for momenta more than about 10° from the node [measured about (π, π)]. In terms of the energy of an assumed bosonic mode, this rise occurs somewhat close to a magnetic "resonance" peak seen in inelastic neutron scattering experiments. However, the energy scale of the resonance does not overlap perfectly with the intensification of Σ'_{eff}, signalling that if spin fluctuations are at play, they may not be the only contribution to the kink.

As will be discussed, these findings are somewhat surprising in light of previous experimental and theoretical work that strongly suggested it might be phonons, not spin fluctuations, that are responsible for the nodal main kink. The new results cloud this picture and may be considered somewhat paradoxical in the sense that they do not clearly point toward a sole mechanism behind the kink. Thus our study opens the possibility that both types of coupling may be relevant to the kink and the physics of the nodal electrons.

4.2 The effective self-energy in the nodal region

4.2.1 Experimental

The data presented here come from near-optimally-doped Bi2212 with $T_c = 89$ K. The experiments were conducted at HiSOR BL-9A at the Hiroshima Synchrotron Radiation Center, which is equipped with a VG Scienta R4000 analyzer. Data was collected in the superconducting state at $T = 10$ K using 7-eV photons. The total instrumental energy resolution (light source plus analyzer) was determined to be about 7 meV based on fits to the Fermi edge of a polycrystalline gold sample. Due to matrix element effects, the 7-eV photon energy isolates the antibonding band in Bi2212 (section 3.3.3) [Iwasawa et al., 2008], greatly simplifying the analysis of the spectra. Data was collected along the nodal $(0,0)$–(π,π) sample orientation, which was determined by Laue diffraction. Excellent rotational alignment of the sample was later confirmed by analysis of the momentum-space symmetry of various parameters such as the Fermi momenta $\boldsymbol{k_F}$, band velocities, and gap values.

4.2.2 k-space evolution of the self-energy

The k-space region of study is illustrated in Fig. 4.1(a), which shows the data collected in the first quadrant of the Brillouin zone.[2] The thicker black lines are sketches of the antibonding (AB) and bonding (BB) bands in Bi2212 based on a tight-binding model [Markiewicz, 2004]. As already discussed, the 7-eV photons observe only the antibonding band. The angle θ with respect to the node and measured about (π,π) will serve as a convenient index of the position along the Fermi surface. Two representative slices of the data labeled **i** and **ii** (corresponding to $\theta = 0.9°$ and $\theta = 16.3°$, respectively) are indicated by the red curves.

The data from each cut is analyzed as shown in Fig. 4.1(b). The black curves show the dispersions, which are the peak positions found from Lorentzian MDC fitting (section 2.6.1). The red dashed lines, meanwhile, are effective bare bands that will be used to extract the effective

[2] Some interpolated points have been added to the Fermi surface plot, especially since the cuts become slightly canted in momentum as a result of the k-space transformation (section 2.3).

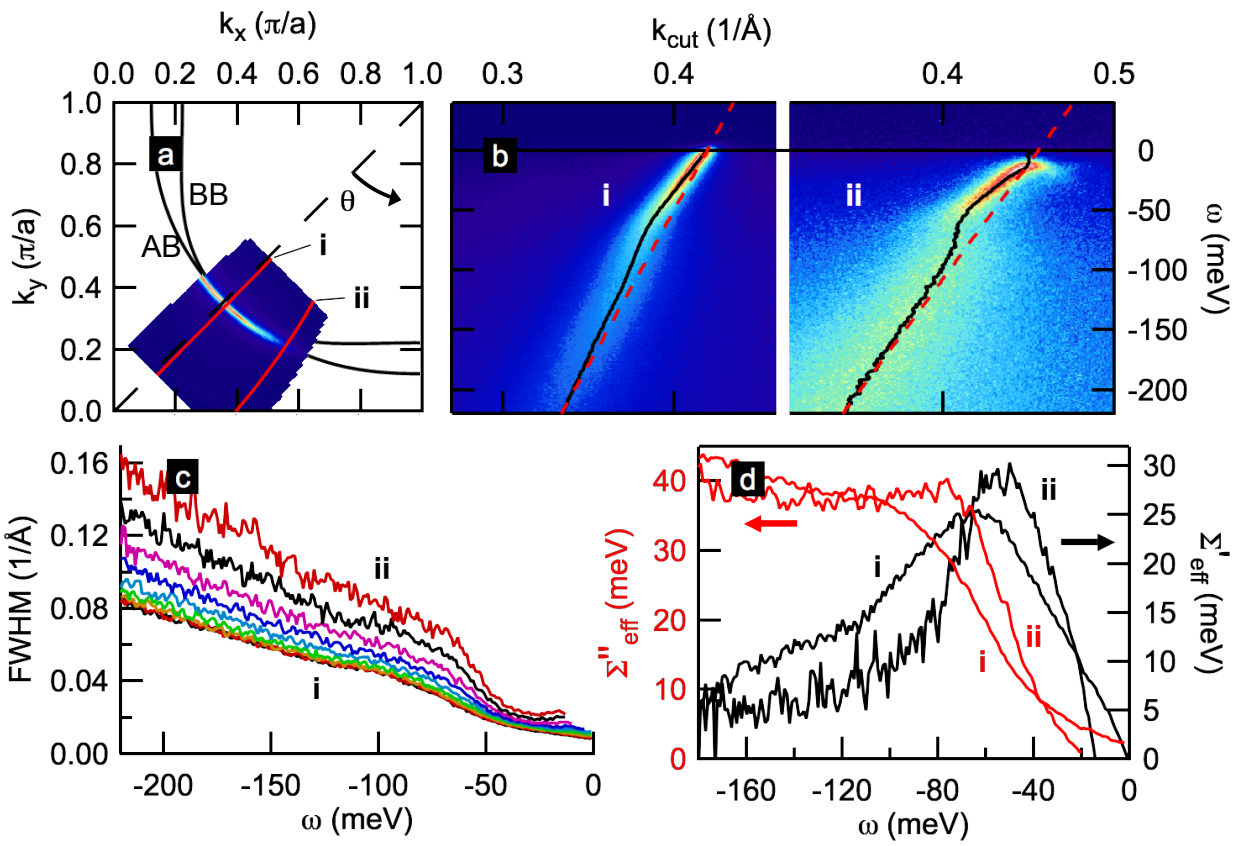

Figure 4.1: Momentum evolution of the nodal dispersion in Bi2212. (a) First quadrant of the Brillouin zone in Bi2212, showing the region of study. The color scale is the measured spectral intensity 10 meV below E_F. Two representative cuts (**i** and **ii**) are indicated by red curves. The black curves are sketches of the antibonding (AB) and bonding (BB) Fermi surfaces. The use of 7-eV photons isolates the antibonding band. Cuts are indexed by the angle θ relative to the node. (b) Raw ARPES data from cuts **i** and **ii**. The solid black curves are the dispersions determined by the peak positions from MDC fitting, while the dashed red lines are the effective noninteracting bands used to extract the self-energy Σ_{eff}. (c) The spectra of MDC widths (red) at cuts progressing away from the node. (d) Real and imaginary components of the effective electronic self-energy [Σ'_{eff} (black, right axis) and Σ''_{eff} (red, left axis), respectively] for cuts **i** and **ii**.

self-energy Σ_{eff} as described in section 2.6.2. Each effective bare band is determined by performing a linear fit to a deep-energy portion of the dispersion (-230 to -200 meV). The fit is constrained to pass through the Fermi momentum k_F.

The momentum dependence of the kink is reflected in multiple aspects of the data self-consistently. Fig. 4.1(c) shows MDC width spectra for each slice progressing from cut **i** to **ii**. Each

spectrum has a prominent step-like rise, and these steps move toward E_F and sharpen as the cuts move from node to antinode. To first-order in the fully non-interacting bare dispersion, the MDC widths are proportional to the total imaginary self-energy $\Sigma''(\boldsymbol{k},\omega)$, which itself is proportional to the scattering rates (inverse lifetimes) of the states (section 2.6.2). Hence, these spectra indicate an acute onset of scattering which coincides with the kink. We should therefore see similar behavior in the effective self-energy, and this is in fact what is observed.

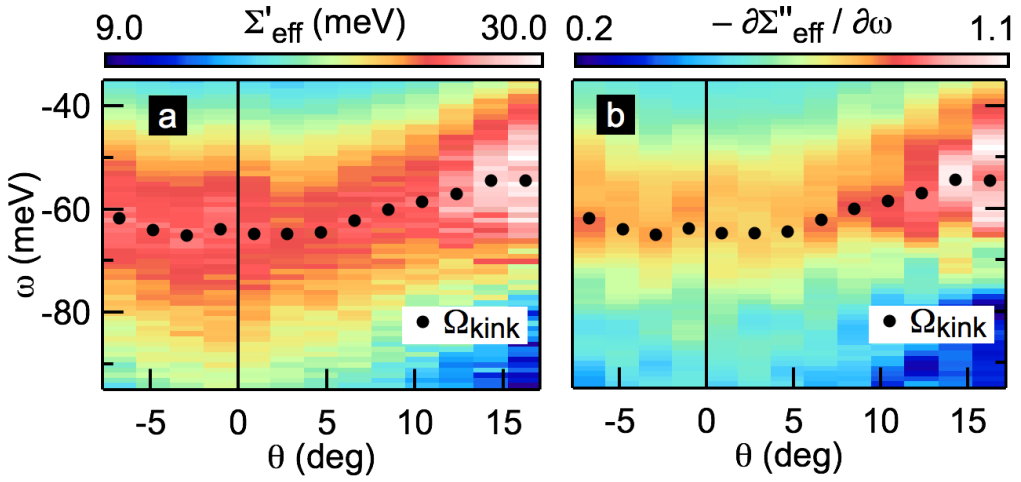

Figure 4.2: Momentum dependence of $\Sigma_{\rm eff}(\omega)$ in the nodal region of Bi2212. In each panel the horizontal axis θ is the Fermi surface angle illustrated in Fig. 4.1(a). The markers specify the energy of the kink $\Omega_{\rm kink}$ determined by the location of the peak in $\Sigma'_{\rm eff}(\omega)$ for each θ. Panel (a) is the spectrum of $\Sigma'_{\rm eff}(\theta,\omega)$, while (b) shows $\partial\Sigma''_{\rm eff}(\theta,\omega)/\partial\omega$. A small offset of the peak in (b) relative to $\Omega_{\rm kink}(\theta)$ arises due to smoothing used to analyze the derivative.

Extracted curves for $\Sigma'_{\rm eff}(\boldsymbol{k},\omega)$ from cuts **i** and **ii** are displayed as black curves (right axis) in Fig. 4.1(d). The corresponding $\Sigma''_{\rm eff}(\boldsymbol{k},\omega)$ are computed from these curves by Kramers-Kronig transformation.[3] These are plotted in red (left axis). Consistent with the behavior of the MDC

[3] The transformation in this case assumes that the spectrum is symmetric about E_F (particle-hole symmetry). The results were checked against a different algorithm which simply extrapolates the endpoints as constants, rather than assuming any symmetry, and the spectra were found to be qualitatively very similar. To improve the results, "bad"

widths in panel (c), the peaks (steps) of $\Sigma'_{\rm eff}(\omega)$ [$\Sigma''_{\rm eff}(\omega)$] shift closer to E_F and sharpen. The $\Sigma''_{\rm eff}(\omega)$ spectra are essentially flat-topped steps, indicating that we have succeeded in removing the large sloping background of slow-moving contributions to the full $\Sigma''(\omega)$ inferred from the MDC widths. This signifies that the analysis has done a good job of isolating just the portion of the self-energy that is due to some sharp mode. We note that the maximum height of $\Sigma''_{\rm eff}(\boldsymbol{k},\omega)$ is roughly independent of $\boldsymbol{k}$, even though the step behavior sharpens approaching the antinodal region. Meanwhile, $\Sigma'_{\rm eff}(\boldsymbol{k},\omega)$ likewise sharpens, and the height of the peak increases away from the node. This is (by construction) Kramers-Kronig-consistent with the behavior of $\Sigma''_{\rm eff}(\boldsymbol{k},\omega)$.

Figure 4.2(a) shows the full behavior of $\Sigma'_{\rm eff}(\omega)$ as a function of the Fermi surface angle θ. The locations of the effective $\Sigma'_{\rm eff}(\omega)$ peaks, $\Omega_{\rm kink}$, are indicated by the black markers. These peak positions are determined by fitting a quadratic curve to points ± 15 meV around the highest point in each spectrum. Notably, the height of the self-energy peak is roughly constant in the immediate vicinity of the node, but begins to rise significantly for $\theta \gtrsim 10^\circ$. This corresponds with a sudden sharpening of the step in $\Sigma''_{\rm eff}(\boldsymbol{k},\omega)$, illustrated in Fig. 4.2(b), which shows $\partial\Sigma''_{\rm eff}/\partial\omega$ as a function of θ and ω.[4]

Before concluding this section, it is worth pointing out that the quantity $\partial\Sigma''_{\rm eff}/\partial\omega$ is — under normal circumstances, at least — closely related to the Eliashberg electron-boson coupling spectrum $\alpha^2F(\boldsymbol{k},\nu)$, where ν is the bosonic energy parameter. Strictly speaking, $F(\nu)$ is the phonon density of states, and $\alpha^2(\boldsymbol{k},\nu)$ contains the electron-phonon interaction matrix elements. However, these are often regarded as a single parameter. It is defined as

$$\alpha^2F(\boldsymbol{k},\nu) = \frac{1}{(2\pi)^3}\int \frac{d\boldsymbol{q}}{v_F}|g(\boldsymbol{k},\boldsymbol{q})|^2\delta[\nu - \Omega_\eta(\boldsymbol{q})] \tag{4.1}$$

where v_F is the Fermi velocity, $\Omega_\eta(\boldsymbol{q})$ is the boson dispersion of a branch indexed by η, and $g(\boldsymbol{k},\boldsymbol{q})$ is the screened electron-boson matrix element [Mahan, 2000].

In a gapless system at $T = 0$, $\alpha^2F(\boldsymbol{k},\nu)$ is related to the self-energy contribution due to

data points in $\Sigma'_{\rm eff}(\omega)$ from energies inside the gap ($|\omega| < \Delta(\boldsymbol{k})$) are set to zero before calculating the Kramers-Kronig transform. The calculated $\Sigma''_{\rm eff}$ spectra were checked for consistency by transforming them back into $\Sigma'_{\rm eff}$.

[4] To reduce noise in the derivative, the $\Sigma''_{\rm eff}(\omega)$ spectrum at each θ was first smoothed by multiplying its FFT by a squared Hann window and then applying the inverse Fourier transform.

electron-boson coupling by

$$\Sigma''(\boldsymbol{k},\omega) = \pi \int_0^{|\omega|} d\nu \alpha^2 F(\boldsymbol{k},\nu) \tag{4.2}$$

[Allen, 1971, Mahan, 2000]. Hence $\partial\Sigma''_{\text{eff}}/\partial\omega$ (measured at low T) is usually very similar to $\alpha^2 F(\boldsymbol{k},\nu)$.

An experimental determination of $\alpha^2 F$ from ARPES would be of substantial value, because it neatly encodes the bosonic interactions into a quantity that can be readily applied to the strong coupling theory of superconductivity. Some papers have attempted to extract this quantity in cuprates [Schachinger and Carbotte, 2008, Bok et al., 2010]. It is critical to note, though, that the presence of a single-particle gap Δ renders the electronic and bosonic energy scales — ω and ν, respectively — inequivalent. This will be discussed in subsequent sections and especially in appendix A. For the situation of an anisotropic gap $\Delta(\boldsymbol{k})$, as encountered in cuprates, the situation is even more complicated, and the correct calculation of $\alpha^2 F$ from the data becomes quite difficult. Thus, while $\partial\Sigma''_{\text{eff}}/\partial\omega$ in Fig. 4.2(b) is in some respect an $\alpha^2 F$-like quantity, we will not attempt to pursue this line of quantitative analysis.

4.3 Electron-boson interactions

4.3.1 Mapping the interactions in q-space

In this section we hope to exploit the high resolution of LE-ARPES in order to infer the q-space dispersion of a mode coupled to the electrons. A crucial yet easily overlooked aspect of the analysis is the correct assignment of boson energies $\Omega_{\text{boson}}(\boldsymbol{q})$ from kink energies $\Omega_{\text{kink}}(\boldsymbol{k})$. In the present case, this is not straightforward — i.e., generally it cannot be assumed that $\Omega_{\text{boson}}(\boldsymbol{q}) \neq -\Omega_{\text{kink}}(\boldsymbol{k})$. In appendix A it is argued that due to the d-wave gap, a boson $\Omega_{\text{boson}}(\boldsymbol{q})$ that scatters electrons within the region around the node by $\boldsymbol{q} = \boldsymbol{k'} - \boldsymbol{k}$ leads to a self-energy feature in ARPES roughly located at

$$\Omega_{\text{kink}}(\boldsymbol{k}) = -\Omega_{\text{boson}}(\boldsymbol{q}) - \Delta(\boldsymbol{k'}). \tag{4.3}$$

This can be understood by considering the lifetime of a photohole injected into the sample at $\boldsymbol{k}, \omega$. We are interested in the electrons which can decay to this state via emitting a boson $\Omega_{\text{boson}}(\boldsymbol{q})$. If the photohole's energy is $\omega(\boldsymbol{k}) > -\Omega_{\text{boson}}(\boldsymbol{q}) - \Delta(\boldsymbol{k'})$, then there is no suitable electron state available for decay, and the hole will have infinite lifetime, meaning $\Sigma'' = 0$ for this hole excitation. On the other hand, for $\omega(\boldsymbol{k}) < -\Omega_{\text{boson}}(\boldsymbol{q}) - \Delta(\boldsymbol{k'})$, electrons can make the transition to the hole, meaning the holes in this energy range have finite lifetimes (i.e., $\Sigma'' > 0$). This leads to a step in $\Sigma''(\omega)$ located at the energy given by Eq. 4.3, as well as a corresponding feature in $\Sigma'(\omega)$. Again, a more in-depth discussion of this phenomenon is presented in appendix A. Recently it has been argued that the true value of $\Omega_{\text{kink}}(\boldsymbol{k})$ may differ slightly from Eq. 4.3 for realistic boson modes with finite energy width [Schachinger and Carbotte, 2009], but this effect is expected to be small and should not alter our results at the qualitative level.

In order to properly correct the gap-shifting of the kinks observed by ARPES, the weighted $\boldsymbol{q}$'s of all the boson scattering channels would have to be known a priori. In lieu of this information, we can proceed by assuming some reasonable form for the $\boldsymbol{q}$-dependence of electron-phonon coupling. In particular, we will consider simple scattering scenarios along symmetries of the Brillouin zone [$\boldsymbol{q} = (\xi, 0, 0)/(0, \xi, 0)$ and $(\xi, \xi, 0)$], as depicted by the arrows in the inset of Fig. 4.3(a).[5] Under these assumptions, $\Delta(\boldsymbol{k'}) = \Delta(\boldsymbol{k})$, and thus the boson energy is simply

$$\Omega^*_{\text{boson}}(\theta) = -\Omega_{\text{kink}}(\theta) - \Delta(\theta) \tag{4.4}$$

where the asterisk (*) denotes that the value is only applicable under these special circumstances. This quantity is plotted in Fig. 4.3(a) along with the original values of $\Omega_{\text{kink}}(\theta)$ obtained from the peak positions of $\Sigma'_{\text{eff}}(\theta, \omega)$. The inset shows the assumed scattering directions connecting like-valued regions of the d-wave gap. Measurements of the gap amplitude used to compute $\Omega^*_{\text{boson}}(\theta)$ are shown in panel (b).

It is fair to ask whether the classes of scattering vectors shown in the inset of Fig. 4.3 are indeed reasonable guesses for the dominant electron-boson couplings, or whether there is even any

[5] In the notation for $\boldsymbol{q}$ vectors, ξ has reciprocal lattice units in terms of $2\pi/a$ such that $-0.5 \leq \xi \leq 0.5$ in the reduced zone scheme. We will assume two-dimensionality and set the z-axis to zero by convention.

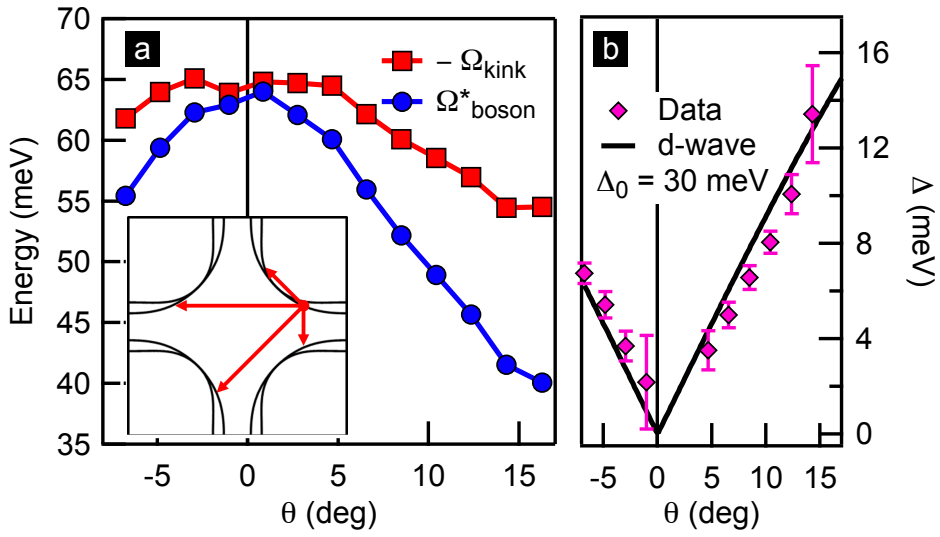

Figure 4.3: Boson energies under assumed scattering scenarios. (a) For scattering directions depicted in the inset, $\Omega^*_{\text{boson}}(\theta)$ reduces to Eq. 4.4. (b) Measurements of the d-wave gap.

dominant scattering channel in the first place. In response to this, we first note that the nodal kink is a reasonably sharp feature of the dispersion, with no substantive evidence from LE-ARPES to suggest that the peak in Σ'_{eff} is somehow comprised of closely-spaced subpeaks that would indicate coupling to multiple modes with comparable weights (see, e.g., Ch. 5 and Fig. 5.3).[6] [7] Thus, the assumption that there is a single dominant electron-boson interaction in the nodal region seems reasonable.

As for the natural criticism that the scattering may not occur predominantly along one of the directions we have assumed, we note that calculations of the electron-phonon matrix elements for various phonon modes find that the scattering is often quite anisotropic over the Fermi surface and frequently exhibits a preference along one of the simple directionalities that were assumed for

[6] There is an additional feature at the 10-meV scale (Ch. 5), and possibly others at deeper energy [Zhang et al., 2008b], but these are too far removed from the main kink energy scale to figure into the present analysis.

[7] As noted in section 3.3.5, some studies using conventional ARPES have claimed that the main nodal kink contains contributions from multiple modes [Zhou et al., 2005, Meevasana et al., 2006, Lee et al., 2008], but these supposed features are extremely subtle, and they have not been convincingly observed so far by LE-ARPES, which has superior resolution.

calculating $\Omega^*_{\rm boson}(\theta)$ (i.e., horizontal/vertical or diagonal in the Brillouin zone). Some examples of these matrix element calculations are shown in Fig. 4.4. There is also some experimental evidence to suggest highly directional phonon scattering by a particular phonon of interest, which will be discussed later and is featured in Fig. 4.6. Furthermore, for the case of spin fluctuations, the scattering should be strongly concentrated along diagonal directions, since the dispersion of the magnetic excitations is confined around the antiferromagnetic wavevector $\boldsymbol{q} = (0.5, 0.5)$ [Tranquada et al., 2004, Hayden et al., 2004, Pailhès et al., 2004, Reznik et al., 2004]. One final argument boils down to "There is no harm in trying". That is to say, if analysis of a particular assumed scattering direction obtains results that are consistent with other experiments and/or theoretical expectations, then there is a case to be made a posteriori that perhaps the assumption, for whatever reason, was not so bad after all.

Having obtained $\Omega^*_{\rm boson}$ in the previous section under some simplifying assumptions, we can now map this quantity into q-space along the various horizontal/vertical and diagonal scattering directions that we have already explicitly assumed. This is shown in Fig. 4.5. In addition to horizontal/vertical scattering, there are two forms of diagonal scattering that are considered: inter- and intra-hole-pocket $\boldsymbol{q}$'s that have long and short wavevectors, respectively. These four scenarios are depicted in panel (a). Panels (b)-(d) show the dispersions of $\Omega^*_{\rm boson}(\boldsymbol{q})$ for each of the assumed coupling directionalities. For comparison, $-\Omega_{\rm kink}(\boldsymbol{q})$ is shown as well. The extracted boson dispersion is directly compared to phonons observed by inelastic neutron scattering (INS) on $YBa_2Cu_3O_{6+x}$ (YBCO) where $x = 0$ (down triangles) and $x = 1$ (up triangles) [Reichardt, 1996], as well as phonons measured by inelastic x-ray scattering (IXS) on Bi2212 (diamonds) [Graf et al., 2008]. Panel (d) additionally features a portion of the high-energy branch of incommensurate spin fluctuations (SF) observed in Bi2212 by INS [Xu et al., 2009]. This dispersion, as well as the Bi2212 Cu-O bond-stretching (BS) phonon dispersion in (b), are highlighted (green and pink shading, respectively) and will be discussed in depth shortly.

For interpreting Fig. 4.5(b), the extracted dispersions for Horiz and Vert should be viewed as "limiting cases" in the sense that each represents a pure scattering directionality. Since $(\xi, 0, 0)$ and

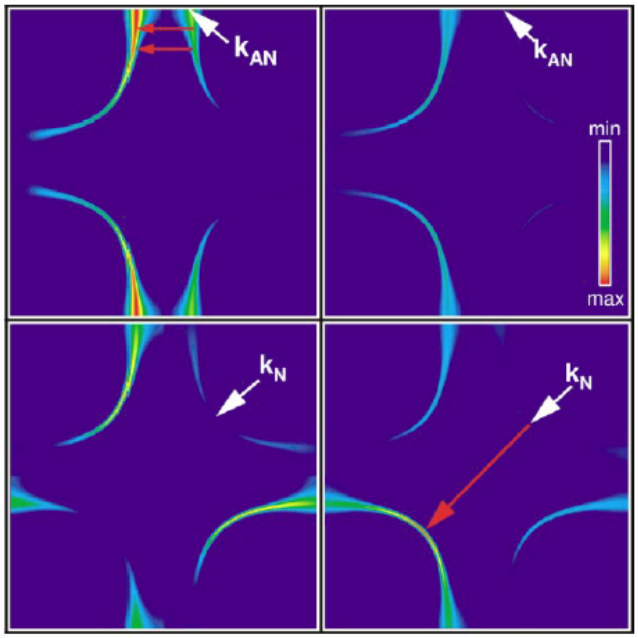

Figure 4.4: Calculations of electron-phonon matrix elements. The lefthand panels are the scattering matrix elements for a Cu-O bond "buckling" mode, while the righthand panels show the calculations for a Cu-O "breathing" (bond-stretching) mode. Top (bottom) sets of panels show the scattering for an electron beginning at the antinode (node). The key point in the context of the present analysis is that even for relatively complicated scattering matrix elements such as these, often there is still a tendency toward a preferred, simple scattering directionality (e.g., roughly horizontally or diagonally for a nodal electron scattered by the buckling or breathing mode, respectively). From [Devereaux et al., 2004]. Reprinted with permission. Copyright 2004 by the American Physical Society.

$(0, \xi, 0)$ are equivalent, these types of scattering should happen simultaneously, perhaps with some complicated q dependence of the ratio of the relative contributions to the kink from each scattering direction. However, based on the pure Horiz and Vert dispersions of $\Omega^*_{\rm boson}(\boldsymbol{q})$, it is difficult to imagine how the behavior of the nodal kink could be explained in terms of most of the various phonon branches in Fig. 4.5(b).

In fact, in general very little qualitative agreement is found between $\Omega^*_{\rm boson}(\boldsymbol{q})$ and most of the boson dispersions in Fig. 4.5. We can point to only two areas of reasonable correspondence. The first of these is the $\boldsymbol{q} \approx (0.3, 0, 0)$ portion of the Cu-O BS phonon in Fig. 4.5(b) which overlaps

with $\Omega^*_{\rm boson}(\boldsymbol{q})$. The other is the strongly dispersing character of $\Omega^*_{\rm boson}(\boldsymbol{q})$ in the inter-hole-pocket scattering scenario, which qualitatively resembles that of the the spin fluctuation branch.

We now turn our focus to a discussion of the two highlighted dispersions in Fig. 4.5(b) and (d). The phonon dispersion emphasized by pink shading in Fig. 4.5(b) is noteworthy for a number of reasons. This is a Cu-O bond-stretching phonon that is observed to anomalously "soften" in many materials [Pintschovius, 2005, Reznik, 2010], which refers to the fact that its dispersion features a sharp energy drop (and corresponding broadening) in an analogy with kinks seen in ARPES. Hence this is a signature of strong electron-phonon coupling.[8] Additionally, a LE-ARPES study of oxygen-isotope substituted Bi2212 found an isotope shift in the energy location of the nodal main kink, with the size of the shift suggesting that the Cu-O bond-stretching mode was most likely to be responsible [Iwasawa et al., 2008]. It was furthermore recently noted that this phonon branch crosses (or possibly anti-crosses) with a longitudinal optical phonon in Bi2201 [Graf et al., 2008], which is also shown in Fig. 4.5(b). This crossing point is roughly $\boldsymbol{q} = (0, 0.22\text{–}0.25, 0)$ and at an energy of ~ 60 meV. The authors state that the $\boldsymbol{q}$ vector where the phonon branches cross connects points on the Fermi surface where a sudden "crossover" jump occurs in the the location of the main ARPES kink [Graf et al., 2008, Garcia et al., 2010] — a claim that is contradicted by the data here, which shows a smooth evolution of $\Omega_{\rm kink}$ around the Fermi surface. Finally, INS has observed that the bond-stretching phonon dispersion is substantially broader at optimal doping than at overdoping at points along the horizontal and vertical q-space directions [Reznik, 2010] (Fig. 4.6). This suggests that at optimal doping the mode couples electrons relatively strongly along $(\xi, 0, 0)/(0, \xi, 0)$ and perhaps is associated in some way with superconductivity.

For all the reasons just mentioned, it seemed especially likely at the outset of our analysis that we might uncover a particularly strong correspondence between the dispersions of $\Omega^*_{\rm boson}(\boldsymbol{q})$ and the Cu-O bond-stretching phonon along $(\xi, 0, 0)/(0, \xi, 0)$. As it turns out, the findings paint a more complicated and nuanced picture. There is some limited region of near-agreement between

[8] Such softening can in fact be seen in the data from the same phonon branch in $YBa_2Cu_3O_7$, which runs alongside the highlighted curve.

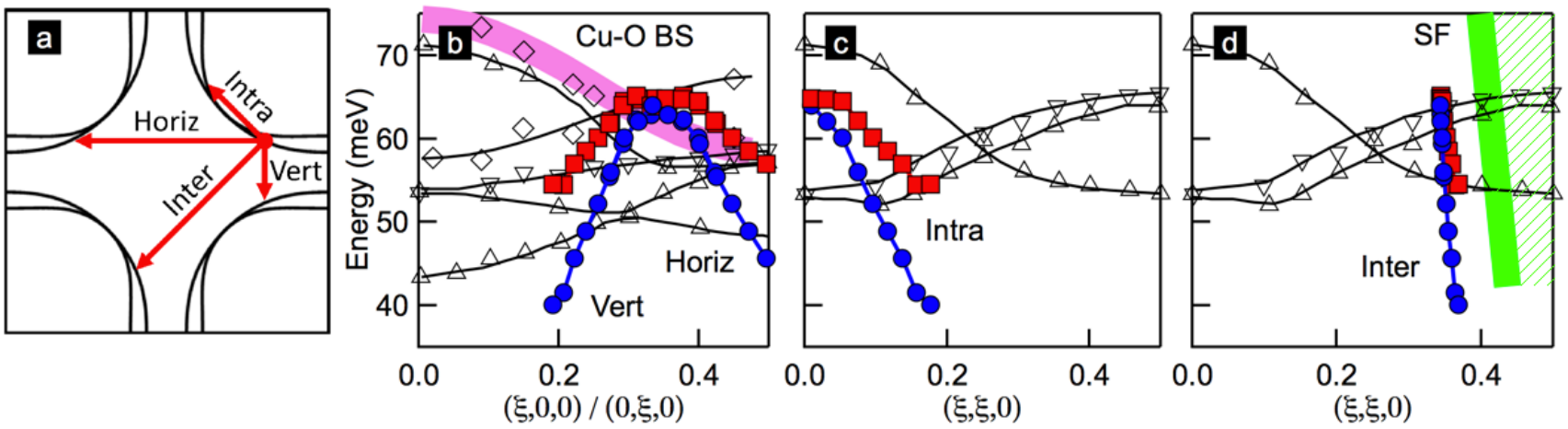

Figure 4.5: q-space dispersions of Ω_{kink} and Ω^*_{boson}. The boson and kink energy dispersions are extracted from ARPES under various assumed scattering scenarios are shown in (a): horizontal (Horiz), vertical (Vert), intra-pocket (Intra), and inter-pocket (Inter). (b) Dispersion of $-\Omega_{\text{kink}}(\boldsymbol{q})$ (filled red squares) and $\Omega^*_{\text{boson}}(\boldsymbol{q})$ (filled blue circles), assuming that scattering occurs horizontally/vertically in the Brillouin zone. The difference between these two dispersions corresponds to the local gap value $\Delta(\boldsymbol{k})$ The extracted dispersions are compared to those of oxygen bond-stretching phonons measured by INS in $YBa_2Cu_3O_7$ (up triangles) and $YBa_2Cu_3O_6$ (down triangles) [Reichardt, 1996], as well as phonons observed by IXS in Bi2201 (diamonds) [Graf et al., 2008]. The pink shading highlights a Cu-O bond-stretching phonon branch in Bi2201 that is of interest for a number of reasons (see text). (c),(d) Analogous plots assuming diagonal intra- and inter-hole-pocket scattering, respectively. The open circles in (d) are the dispersion of the high-energy branch of spin fluctuations (SF) observed in Bi2212 [Xu et al., 2009]. The green shaded curve is a guide to highlight this dispersion. The hatched area indicates that this region is often observed to be filled in with neutron scattering signal, and it is not clear that the SF dispersion is actually well-defined as a sharp dispersion.

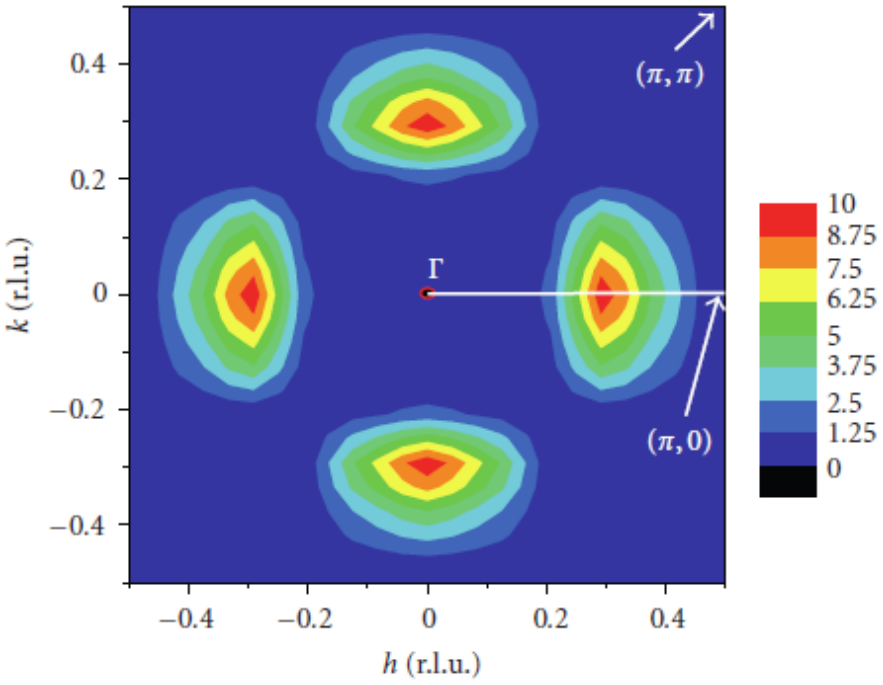

Figure 4.6: Evidence for horizontal/vertical scattering by the Cu-O bond-stretching phonon. The map is a qualitative schematic of the observed change in phonon dispersion linewidths between the optimal and overdoped phase in $La_{2-x}Sr_xCuO_4$. From [Reznik, 2010]. Reprinted with the author's permission.

the two dispersions in the vicinity of $(\approx 0.3, 0, 0)$, but they overall exhibit qualitatively disparate characters. Crucially, had we not attempted to account for the gap-shifting of Ω^*_{boson} relative to Ω_{kink}, we would have been deceived into thinking that there was more similarity between the two dispersions over the region $(0.3\text{–}0.5, 0, 0)$ than actually exists. Meanwhile, considering inter-hole-pocket scattering along $(1, 1, 0)$, there is notable qualitative similarity between the dispersion of $\Omega^*_{\text{boson}}(\boldsymbol{q})$ and that of incommensurate spin fluctuations highlighted by green shading in Fig. 4.5(d). The dispersions move nearly parallel to each other from 65 meV down to about 45 meV. However, as noted by the green hatched region, the SF dispersion is possibly not sharp, and in many data it

appears that the region around $(0.5, 0.5, 0)$ is "filled in" by the neutron scattering signal.

The SF dispersion plotted in Fig. 4.5(d) is actually a high-energy branch of magnetic excitations which merges with a low-energy branch [Tranquada et al., 2004, Hayden et al., 2004, Pailhès et al., 2004, Reznik et al., 2004], as shown in Fig. 4.7. The spin fluctuation branches converge near 30–50 meV at the antiferromagnetic wavevector $\boldsymbol{q} = (0.5, 0.5)$, which corresponds in momentum and energy with a magnetic resonance where INS scattering is strongly peaked [Rossat-Mignod et al., 1991, Mook et al., 1993]. The hourglass shape of the combined dispersions is illustrated in Fig. 4.7 (which emphasizes the shape of the dispersions in 2D q-space and energy) and in Fig. 4.8 (which emphasizes the peaked magnetic response at the resonance point).

By plotting the peak height of Σ'_{eff} as a function of Ω^*_{boson} we observe that the self-energy intensity varies relatively little at high energies but increases dramatically below about 45 meV. This behavior bears a qualitative resemblance to the observed INS response of the magnetic resonance — e.g. the measurements on Bi2212 by Fong et al. [Fong et al., 1999], which are compared to the LE-ARPES data in Fig. 4.9. Additionally, within our simple scattering model, the kink feature in Σ_{boson} sharpens for Ω^*_{boson} near the resonance, which could conceivably be connected to the fact that the SF dispersion flattens as it approaches the resonance peak. This finding supports the notion that the dispersion of Ω^*_{boson} in terms of the inter-hole-pocket coupling direction $\boldsymbol{q} = (\xi, \xi, 0)$ may be related to the high-energy incommensurate spin fluctuations. Notably, this is consistent with the findings of some other recent work [Inosov et al., 2007a, Dahm et al., 2009] which arrived at their conclusions by different means.

4.4 Discussion

The data presented in section 4.2 make some valuable observations that are of general interest to the study of the interactions of the nodal electrons, independent of the model-based analysis presented in section 4.3. In particular, we clearly observe that the main kink energy disperses smoothly toward E_F (by ~ 10 meV) as a function of $\boldsymbol{k}$ as we move away from the nodal region of the Fermi surface. This is in contrast to a previous line of thinking that the energy scales seen at

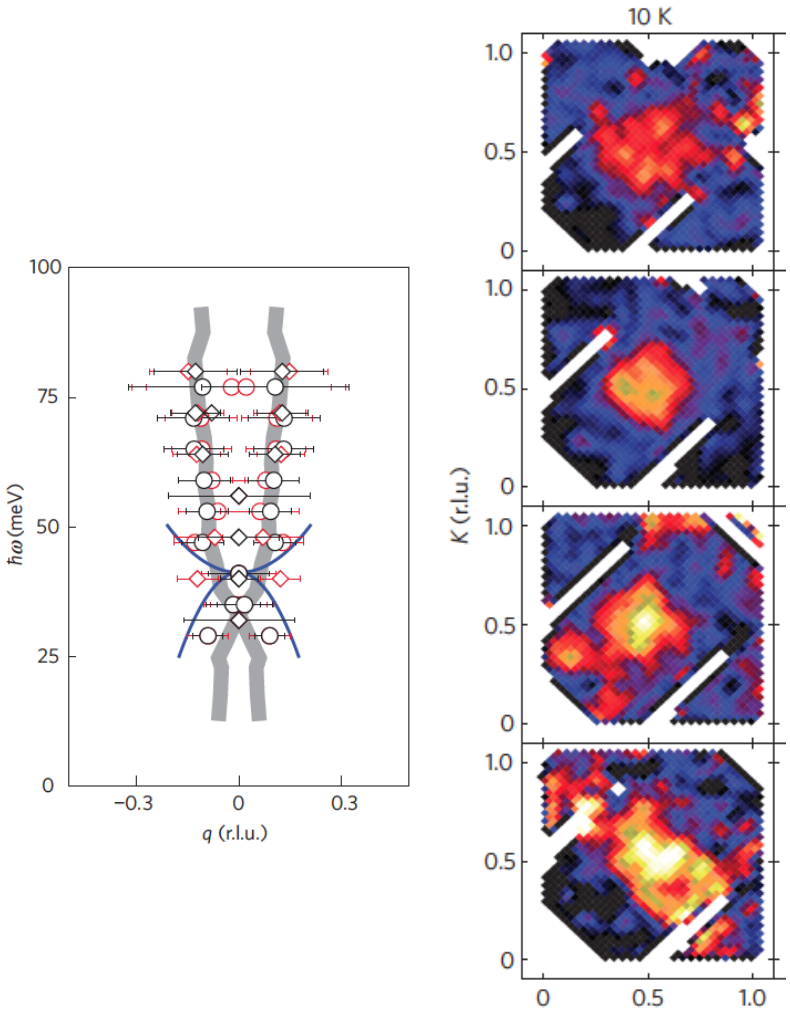

Figure 4.7: INS measurements of the "hourglass" dispersion of spin fluctuations in Bi2212. The data come from Xu et al. [Xu et al., 2009]. Left: Spin fluctuation dispersion branches in optimally-doped Bi2212 ($T_c = 91$ K). The horizontal axis is q with respect to the antiferromagnetic wavevector $(0.5, 0.5, 0)$. The data are averaged over cuts in the $(\xi, 0, 0)$ and $(0, \xi, 0)$ directions, but the authors state that the findings are virtually identical for cuts in the $(\xi, \xi, 0)$ direction. Points from incident neutron energies of 120 and 200 meV are indicated by circles and diamonds, respectively. Black and red symbols are $T = 10$ K and $T = 100$ K, respectively. The results are compared with dispersions from $YBa_2Cu_3O_{6.5}$ (gray shaded curve) [Stock et al., 2005] and $YBa_2Cu_3O_{6.95}$ (thin blue curve) [Reznik et al., 2004]. Righthand panels: q-space maps of the neutron scattering signal at fixed energy transfers. The energies are, from bottom to top, 36, 42, 54, and 66 meV. Taken together, these maps form a 3D perspective of the dispersion in the lefthand panel. The colorscale is the intensity of the imaginary part of the magnetic susceptibility $\chi''(\boldsymbol{q})$, the extraction of which is described in that text. The data were collected at 10 K. Reprinted by permission from Macmillan Publishers Ltd., copyright 2009.

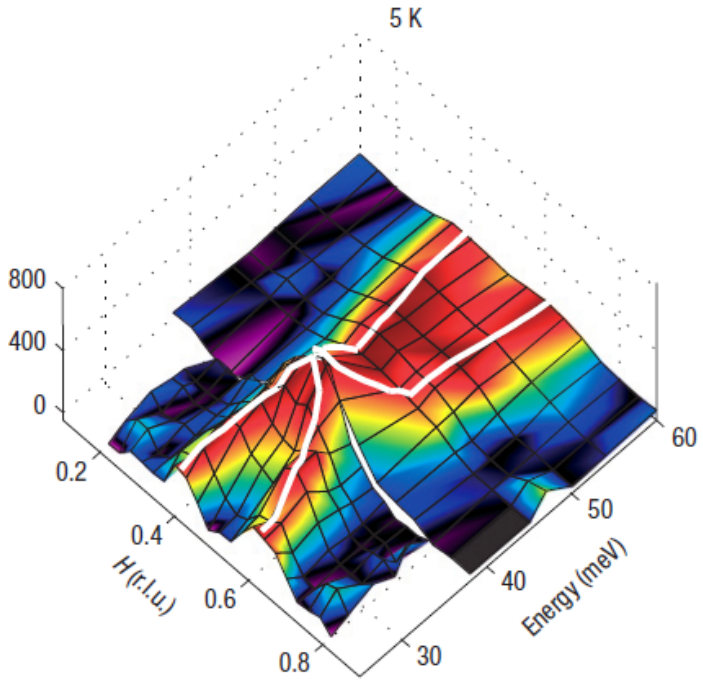

Figure 4.8: Momentum-resolved view of the magnetic resonance in YBCO. The z-axis/color scale represent the neutron scattering intensity. The momentum axis is $(H, -1.5, -1.7)$ in reciprocal lattice units — i.e., the scan is a horizontal cut through the antiferromagnetic wavevector in a higher-order Brillouin zone. The sample, underdoped YBCO, is studied below T_c at 5 K. Above T_c the resonance peak vanishes. From [Hinkov et al., 2007]. Reprinted by permission from Macmillan Publishers Ltd., copyright 2007.

the node and antinode are more-or-less static within their respective neighborhoods of the Fermi surface, possibly to the extent that the energy of the main kink makes a sudden jump at a distinct crossover point in k-space [Graf et al., 2007, Garcia et al., 2010].

However, based on our data, the paradigm of nodal-antinodal crossover is not dead, per se; It perhaps just needs to be characterized in terms of a different set of parameters. As the data shows, the peak in $\Sigma'_{\text{eff}}(\boldsymbol{k}, \omega)$ sharpens and intensifies rather quickly for points along the Fermi

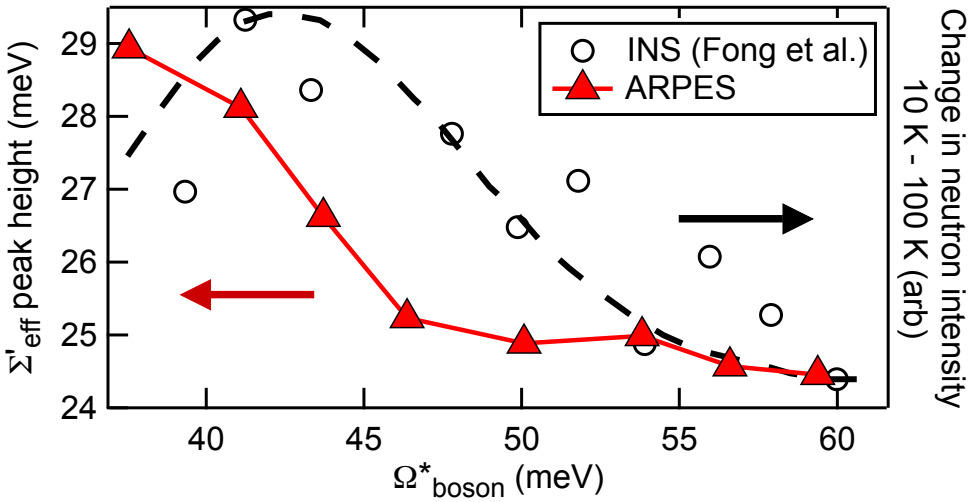

Figure 4.9: Comparison between Σ'_{eff} and the magnetic resonance peak in Bi2212. The peak height of Σ'_{eff} (left axis) is plotted as a function of Ω^*_{boson}. The difference in neutron scattering intensity between 10 K and 100 K in Bi2212 shows the magnetic resonance peak (from [Fong et al., 1999]). This is plotted on the right axis and along the same energy coordinates. The dashed line is a guide to the eye for the INS data.

surface where $\theta \gtrsim 10°$, consistent with a sudden sharpening of the steps in $\Sigma''_{\text{eff}}(\boldsymbol{k}, \omega)$. Whether this behavior constitutes a crossover is maybe a matter of semantics, but it is probably a useful finding nonetheless.

The analysis of the q-space dispersion of the mode energy in sections 4.3 and 4.3.1 relied on two key assumptions: (i) the kink is primarily due to a single interacting boson; and (ii) this interaction scatters electrons predominantly along one of the symmetry axes of the Brillouin zone. An attempt was made to justify these assumptions on various experimental and theoretical grounds. Still, some potentially valid criticisms could be leveled against our approach. For instance, one could propose that phonons should scatter the electrons primarily to the antinodes, since these points are van Hove singularities. In this case, $\Omega_{\text{boson}}(\theta) = -\Omega_{\text{kink}}(\theta) - \Delta_0$, where $\Delta_0 \approx 30$ meV. The kink would then correspond to bosons in the range of roughly 20–30 meV. In cuprates, this energy range is home to a tangled spaghetti of phonon modes [Falter, 2005], and, moreover, the $\boldsymbol{q}$ vectors in this scenario would not fall on a straight line, making the analysis of the problem and comparison to

INS/IXS data a daunting challenge. Therefore there is not much our analysis can say about this type of problem, except that it is a call to theorists to attempt to explain the dispersion of $\Omega_{\rm kink}$ and the momentum dependence of $\Sigma_{\rm eff}$ from phonon theory.

Despite the partial overlap of $\Omega^*_{\rm boson}$ and the Cu-O bond-stretching phonon branch, it is not clear that there is a satisfactory explanation of the kink's k-space evolution in terms of phonons. For instance, Fig. 4.10 shows calculations of the electron-phonon coupling parameter $\lambda(\boldsymbol{k})$ [Devereaux et al., 2004]. This quantity for a given phonon is related to $\alpha^2F(\boldsymbol{k},\nu)$ by $\lambda(\boldsymbol{k}) = 2\int_0^{\omega_D} \frac{d\nu}{\nu}\alpha^2F(\boldsymbol{k},\nu)$ [Mahan, 2000]. The calculations find that the Cu-O bond-stretching mode (labeled "breathing" in the figure)has $\lambda(\boldsymbol{k})$ that is peaked at the node — essentially the opposite of the behavior of the effective self-energy found here, which intensifies toward the antinodes. This is surprising if we recall that the bond-stretching mode is often thought to be responsible for the nodal kink (see discussion in 4.3.1). Meanwhile, the buckling mode (out-of-phase c-axis O vibrations) calculation in the top panel of Fig. 4.10 shows $\lambda(\boldsymbol{k})$ peaked at the antinodes, but this mode has an energy of nominally ~ 40 meV and is believed to couple nodal states primarily across the "necks" of the Fermi surface (see left panels of Fig. 4.4).

In the context of spin fluctuations, the assumptions behind our analysis are quite reasonable, because it is known from experiment that there is only a single dispersion branch at a given energy, and also the scattering is centered about $\boldsymbol{q} = (\pi,\pi)$. The observations in Figs. 4.5 and 4.9 that $\Omega^*_{\rm boson}(\boldsymbol{q})$ and $\alpha^2F(\Omega^*_{\rm boson})$ find some qualitative agreement with the characteristics of the incommensurate spin fluctuations are therefore quite interesting and possibly valid, especially in light of previous work [Inosov et al., 2007a, Dahm et al., 2009].

Finally, our findings are somewhat surprising in light of various prior results suggesting that the main nodal kink originates from electron-phonon interactions. These include, for example, LE-ARPES isotope experiments [Iwasawa et al., 2008], "softened" INS phonon dispersions [Pintschovius, 2005, Reznik, 2010], and theoretical simulations [Devereaux et al., 2004, Ruiz and Badía-Majós, 2009]. In particular, these previous results tend to point toward the Cu-O bond-stretching phonon as the most relevant to the nodal kink. The analysis here paints a picture that

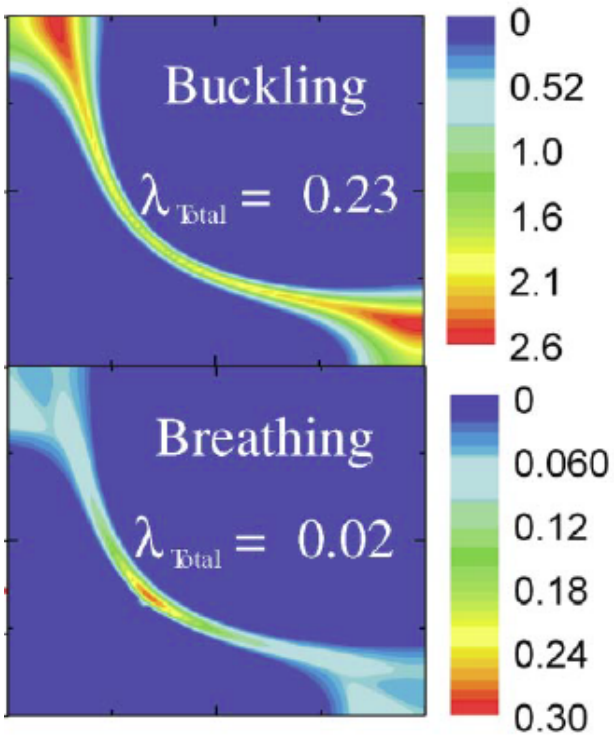

Figure 4.10: Calculations of electron-phonon coupling around the Fermi surface. "Breathing" refers to the Cu-O bond-stretching mode discussed in this chapter. From [Devereaux et al., 2004].

is potentially more complicate and nuanced, finding some possible evidence that both phonons and spin fluctuations contribute to the main kink. Perhaps the discrepancies in these results can be reconciled by the notion that one interaction dominates over the other. For instance, recently Schachinger and Carbotte have argued that the results from the ARPES isotope experiment are actually consistent with phonons being only a small contribution to the overall self-energy [Schachinger et al., 2009]. However, the presence of so much conflicting theory and data may instead hint that the physics of the main nodal kink, and of cuprates in general, is not truly dominated by a single class of interactions but rather arises from phonons and spin fluctuations acting in concert. Theories along these lines [Normand et al., 1996, Nazarenko and Dagotto, 1996, Nunner et al., 1999] eventually may be able to explain the apparent conflicts amongst various results so far.

Chapter 5

A New Energy Scale for Interactions: ~ 10 meV

5.1 Introduction

This chapter describes the discovery of a dispersion kink located roughly 10 meV below E_F along the nodal direction in Bi2212, thus defining a new energy scale for interactions in this material [Plumb et al., 2010]. This energy scale is distinct from others previously seen at the node — in particular the well-established and much larger kink at 60–70 meV which was the subject of Ch. 4 [Bogdanov et al., 2000, Lanzara et al., 2001, Johnson et al., 2001, Kaminski et al., 2001]. The observation of this new dispersion feature and the fine details of its behavior rests heavily on the ultrahigh-resolution, near-intrinsic spectra obtainable by LE-ARPES, and in many ways the results presented here exemplify the enormous potential of this experimental probe.

In optimal and overdoped samples, it is found that the kink abruptly strengthens at a temperature close to T_c, indicating that the interactions causing this dispersion feature may be linked to superconductivity. Moreover, being located so close to E_F, the temperature-dependent behavior of the 10-meV kink has a profound effect on the Fermi velocity, which is the group velocity of the electrons evaluated at the Fermi energy,[1] $v_F = \hbar^{-1}\nabla_{\boldsymbol{k}} E(\boldsymbol{k})\Big|_{E_F}$. In fact, as the temperature is raised, the Fermi velocity is seen to rapidly increase by almost 30% in the vicinity of T_c. Since the onset of this behavior depends on T_c (and hence doping), it defies a previously-held notion that v_F along the nodes of the d-wave superconducting gap is somehow "universal" as a function of doping.

[1] Throughout this work, $\hbar$ will be set to one in the context of velocities, and hence these quantities will be reported in units of energy per momentum (eV $\cdot$ Å).

The observation of the 10-meV kink is far from straightforward, because it turns out that under certain circumstances the MDC fitting results very near E_F can suffer complicated and surprising systematic errors arising from the resolution of the experiment. The resolution effects most strongly influence the very low-T spectra, and they tend to counter the bend of the kink, thus obscuring our view of the physics of this low-lying dispersion feature. This possibly explains why another ARPES group did not manage to clearly identify the kink in 2008, even though they noted a "possible feature" in Σ'' at roughly the same energy scale [Zhang et al., 2008b]. The resolution effects and how to deconvolve them will be discussed at some length, but it will also be shown that LE-ARPES permits direct observation of the kink, in spite of said difficulties, thanks to the probe's exceptional resolution.

Finally, a small number of plausible theories have been proposed to explain the kink's physical origins, while certain other mechanisms can conclusively be ruled out. We will discuss these theories, as well as future directions of study which will hopefully elucidate the physics leading to the kink and any relation it may have to superconductivity.

5.2 Observing the nodal kink near 10 meV

5.2.1 Experimental

The first investigations into the temperature dependence of the low-lying nodal dispersion and the Fermi velocity v_F were performed using the 6-eV laser-ARPES system at the University of Colorado. This system was[2] based on a frequency-quadrupled femtosecond-pulsed Ti:Sapphire laser and used a VG Scienta SES2002 spectrometer [Koralek et al., 2007]. Due to the pulsed nature of this light source, the photon bandwidth was about 5 meV, and total experimental resolution including the analyzer was around 10 meV. Spectra were collected as a function of T along the nodal $(0,0)$–(π,π) direction in Bi2212 at various doping levels. These measurements were able to establish an unusual, nearly-linear temperature dependence of the band velocity near the Fermi

[2] The past tense is emphasized here, because the system has since been altered in several respects. This includes the addition of two (soon to be three) new laser systems, replacement of the main chamber, construction of a new sample manipulator, and an upgrade of the analyzer.

level, and they gave the first hints of a possible low-energy dispersion anomaly.

Later data which more fully revealed the 10-meV kink was collected at SSRL BL5-4 using 7-eV synchrotron light. The endstation is equipped with a VG Scienta R4000 analyzer. The beamline monochromator and the analyzer settings were configured to have total energy resolution $\Delta E = 3.2$ meV (FWHM). Fits to the Fermi edge of polycrystalline gold determined an energy resolution of about 4 meV, in close agreement with the expectation based on the instrument settings.[3] The samples studied were optimally-doped ($T_c = 91$–92 K) and overdoped ($T_c \approx 62$ K) Bi2212.

In all these experiments, data was collected in the nodal $(0,0)$–(π,π) orientation, which was determined to within about 1° by Laue diffraction. The matrix elements of the 7-eV photons isolate just the antibonding band of the bilayer system (section 3.3.3), which simplifies the dispersion analysis, allowing us to obtain highly trustworthy results. The dispersions were analyzed by standard Lorentzian MDC fitting (section 2.6.1). In the attempts to establish the existence of the 10-meV kink, we were afraid that the presence of even a small gap in the spectra could lead to a false identification of a dispersion anomaly. Hence, we went to great lengths to ensure that the spectra were aligned precisely at the node. The node was determined by verifying the momentum dependence of various parameters such as the Fermi momentum k_F, the deep-energy band velocities, and the leading edges of the k-integrated spectra, which were all in good agreement. This last parameter, the leading edge, is determined by fitting a Fermi-Dirac distribution to the k-integrated weight for each spectrum. As a stand-in for a true gap value measurement (which is substantially more involved when done properly [Reber et al., 2010b]), it does a good job of locating the minimum of the gap, and hence the node. It should be noted that in our investigations of Bi2212, it appears that the gap along (π,π) is extremely small (< 1 meV) [Reber et al., 2010b], if not identically zero, which is consistent with other experimental probes and theoretical expectations [Tsuei and Kirtley, 2008]. Thus, we can confidently state that the observed kink near 10 meV is not in any way an

[3] Minor differences between the expected resolution and its measured value frequently occur, with the measured value typically found to be slightly larger than the expected one. The exact cause of the discrepancies is not known, but they probably arise from a combination of factors such as uncertainty about the precise temperature of the gold sample, small additional electronic noise, and/or surface contaminants that scatter the photoelectrons and broaden the Fermi edge.

artifact of a gap being present in the spectrum.

The raw 2D ARPES data, MDC analysis, and node determination are illustrated in Fig. 5.1. Panel (a) shows the spectrum from an optimally-doped Bi2212 sample studied with photon energy $h\nu = 7$ eV at $T = 10$ K. Nodal determination (in this case by leading edge analysis) is shown in (b).

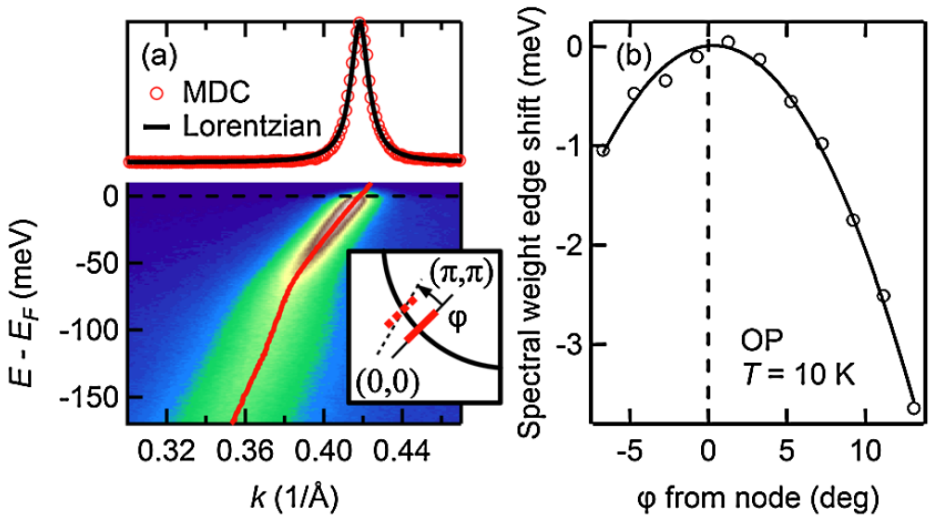

Figure 5.1: LE-ARPES data at the node in Bi2212. (a) Raw data from an optimally-doped sample at $T = 10$ K. The red curve shows the dispersion determined from Lorentzian MDC fitting, which is illustrated in the top axes for the MDC at E_F. The inset shows the positions of the cuts in the Fermi surface. (b) The leading edge of the k-integrated spectral weight is determined for the ARPES cut at each point on the Fermi surface at angles φ from the node (see inset), allowing precise determination of the nodal cut to within better than 1° of the true node. From [Plumb et al., 2010].

5.2.2 Direct observation of the 10-meV kink

As mentioned in the introduction to this chapter, there are complications arising from the experimental resolution which tend to distort the MDC fitting results in such a way that the 10-

meV kink can be hidden. These effects will be discussed in the next section. In the meantime, here we will demonstrate that LE-ARPES can actually directly observe the kink despite these effects, thanks to its ultrahigh resolution.

Figure 5.2 shows data from an optimally-doped sample at $T = 50$ K. In addition to v_F, we note the slightly deeper-energy band velocity v_{20}. Formally, v_F is determined by linear fit to the MDC dispersion over the region $E_F \pm 5$ meV. Meanwhile v_{20} is determined by fitting from 30 meV to 10 meV below E_F. These definitions will be used throughout this chapter, since, as can be seen in the figure, they provide a convenient means of identifying the 10-meV kink. Based on the change in slope from v_{20} to v_F, the kink can be identified at a low energy that is nominally referred to throughout this thesis as "10 meV" (although in actuality it is probably slightly lower).

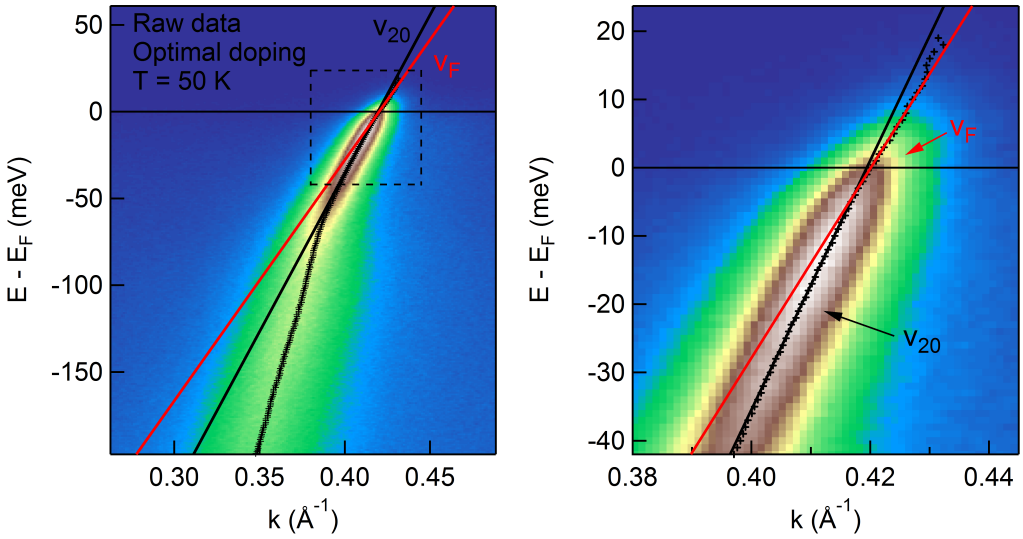

Figure 5.2: Direct observation of the nodal 10-meV kink at $T = 50$ K. The images show raw data from optimally-doped Bi2212. The right panel highlights the region indicated by the dashed box on the left. In each panel, the MDC dispersion is indicated by black markers. The extended lines show the slopes corresponding to v_F (red) and v_{20} (black). The Fermi velocity v_F is determined by performing a linear fit to the MDC peak locations over the range $E_F \pm 5$ meV. At slightly deeper energy, v_{20} is found by fitting a line to the peak locations from 30 meV to 10 meV below E_F. The intersection of these slopes shows a kink at low energy, nominally referred to as "10 meV".

Studies of the temperature dependence of the nodal dispersion further illustrate the existence

of a low-energy kink. Figure 5.3 illustrates some key aspects of the T-dependent behavior. In order to analyze this data in terms of an effective self-energy (section 2.6.2), a linear effective bare band is chosen so as to connect portions of the dispersion which are roughly temperature-independent [panel (a)]. While this band — which is quite similar to the one adopted in Ch. 4 — is obviously not the fully noninteracting dispersion, it is at least bare with respect to any strongly temperature-dependent interactions. Using this band, the effective $\Sigma'(E)$ can be extracted for various temperatures shown in panel (b). It is clear from these data that the behavior of the large "70-meV" kink dominates the self-energy. However, looking at the difference in $\Sigma'(E)$ above and below T_c (at 130 K and 70 K, respectively) shown on the upper axis, it is clear that there is a smaller temperature-dependent feature near 10 meV (arrow). As one expects, a corresponding temperature dependence at both the 70- and 10-meV energy scales can be seen in the effective $\Sigma''(E)$ [panel (c)].[4]

Before moving on, it should be noted that Fig. 5.6 and Fig. 5.3(a)–(b) only present data for $T \geq 70$ K. As we shall see in the next section, this range, unlike colder temperatures, does not suffer to any significant degree from resolution-induced errors in the MDC peak locations. As for Fig. 5.3(c), simulations such as those in appendix B find that the difference in MDC width spectra as a function of temperature should not be significantly affected by the resolution, so the key finding of panel (c) is unchanged. Subsequent sections will deal with resolution complications. It turns out that for the experimental resolution of this study, these issues ought to be taken into account for dispersion measurements at $T \lesssim 50$ K.

5.2.3 Dispersion measurement distortions due to resolution

While Lorentzian MDC fitting is a powerful technique for the analysis of dispersions in ARPES, there is a set of circumstances in which the reliability of the results breaks down. Recently the ARPES community is gaining appreciation of the fact that MDC (and EDC) peaks can deflect

[4] The effective $\Sigma''(E)$ here is simply the MDC half-widths multiplied by the effective bare band velocity. As noted in section 2.6.2, this is not as proper as performing a Kramers-Kronig transformation of the effective $\Sigma'(E)$ as was done in Ch. 4. However, since we are really interested in just the change in $\Sigma''(E)$, this minor simplification presents no problem.

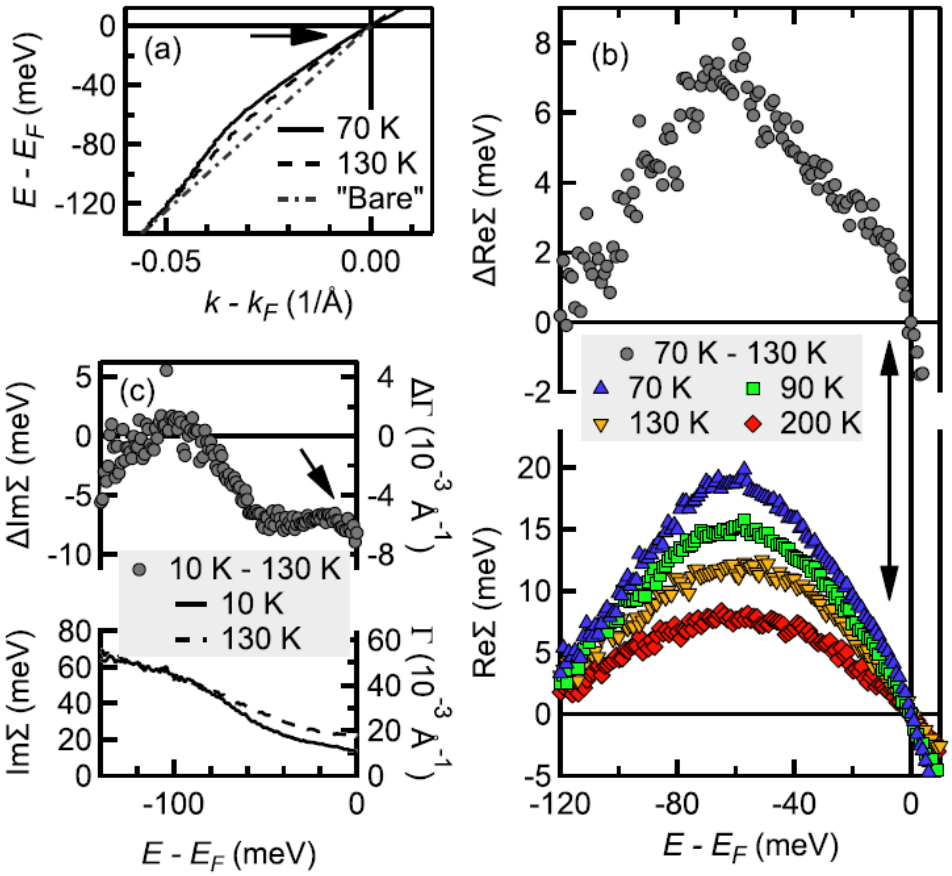

Figure 5.3: 10-meV kink seen in the temperature dependence of the nodal dispersion. (a) Nodal dispersions in optimally-doped Bi2212 below and above T_c. The assumed "bare" dispersion is used to extract an effective self-energy (section 2.6.2) of the sharp energy scale feature. The location of the new kink is indicated by the arrow. (b) Effective $\Sigma'(E)$ as a function of temperature. A bump corresponding to the 10-meV can be seen in the change from 130 K to 70 K (arrow). (c) Change in effective $\Sigma''(E)$ between 130 K and 10 K, calculated from multiplying the MDC half-widths by the slope of the bare band. A feature can again be seen near the 10-meV scale. From [Plumb et al., 2010].

away from the true dispersion when fits are being attempted in the vicinity of a sharp transition in spectral weight [Ingle et al., 2005]. Such a situation routinely occurs at very low temperatures and very near E_F. The problem stems from the experimental resolution. To illustrate how this happens, consider the extreme limiting case shown in Fig. 5.4. The straight black line in the left panel shows a perfectly sharp (i.e., $\Sigma = 0$) linear band at $T = 0$. By convolving this ideal dispersion with an energy resolution (red curves), it is transformed into the image on the right. (For smoothness of the results, a small amount of k resolution has been simulated as well.) Looking at the righthand panel, there are now counts above E_F where previously there had been none. The above-E_F counts are asymmetrically distributed, because there is is no contribution coming from $k > k_F$. The result is that the MDC peaks (red) are deflected to lower $|k|$ in the vicinity of E_F.

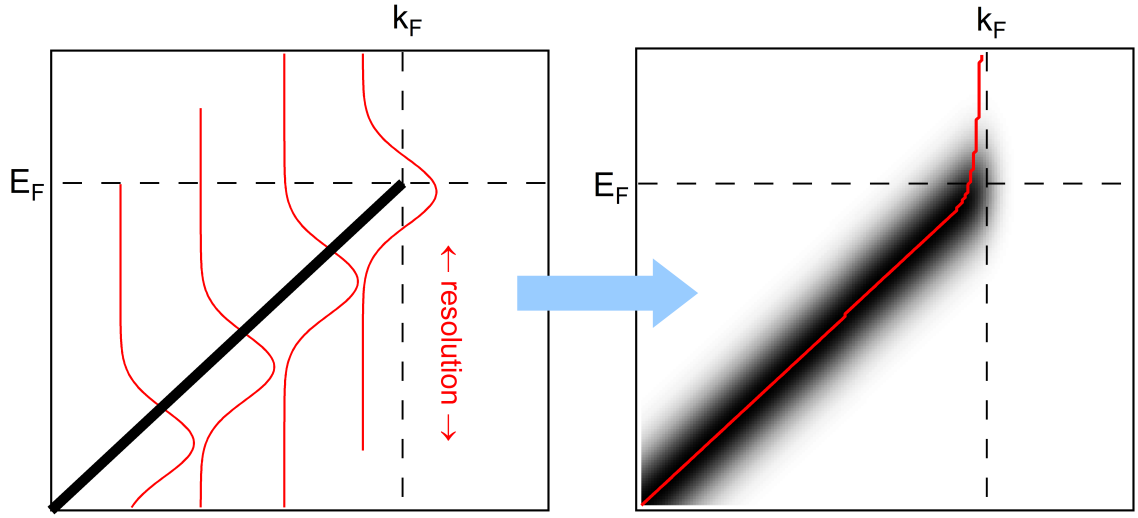

Figure 5.4: Understanding the resolution effect in MDC fitting. The left panel shows an ideal, infinitely sharp, linear dispersion at $T = 0$. Convolving it with an energy resolution, shown in red, (plus a small small amount of momentum resolution for smoothness) produces the image in the right panel. The resolution causes the MDC peaks (red curve on right) to deflect to lower $|k|$.

From this illustration, it is hopefully clear that the deflection will become more dramatic as the energy resolution is broadened, since this will more severely spread counts up above E_F. On the other hand, raising the temperature will counter the effect of the resolution, since this will

introduce counts beyond k_F which will tend to pull the peaks back toward the true dispersion. Another way to picture this is to imagine the $T \to \infty$ limit, in which case the dispersion crosses E_F with no cutoff, and hence the resolution effects vanish. The net result is that resolution effects are really only a concern for roughly $T \lesssim \Delta E/k_B$, where ΔE is the energy resolution in terms of full-width at half-maximum (FWHM). Moreover, the dispersion is generally only affected at energies approaching or above the onset of the Fermi transition, loosely characterized as $E - E_F \gtrsim -2k_BT$. (This final point was not really accurately illustrated by the thought experiment of Fig. 5.4 due to setting $T = 0$.)

LE-ARPES, with its excellent energy and momentum resolution, is therefore an ideal tool for studying the near-E_F dispersion at very low temperatures. However, resolution can never be fully banished from the experiment, and even many of the best LE-ARPES measurements typically have 3–5 meV of total energy broadening (light source plus analyzer) and angular resolution of about 0.2°. Even under these high-resolution conditions, one finds that v_F measurements below ~ 50 K remain somewhat afflicted by the artificial deflection of the MDCs, although the problem is far less severe than for conventional ARPES. For LE-ARPES, the small resolution broadening can be substantially and reliably removed by deconvolution techniques, as we will show in subsequent sections. This is less likely to be the case for conventional ARPES, since any deconvolution technique will naturally have "farther to go" to reduce the resolution and uncover the underlying spectrum. This presumably increases the likelihood that the output of the algorithm will contain errors. Moreover, compared to LE-ARPES, data from ARPES at conventional photon energies contains more background from extrinsically scattered electrons (Ch. 2.7). Like resolution, this background could potentially affect the measured near-E_F dispersion in complicated ways, but it obviously will not be removed merely by attempting to deconvolve the resolution.

5.2.4 Deconvolution and the Richardson-Lucy Technique

Experimental resolution is a so-called point-spread function which convolves with the underlying spectrum and smears it. Once noise is added to this smeared spectrum, the problem

of deconvolution is said to be ill-posed, meaning that there are multiple underlying spectra that could reasonably be proposed as solutions. Many flavors of deconvolution exist, and the differences between them largely boil down to how one defines the criteria for the most reasonable solution.

For removing the resolution from ARPES spectra, it is necessary to use a 2D image deconvolution on the raw E-vs.-angle data. In the results shown here, we employed the Richardson-Lucy (RL) algorithm [Richardson, 1972,Lucy, 1974]. This technique historically has been popular in the astronomy and medical imagining communities but was recently adopted for ARPES analysis [Yang et al., 2008]. The method is rooted in Bayesian probability analysis, a discussion of which lies well outside of the intended scope of this thesis. Let it suffice to say that the algorithm tries to iteratively determine the underlying image $M_{i,j}$ that is most likely to have led to the measured image $\widetilde{M}_{i,j}$ given the resolution $R_{i,j}$ and assuming Poisson-distributed noise (which is appropriate for counting experiments such as ARPES). The RL algorithm reduces to an amazingly concise routine:

$$M_{i,j}^{(k+1)} = \left\{ \left[\frac{\widetilde{M}_{i,j}}{M_{i,j}^{(k)} \otimes R_{i,j}} \right] \otimes R_{j,i} \right\} M_{i,j}^{(k)} \tag{5.1}$$

where $k = 0, 1, 2 \ldots$ is the iteration number, and $\otimes$ signifies convolution.

In the RL implementation used to analyze our data, the initial guess $M_{i,j}^{(0)}$ was set to a constant, and the stopping criterion was signalled by the convergence $\left\langle |M_{i,j}^{(k)} - M_{i,j}^{(k-1)}|/M_{i,j}^{(k-1)} \right\rangle < 0.01$, where the angle brackets represent the mean. The resolution was treated as a 2D Gaussian in energy and angle. For the input to the deconvolution algorithm, we actually used the calculated value of the energy resolution (3.2 meV), rather than the slightly higher measured value (4 meV, see section 5.2). This was precautionary, since the lower value will alter the measured data the least, thus assuring that any observed kink is in fact real. By contrast, "over-deconvolving" the data via a too-large value of ΔE could result in an artificial near-E_F kink. Similarly, the input for the angular resolution was 0.2°, which is roughly a best-case resolution claimed by the instrument manufacturer [VG Scienta AB, 2009].

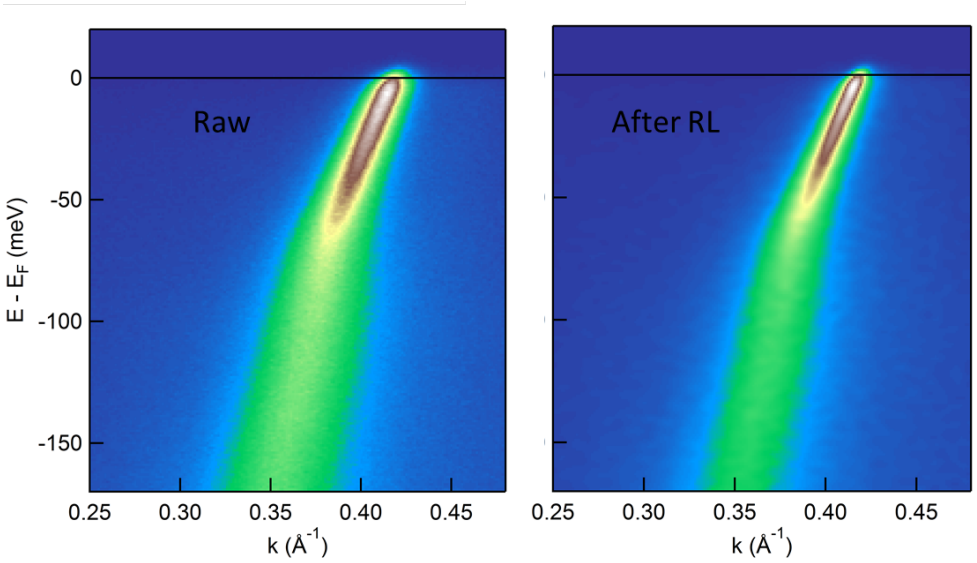

Figure 5.5: Richardson-Lucy deconvolution applied to ARPES data. The raw data on the left was collected at the node of optimally-doped Bi2212. The output of the RL routine is shown at right. The deconvolution was performed prior to transforming the image to k-space with energy resolution of 3.2 meV and angular resolution of 0.2°.

5.2.5 Full temperature dependence of the kink behavior

After applying the RL deconvolution, the artificial deflection of the MDC peaks is largely removed from the spectra, and it becomes possible to quantitatively analyze the dispersion at all energies and temperatures. Figure 5.6 illustrates this by showing the values of v_F and v_{20} in the optimal (OP) and overdoped (OD) samples before and after the RL routine. (v_{20} was defined in section 5.2.2.) As expected, the raw measurements of v_{20} are essentially unchanged after removing the resolution, but the values of v_F get revised downward for $T \lesssim 50$ K (section 5.2.3). This corrects a small upturn in v_F at low T that would otherwise make $v_F(T)$ inexplicably non-monotonic, potentially calling the results into question.

v_F and v_{20} exhibit similar linear temperature dependence above T_c that diverges at low T. The ratio v_{20}/v_F can be regarded as an indicator of the strength of the 10-meV kink. This quantity

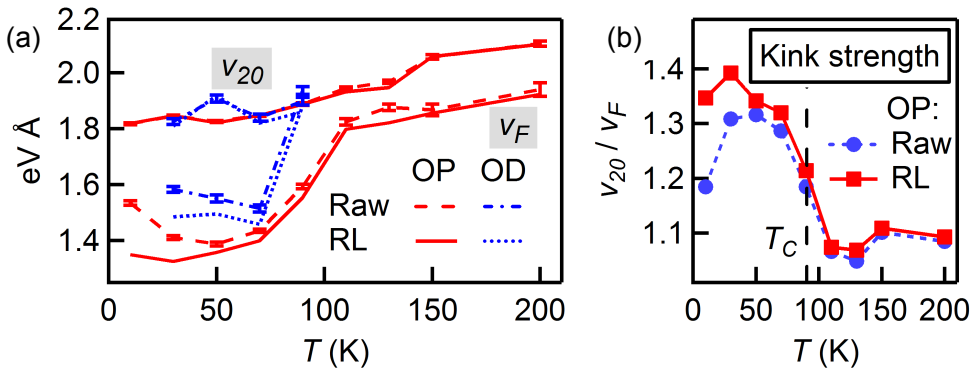

Figure 5.6: Temperature and doping dependence of low-energy band velocities and kink strength. (a) The upper data points are raw and RL-deconvolved values of v_{20} for the optimal (OP) and overdoped (OD) samples. The lower data points are corresponding values for v_F. (b) The ratio v_{20}/v_F can be taken as an indicator of the strength of the 10-meV kink. Raw and RL-deconvolved values of the kink strength in the OP sample are shown. The kink appears to have an onset related to T_c. From [Plumb et al., 2010].

is plotted in Fig. 5.6(b) for the optimally-doped sample, where it becomes clear that the kink suddenly turns on close to T_c. It is trivial to infer from panel (a) that the kink in the overdoped sample has an onset at a lower temperature, roughly consistent with its T_c of about 62 K.

Likewise, as in Fig. 5.3, the kink can be observed in the temperature dependence of $\Sigma'(E)$. This is shown in Fig. 5.7, which looks at the change in $\Sigma'(E)$ relative to the spectrum at 130 K for the optimally-doped sample. In addition to the obvious feature of the 70-meV peak, a bump near 10-meV (indicated by the arrow) begins to form at about 90 K (roughly T_c), grows to full-scale by about 70 K, and persists at all lower temperatures.[5]

To wind down this discussion of the data, we note that based on the results in this section, it appears that the RL deconvolution has rectified the low-T, near-E_F data in a manner that is clarifying, consistent with expectations, and not too dramatic. These aspects of the analysis are all very reassuring. In addition, corrections of v_F based on simulations of the data qualitatively agree

[5] Some small ripple can been seen in this plot, which was introduced by the deconvolution but does not qualitatively alter the results.

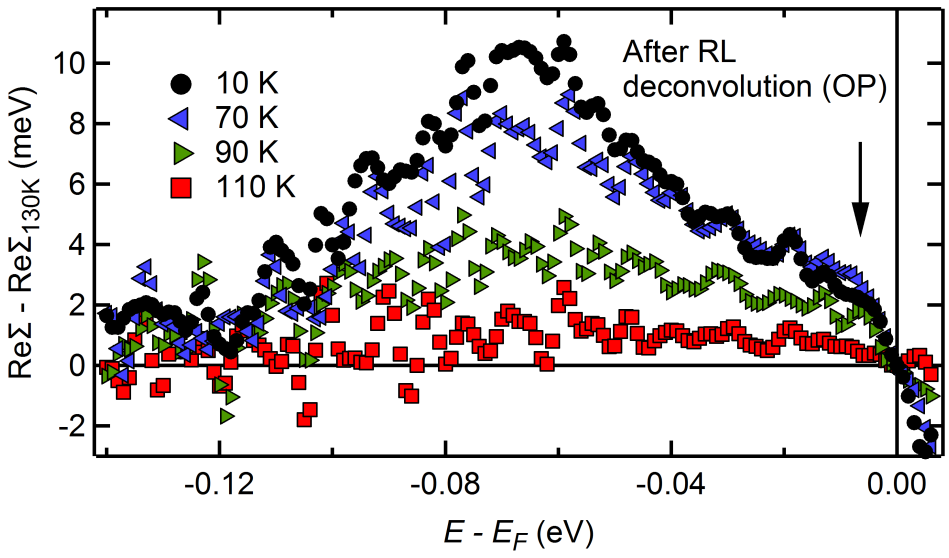

Figure 5.7: Temperature dependence of $\Sigma'(E)$ of the 10-meV kink. Effective $\Sigma'(E)$ spectra are extracted as in section 5.2.2 and plotted as the change in $\Sigma'(E)$ relative to 130 K. The feature due to the 10-meV kink is highlighted by the arrow. From [Plumb et al., 2010].

with the findings in Fig. 5.6 (see appendix B). Thus the results here appear to be highly robust.

5.3 Possible origins

Having established the existence of a nodal self-energy feature near the 10-meV scale, we are left to wonder about its physical origin. Given the success of the BCS theory of phonon-mediated conventional superconductivity, in the high-T_c cuprates there is a justifiable tendency to attempt to view any observed dispersion kink through the prism of electron-boson coupling. In the case of 10-meV kink, however, the low energy scale of the dispersion anomaly places strict constraints on any electron-boson interactions which might explain the kink. As discussed in Ch. 4, dispersion kinks observed by ARPES are shifted to deeper energy by the gap energy $\Delta(\boldsymbol{k'})$ at the location of the scattered state $\boldsymbol{k'}$. The d-wave gap, though zero-valued at the node, quickly rises to a maximum at the antinode. In optimally-doped Bi2212, the antinodal gap value ($\Delta_0 \approx 30$ meV) is clearly much larger than the observed kink. Thus, if bosons are at work, they are evidently scattering the nodal

electrons in very particular directions — namely, to other near-nodal points. Fig. 5.8 illustrates this point.

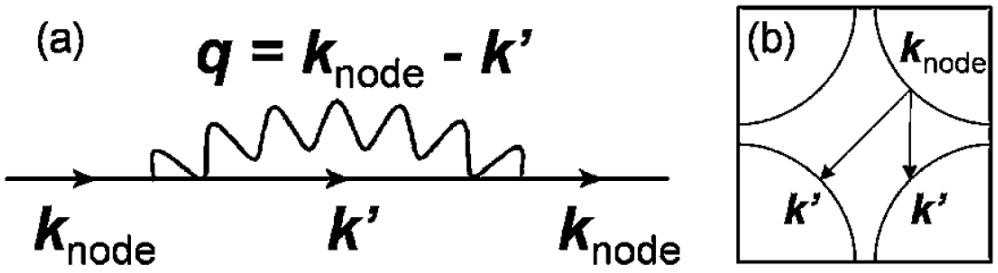

Figure 5.8: Examples of allowed electron-boson scattering vectors for the 10-meV kink. (a) Diagram of the lowest-order electron-boson interaction term in the Migdal approximation. In the context of the nodal states, an electron starting from $\boldsymbol{k}_{\text{node}}$ is scattered to $\boldsymbol{k'}$. The nodal dispersion kink observed by ARPES will appear at an energy scale equal to the boson mode energy plus the gap value $\Delta(\boldsymbol{k'})$. (b) Examples of allowed scattering vectors $\boldsymbol{q}$ for explaining the 10-meV kink. These vectors couple nodal regions of the gap function where $\Delta(\boldsymbol{k'}) \approx 0$. Another such vector is obviously $\boldsymbol{q} = 0$. From [Plumb et al., 2010].

Taking into account the energetic constraints, it has been argued that the kink results from the electrons coupling to acoustic phonons [Johnston et al., 2011] or c-axis optical phonons [Rameau et al., 2009, Anzai et al., 2010] with small momentum transfers $q \approx 0$. Additionally, an alternative theory related to 2D Fermi liquid behavior has been proposed to explain the temperature dependence of velocity of the band dispersion [Chubukov and Eremin, 2008], and it may also be relevant to the kink itself.

5.3.1 Acoustic phonon mode coupling

It has been suggested that the nodal 10-meV kink arises due to forward (i.e., $\boldsymbol{q} \approx 0$) scattering of the low-energy electrons by acoustic phonons [Johnston et al., 2011]. The model is described by

a standard Hamiltonian for the screened electron-phonon interaction:

$$H_{\text{el-ph}} = \frac{1}{\sqrt{N}} \sum_{\boldsymbol{q},\boldsymbol{k},\sigma,\nu} |g(\boldsymbol{k},\boldsymbol{q})|^2 d^\dagger_{\boldsymbol{k}-\boldsymbol{q},\sigma} d_{\boldsymbol{k},\sigma} (b^\dagger_{\boldsymbol{q},\nu} + b_{-\boldsymbol{q},\nu}) \tag{5.2}$$

where $d^\dagger_{\boldsymbol{k},\sigma}$ ($d_{\boldsymbol{k}}$) is the creation (annihilation) operator for an electron with momentum $\boldsymbol{k}$ and spin σ, and $b^\dagger_{\boldsymbol{q},\nu}$ ($b_{\boldsymbol{q},\nu}$) creates (annihilates) a phonon with momentum $\boldsymbol{q}$ on the branch indexed by ν. The quantity $g(\boldsymbol{k},\boldsymbol{q})$ is the matrix element for the coupling between an electron at $\boldsymbol{k}$ and a phonon with momentum $\boldsymbol{q}$. It is argued that for acoustic phonons, $g(\boldsymbol{k},\boldsymbol{q}) \to g(\boldsymbol{q})$ — i.e., the interaction is independent of the details of the electronic dispersion.

The terms $|g(\boldsymbol{q})|^2$ weight the contributions of the phonon Green's function to the self-energy [Mahan, 2000] and are given by

$$g(\boldsymbol{q}) = \frac{1}{V_{\text{cell}}} \sqrt{\frac{\hbar}{2M\Omega(\boldsymbol{q})}} \hat{e}_{\boldsymbol{q}} \cdot \boldsymbol{q} \frac{V(\boldsymbol{q})}{\varepsilon(\boldsymbol{q})} \tag{5.3}$$

where V_{cell} is the unit cell volume, M is the combined Cu-O ion mass, $\Omega(\boldsymbol{q})$ is the phonon dispersion, $\hat{e}_{\boldsymbol{q}}$ is the phonon polarization, and $V(\boldsymbol{q})$ is the Fourier-transformed Coulomb potential. The final term, $\varepsilon(\boldsymbol{q})$, is the dielectric function.

A Thomas-Fermi model of the dielectric function is thought to be relevant for the acoustic modes. This takes the form $\varepsilon(\boldsymbol{q}) = 1 + q^2_{TF}/q^2$, where q_{TF} parameterizes the damping of the dielectric response due to screening. In this model, $|g(\boldsymbol{q})|^2$ is peaked in the vicinity of $|\boldsymbol{q}| \sim q_{TF}$ and goes to zero at $\boldsymbol{q} = 0$. Johnston et al. argue that q_{TF} is small in cuprates. As a result, the coupling is peaked for small $\boldsymbol{q}$ momentum transfers.

In light of the screening effects, it is expected that q_{TF} should further decrease in the less-metallic underdoped regime. This, in turn, would intensify the peak in $|g(\boldsymbol{q})|^2$. Thus, the theory predicts that the kink should strengthen in the underdoped side of the phase diagram and weaken for overdoping. This prediction is consistent with the observations presented here. From Fig. 5.6 one can see that v_F is slightly higher in the overdoped state than at optimal doping, whereas v_{20} is essentially independent of the doping. Hence, judging the kink's strength by the ratio v_{20}/v_F, it is found to be slightly weaker in the case of overdoping. Furthermore, the 10-meV kink has been found to strengthen substantially with underdoping [Vishik et al., 2010, Anzai et al., 2010].

Calculations of the self-energy contributions due to acoustic mode coupling have been compared to data collected from underdoped Bi2212, which appear to agree well with the theoretical predictions. These results are shown in Fig. 5.9. Based on all available evidence, acoustic mode scattering currently seems to be a credible theory to explain the 10-meV kink. Still, other theories have not been as rigorously tested and cannot be conclusively ruled out.

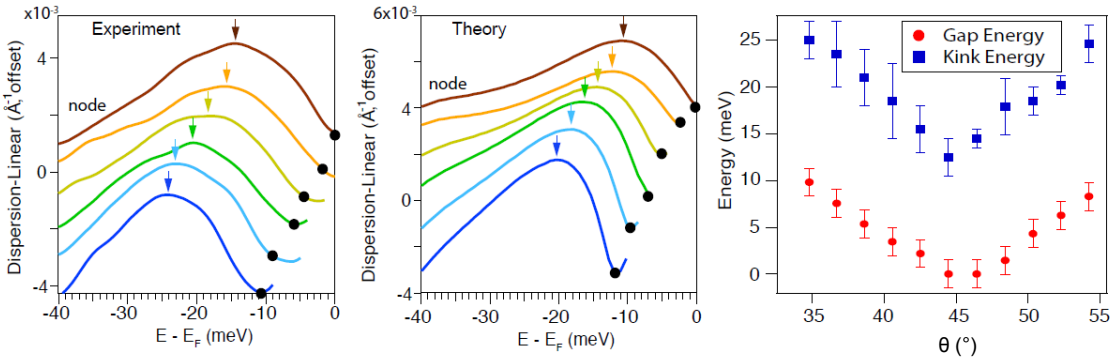

Figure 5.9: Evidence for acoustic phonon coupling as a possible origin of the 10-meV kink. Left: A measure of the effective $\Sigma'(E)$ obtained from ARPES on underdoped Bi2212 ($T_c = 55$ K). The self-energy extraction assumes a linear bare band connecting the dispersion at E_F and -40 meV. The data are obtained from ARPES cuts in small increments around the Fermi surface [$\approx 2°$ spacing in terms of the angle about (π, π), see bottom axis of right panel]. The extracted curves have not been multiplied by a band velocity and therefore are reported in units of Å^{-1}. A vertical offset is added for clarity. Middle: Comparison to calculated effective self-energies based on electron-phonon coupling due to acoustic modes. Right: Measured momentum dependence of the gap and low-energy kink location. The kink appears to be located at a constant offset of about 10 meV from the gap, which is consistent with the gap-referencing expected for acoustic phonons that scatter the electrons only locally in k-space. From [Johnston et al., 2011]. Reprinted with the authors' permission.

5.3.2 *c*-axis optical phonons

Prior to the theory of acoustic mode electron-phonon coupling, low-energy c-axis optical phonons were proposed as the cause of the 10-meV kink [Rameau et al., 2009]. Theory [Kovaleva

et al., 2004, Falter and Schnetgöke, 2003, Falter, 2005] and experiment [Liu et al., 1992, Tsvetkov et al., 1999, Misochko and Sherman, 2000] confirm the existence of optical phonons with suitably low energies in various cuprates, but again, it is critical that these electron-phonon interactions involve scattering $\boldsymbol{q}$ vectors connecting near-nodal points on the Fermi surface.

Presently there is serious disagreement regarding the nature of the scattering by these c-axis phonons. In particular, an A_{1g} mode (Fig. 5.10) has been proposed as the most likely candidate [Rameau et al., 2009] with some claiming that this mode should strongly favor the necessary $q \approx 0$ transfers [Rameau et al., 2009, Giustino et al., 2008] and others arguing that it should instead primarily scatter nodal electrons away from the node [Johnston et al., 2010, Johnston et al., 2011], which would violate the energetic constraints of the observed kink. So far no theoretical work has tried to simulate the ARPES dispersion kink based on a model of coupling to a c-axis optical mode. Such simulations could be an important topic for future investigation.

5.3.3 Backscattering in a 2D Fermi liquid

The Landau Fermi liquid theory is a generic picture of interacting electrons, neglecting correlation effects. Based on phase space arguments following from the Pauli exclusion principle, the allowed channels of electron-electron scattering grow with energy and temperature in such a way that Σ has the following dependence on E and T:

$$\Sigma_{\mathrm{FL}}(E) = \alpha E + i\beta[E^2 + (\pi k_B T)^2] \tag{5.4}$$

[Fetter and Walecka, 1971, Ashcroft and Mermin, 1976, Mahan, 2000]. The quadratic behavior of Σ''_{FL}, in particular, is one of the hallmarks of the Fermi liquid theory. However, a number of nonanalytic corrections to the theory exist, which lie outside the conventional phase space arguments [Chubukov and Maslov, 2003]. One such correction arises from singular $2k_F$ backscattering processes in 2D and exhibits low-energy behavior of logarithmic form $\Sigma''(E) \sim E^2 \ln E$. This is a generic feature of a 2D Fermi liquid, though the size of the correction will depend on the details of the system in question. Chubukov and Eremin have analyzed the numerics of this correction in

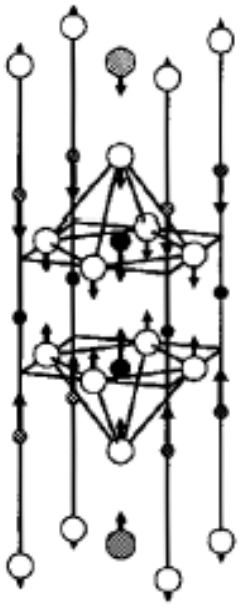

Figure 5.10: Low-energy A_{1g} mode in Bi2212. This mode has been proposed as the origin of the 10-meV kink seen in ARPES. Rameau et al. [Rameau et al., 2009] state the observed energy of this mode as 58–65 cm^{-1} (= 7.2–8.1 meV). Falter and Schnetgöke [Falter and Schnetgöke, 2003], from whom the figure is adapted, calculate it to be 2.944 THz (= 12.18 meV). Reprinted with permission. Copyright 2003 by IOP Publishing, Ltd.

cuprates and have found that it may account for the linear temperature dependence of the low-energy band velocity (which we may regard as v_{20}) [Chubukov and Eremin, 2008]. Additionally, some T-dependent bending behavior can be seen in the calculated $\Sigma'(E)$ which could presumably be related to the kink itself, although this is not made explicit in their work.

While the explanation of the linearity of $v_{20}(T)$ — and possibly the more dramatic T dependence of the 10-meV kink — in terms of this 2D Fermi liquid correction exhibits some qualitative consistency with the data, it must be noted that there is a substantial and ongoing debate as to whether cuprate physics can even be described by the Fermi liquid model. Above T_c, in the pseudogap regime, cuprates exhibit transport properties, for example, that are anomalous and in conflict with Fermi liquid theory [Iye, 1992] (although the transport regains Fermi-liquid-like characteristics

— e.g., $\rho \sim T^2$ — when the sample is strongly overdoped). It has been proposed, in fact, that the cuprates are better described by a "marginal" Fermi liquid (MFL) model [Varma et al., 1989] with a self-energy characterized by

$$\Sigma''_{\mathrm{MFL}}(E) \propto \max(|E|, k_B T) \tag{5.5}$$

There is evidence from optical conductivity that the momentum-integrated $\Sigma''(E,T)$ follows the linear MFL behavior [Hwang et al., 2004], but ARPES has not arrived at a consensus on this issue [Valla et al., 2000, Koitzsch et al., 2004a, Koralek et al., 2006, Casey et al., 2008]. If it is true that the Fermi liquid model is insufficient as a description of the basic electron-electron interactions in cuprates, then presumably this could undermine the argument that the 10-meV kink originates from a $2k_F$ interaction in the 2D Fermi liquid.

5.3.4 Ruled out

A few mechanisms can be ruled out as the cause of the nodal 10-meV kink:

- *Reduced phase space for electron-electron scattering in the superconducting state.* As the sample temperature is lowered into the superconducting state, the opening of the d-wave gap will eliminate the allowed phase space for electron-electron scattering within the d-wave gap energy scale $\Delta(\boldsymbol{k})$. At first glance, it would seem that this could largely explain the observed kink: The sudden reduction in scattering at an energy scale on the order of $\Delta_0 \sim 30$ meV could lead to a sharp drop in $\Sigma''(E)$ and a corresponding feature $\Sigma'(E)$, which, averaging over the Fermi surface, might actually be located somewhere near 10 meV. This turns out to be an oversimplified picture. The lowest-order electron-electron term is the process depicted by the Feynman diagram in Fig. 5.11 [Norman and Ding, 1998]. The diagram shows that the electron-electron scattering event leads to the creation (and recombination) of a polarized electron-hole pair. In the superconducting state, each of the three internal particle lines — the scattered electron plus the electron-hole pair — acquires a $\Delta(\boldsymbol{k'})$ due to the local value of the gap at each scattered momentum state. As a result,

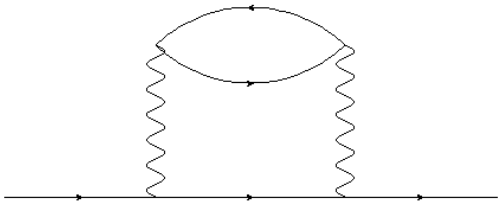

Figure 5.11: Lowest-order Feynman diagram for electron-electron scattering. One electron scatters off another, creating an electron-hole polarization "bubble", which then recombines. In the d-wave superconducting state, each of the three internal particle lines is gapped by the value of Δ appropriate for each scattered momentum state.

assuming that the scattering is basically isotropic, any drop in $\Sigma''(E)$ should be spread over a broad energy range up to $3\Delta_0$ (≈ 90 meV) [Littlewood and Varma, 1992, Norman and Ding, 1998]. Clearly this energy scale is incompatible with the relatively sharp, low energy scale of the 10-meV kink. Thus, it is virtually impossible for the kink to result from a suppression of low-energy electron-electron scattering due to the opening of the d-wave superconducting gap.

- *Almost all electron-boson interactions with in-plane momentum transfers.* As already discussed, electron-boson interactions lead to kinks in ARPES at energies that are gap-shifted according to $\Omega_{\mathrm{kink}} = -\Omega_{\mathrm{boson}} - \Delta(\boldsymbol{k'})$. Since the observed kink at the node is already at a lower energy scale than the gap maximum, this demands at least that $\Delta(\boldsymbol{k'}) < 10$ meV, if not $\Delta(\boldsymbol{k'}) \approx 0$. In the d-wave superconductor, only a small subset of scattering vectors $\boldsymbol{q} = \boldsymbol{k'} - \boldsymbol{k}$ satisfy this requirement (Fig. 5.8). Thus a large class of in-plane momentum transfers can be ruled out.

- *Marginal Fermi liquid behavior.* As touched upon in section 5.3.3, over much of the doping phase diagram, cuprates do not behave as expected from Fermi liquid theory, which is the generic model of electron-electron interactions in a standard, uncorrelated metal. As

an alternative, so-called marginal Fermi liquid theory has been proposed to describe the electronic self-energy in cuprates [Varma et al., 1989]. In this theory, the $\Sigma''(E)$ linearly approaches E_F, until suddenly flattening out at $|E| < k_BT$ (Eq. 5.5). The sharp crossover behavior should presumably lead to some kind of low-energy feature in $\Sigma'(E)$ via the Kramers-Kronig relation.[6] However, the theory implies that the location of this kink or bend should be temperature-dependent. Contrary to this, our data show no clear evidence of any such temperature shift (see Fig. 5.7). Therefore, barring any future refinements to the data that might reveal some small temperature dependence of the kink's location, marginal Fermi liquid behavior can be ruled out as a possible cause of the 10-meV kink.

5.4 Breaking the universal Fermi velocity

Zhou et al. studied several cuprate systems and noted that, over a large doping range, the nodal dispersion between the 70-meV kink and E_F tends to converge toward a common slope [Zhou et al., 2003]. They called this slope "v_F", although it was determined by fitting over the range from -50 meV to E_F. Hence it is more comparable to our v_{20}. The results from Zhou et al. are shown in Fig. 5.12. The low-energy band velocities fall within about 20% of each other, while those of the deeper dispersions well below the 70-meV kink vary by a factor of about 2–3. Supposing (incorrectly, it turns out) that this "universal" nodal Fermi velocity is a robust feature of the dispersion, the mechanism underlying this phenomenon is not clear, but philosophically-inclined physicists might be tempted to invoke the notion of a "quantum protectorate" — a state of matter "whose generic low-energy properties are determined by a higher organizing principle and nothing else" [Laughlin and Pines, 2000]. Presumably, if we were witnessing some signpost of quantum protection, then the Fermi velocity should exhibit universality not only against variations in material and doping, but also temperature.

[6] Technically speaking, Varma et al. have written the real part of the marginal Fermi liquid self-energy as $\Sigma'_{\mathrm{MFL}}(E) = E\ln[\max(|E|, k_BT)/E_c]$, where E_c is an ultraviolet cutoff [Varma et al., 1989]. However, the theory seems more firmly rooted in $\Sigma''_{\mathrm{MFL}}(E)$ as a starting point than $\Sigma'_{\mathrm{MFL}}(E)$, so we have quoted just the imaginary part in the main text. In any event, the theory undoubtedly features a crossover behavior in $\Sigma'(E)$ related to T, so this technical point does not affect the conclusions here.

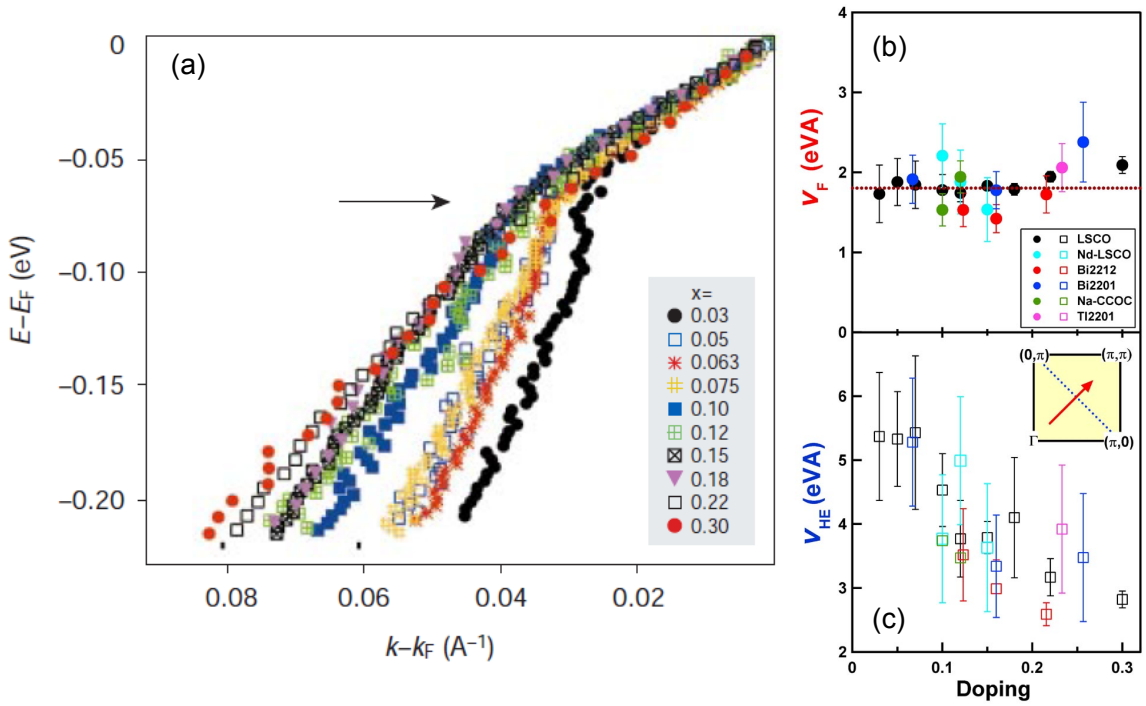

Figure 5.12: Earlier claim of a universal nodal Fermi velocity. Between E_F and the kink at about 70 meV, the band velocity is roughly independent of doping. This supposed universality is broken by the doping and temperature dependence of v_F due to the 10-meV kink (Fig. 5.6). In the panels at right, values of "v_F" are determined by linear fits from -50 meV to E_F. "v_{HE}" are obtained by fitting from -200 to -100 meV. From [Zhou et al., 2003] and supplementary material therein. Reprinted by permission from Macmillan Publishers Ltd., copyright 2003.

The behavior of the 10-meV kink, however, breaks the paradigm of the universal Fermi velocity. Figure 5.6 clearly illustrates that v_F depends on both temperature and doping. The behavior of v_{20}, on the other hand, helps explain the earlier observation of the supposed universality: Although v_{20} varies approximately linearly with T, it appears to be largely independent of doping. This is consistent with previous work (which was fixed at $T = 20$ K) to the extent that those experiments lacked the resolution to distinguish v_F and v_{20}. Notably, although the temperature dependence of v_F depends on doping, our results show that the behavior of v_{20} does not. Thus there is, in some sense, a doping-independent universality of the dispersion intermediate to the 10-meV

kink and the one at 70 meV. However, the relevance of framing the discussion of the low-lying electronic features in terms of universal behavior has been seriously called into question by the results shown here.

5.5 Recent developments and future directions of study

The results presented in this chapter have established the existence of a kink roughly 10 meV below E_F along the gap node of Bi2212. Furthermore the kink first appears below a temperature close to T_c, and it seems that its strength depends on doping. Namely, we find that the kink strengthens going from overdoping to optimal doping. These results are largely consistent with those of three other groups who have independently confirmed the existence of this dispersion feature [Rameau et al., 2009, Vishik et al., 2010, Anzai et al., 2010, Johnston et al., 2011]. Despite so many concurrent or nearly-concurrent studies, each has managed to take a somewhat unique tack (though all have relied on LE-ARPES), and as a result, a significant amount of the experimental parameter space concerning the kink has rapidly been explored: temperature [Plumb et al., 2010], doping [Plumb et al., 2010, Vishik et al., 2010, Anzai et al., 2010], and momentum dependence [Rameau et al., 2009, Johnston et al., 2011]. Though obtained and analyzed in various ways, the results are largely consistent with each other. For the most part the experiments seem to be rapidly converging toward a unified picture of the existence and behavior of the 10-meV kink (though there is decidedly less convergence on the theoretical side). In addition to our findings, it appears that the feature persists over the region around the node where it shifts to deeper binding energy according to the local gap value $\Delta(\boldsymbol{k})$ [Rameau et al., 2009, Johnston et al., 2011]. Also, it seems that the kink strengthens substantially in the underdoped region of the phase diagram [Vishik et al., 2010, Anzai et al., 2010].

One of the only points of conflict so far is whether the kink weakens or intensifies in the case of overdoping. Anzai et al. report that the kink is weakest at optimal doping, and in their data it appears to strengthen again as the sample is overdoped. Clearly this is in conflict with our own observations. One obvious point for future study, then, is to further investigate the behavior of the

kink on the overdoped side of the phase diagram in order to pin down its behavior. The results of such a study could prove to be very useful. For instance, if it were discovered that the kink is in fact weakest at optimal doping, then this might signal that the interactions oppose superconductivity and break d-wave Cooper pairs.

Expanded studies of the momentum-dependence of the 10-meV kink will also be of great importance. In particular, it would be interesting to know how the kink evolves going from the near-nodal region to the antinode. It could turn out that this nodal kink is related to a well-known antinodal dispersion kink at about 40 meV (which is roughly what one expects based on gap-referencing and an antinodal gap $\Delta_0 \approx 30$ meV). If it were discovered that these two dispersion features are connected, this could throw a wrench into current theories of the antinodal kink, which is typically thought to arise from either entirely different phonon interactions [Devereaux et al., 2004] or from coupling to spin fluctuations [Manske et al., 2001].

Experiments are also needed to test for the presence of the 10-meV kink in other cuprates besides Bi2212. Like the 70-meV kink [Lanzara et al., 2001], if it is found to be an ubiquitous, universal feature of the nodal dispersion in cuprates, then this would provide one more indication of the 10-meV kink's possible relevance for high-T_c superconductivity. A good starting point in testing the ubiquity of the low-energy kink may be $La_{2-x}Sr_xCuO_4$ (LSCO), since one ARPES group has claimed to see a low-energy kink in this material at momentum intermediate to the node and antinode [Sato et al., 2007, Xiao et al., 2007]. Those studies, however, did not use ultrahigh resolution and/or low-energy photons, and the quality of the data merits some skepticism in light of the resolution effects discussed here (section 5.2.3). Thus, the possibility of a low-energy dispersion kink in LSCO should be revisited using LE-ARPES, and other cuprate systems should be investigated as well.

Concerning the debate over the origin of the kink, simulations of ARPES spectra akin to what was done in [Johnston et al., 2011] but instead using a model of the c-axis optical phonon coupling would be very valuable. Additionally, it may be productive to investigate whether the 2D Fermi liquid backscattering theory of section 5.3.3 can be more quantitatively connected to the

10-meV kink and its behavior.

The behavior of the kink and the strong temperature and doping dependence it induces in the Fermi velocity suggest that it may be possible to gain new insights into the transport properties of cuprates, since v_F is a key parameter of the Boltzmann transport equation. For instance, Vishik et al. [Vishik et al., 2010] showed that previous discrepancies between thermal conductivity experiments and the expected transport properties based on ARPES measurements [Sun et al., 2006] may now be resolved in light of the breakdown of the supposed universal nodal Fermi velocity (section 5.4). Beyond this, it is quite possible that the details of the temperature and doping dependence of v_F above T_c may eventually give new insights into the "strange metal" behavior in and around the pseudogap regime, so experiments in this part of the phase diagram may be quite valuable.

Clearly, despite so much early progress in studying the 10-meV kink, more work remains to be done. LE-ARPES will be crucial in these future experiments, as the advantages unique to low-energy photons are necessary to reveal the fine details of the dispersion near E_F.

Chapter 6

Summary and discussion

This thesis presented new findings from studies of the high-T_c cuprate superconductor Bi2212 using low photon energy ARPES. In particular, the work focused on the detailed analysis of "kink" dispersion anomalies in the k-space region around the node of the superconducting gap. These kinks are of great interest, because they signal the energy- and momentum-dependent characteristics of strong, sharp many-body interactions experienced by the electrons. In principle, then, such dispersion features may be gateways to valuable information about the interactions behind high-temperature superconductivity.

In chapter 4, LE-ARPES was able to reveal the detailed momentum evolution of a well-known, prominent feature of the electronic dispersion. At optimal doping and below T_c, a large kink normally found at about 65 meV shifts smoothly toward E_F by about 10 meV. This happens somewhat quickly over a k-space distance corresponding to about one-third of the way from node to antinode. Extracted self-energy components Σ'_{eff} and Σ''_{eff} tell the same story: Over most of the near-nodal range, the width and intensity of the kink does not change much, even as its location is smoothly varying. However, for $\theta \gtrsim 10^\circ$ [where θ is the angle from the node, measured about (π, π)], $\Sigma''_{\text{eff}}(\omega)$ sharpens and $\Sigma'_{\text{eff}}(\omega)$ correspondingly sharpens and intensifies. These new observations represent the clearest, most detailed study yet of the nature of the transition of the main kink's self-energy from node to antinode, answering some lingering questions about "crossover" behavior between these two regions.

Motivated by several factors, we attempted to calculate the momentum-dependent energy

of a supposed bosonic coupling mode based on a model of various assumed, simple scattering $\boldsymbol{q}$ vectors of the interactions. Plotting the results as function of $\boldsymbol{q}$ along different symmetries of the Brillouin zone, we found that the ARPES-extracted boson dispersion was in rough agreement with a Cu-O bond-stretching phonon over a short range of q-space. Otherwise, however, the extracted dispersion was in conflict with measured values for phonons. Instead, the dispersion was more similar in character to that of high-energy incommensurate spin excitations. Moreover, the intensification and sharpening seen in $\Sigma'_{\text{eff}}(\omega)$ and $\Sigma''_{\text{eff}}(\omega)$, respectively, as a function of the boson energy and the location on the Fermi surface are in qualitative agreement with the expectations for the electrons being coupled to spin excitations. By contrast, the phonon most widely suspected to be responsible for the main nodal kink is expected to have substantially different behavior as a function of momentum around the Fermi surface.

In these respects, overall the results of Ch. 4 seem to point to incommensurate spin fluctuations as the cause of the well-known nodal "70-meV" kink. This finding agrees with certain ARPES studies that arrived at similar conclusions by different methods, but it nevertheless comes as a surprise in light of other studies that have carefully presented significant evidence that the kink is instead due to phonons. It seems quite possible then that both classes of interaction make a measurable contribution to the nodal kink. The question then becomes, Does one type of interaction dominate, or are they both critical to the physics of the nodal electrons? We clearly cannot answer this question now, but hopefully future investigations using LE-ARPES in combination with more theory work will resolve the conflict.

Chapter 5 presented an analysis of a new, fine-scale, near-E_F kink in the nodal dispersion. Whereas complications due to resolution effects rendered this feature virtually invisible to previous ARPES experiments, the use of low-energy photons allowed accurate measurements of the band dispersion down to temperatures low enough that the kink was visible in the raw data. Just 10-meV or so below the Fermi level, LE-ARPES found that the kink turns on near T_c in both optimal and overdoped samples. This dispersion anomaly, though small, has a profound effect on the nodal Fermi velocity, and as a result, it disobeys a previous notion that v_F was supposedly a constant

with respect to doping.

The extremely low energy of this kink puts useful constraints on the types of phenomena from which it might originate. Namely, it is argued that the responsible coupling must somehow scatter electrons between near-nodal points on the Fermi surface. A leading theory proposed so far for the origin of the kink is forward-scattering ($\boldsymbol{q} \approx 0$) interactions with acoustic phonons, though other theories have been proposed. The discovery of the 10-meV kink has drawn the attention of a handful of groups who are all necessarily and exclusively using LE-ARPES to study it. As a result, we are rapidly learning much about its behavior. The progress so far suggests some promising experiments for the future: e.g., probing the k-dependence of the feature to momenta close to the antinode, testing for the 10-meV kink in other cuprates besides Bi2212, and verifying the behavior of the kink's strength in the overdoped regime.

Beyond the results of the studies in chapters 4 and 5, there is one overarching and clear finding. LE-ARPES extends the power of more conventional ARPES by substantial improvements in resolution, material bulk sensitivity, and overall spectral sharpness. These advantages have already uncovered significant new physics in cuprates, with the promise of more to come in these materials and others.

Bibliography

[Adachi et al., 2001] Adachi, T., Noji, T., and Koike, Y. (2001). Crystal growth, transport properties, and crystal structure of the single-crystal $La_{2-x}Ba_xCuO_4$ ($x = 0.11$). Physical Review B: Solid State, 64(14):144524.

[Aebi et al., 1994] Aebi, P., Osterwalder, J., Schwaller, P., Schlapbach, L., Shimoda, M., Mochiku, T., and Kadowaki, K. (1994). Complete Fermi surface mapping of $Bi_2Sr_2CaCu_2O_{8+x}$(001): Coexistence of short range antiferromagnetic correlations and metallicity in the same phase. Physical Review Letters, 72(17):2757–2760.

[Allen, 1971] Allen, P. B. (1971). Electron-phonon effects in the infrared properties of metals. Physical Review B: Solid State, 3(2):305–320.

[Ando et al., 2002] Ando, Y., Segawa, K., Komiya, S., and Lavrov, A. N. (2002). Electrical resistivity anisotropy from self-organized one dimensionality in high-temperature superconductors. Physical Review Letters, 88(13):137005.

[Anzai et al., 2010] Anzai, H., Ino, A., Kamo, T., Fujita, T., Arita, M., Namatame, H., Taniguchi, M., Fujimori, A., Shen, Z.-X., Ishikado, M., and Uchida, S. (2010). Energy-dependent enhancement of the electron-coupling spectrum of the underdoped $Bi_2Sr_2CaCu_2O_{8+\delta}$ superconductor. Physical Review Letters, 105(22):227002.

[Ashcroft and Mermin, 1976] Ashcroft, N. W. and Mermin, N. D. (1976). Solid State Physics. Saunders College, Philadelphia, 1st edition.

[Balatsky et al., 2009] Balatsky, A. V., Lee, W. S., and Shen, Z. X. (2009). Bogoliubov angle, particle-hole mixture, and angle-resolved photoemission spectroscopy in superconductors. Physical Review B: Solid State, 79(2):020505.

[Bardeen et al., 1957] Bardeen, J., Cooper, L. N., and Schrieffer, J. R. (1957). Theory of superconductivity. Physical Review, 108(5):1175–1204.

[Basak et al., 2009] Basak, S., Das, T., Lin, H., Nieminen, J., Lindroos, M., Markiewicz, R. S., and Bansil, A. (2009). Origin of the high-energy kink in the photoemission spectrum of the high-temperature superconductor $Bi_2Sr_2CaCu_2O_8$. Physical Review B: Solid State, 80(21):214520.

[Bednorz and Müller, 1986] Bednorz, J. G. and Müller, K. A. (1986). Possible high T_c superconductivity in the BaLaCuO system. Zeitschrift für Physik B: Condensed Matter, 64(2):189–193.

[Bednorz and Müller, 1988] Bednorz, J. G. and Müller, K. A. (1988). Perovskite-type oxides—The new approach to high-T_c superconductivity. Review of Modern Physics, 60(3):585–600.

[Bogdanov et al., 2000] Bogdanov, P. V., Lanzara, A., Kellar, S. A., Zhou, X. J., Lu, E. D., Zheng, W. J., Gu, G., Shimoyama, J.-I., Kishio, K., Ikeda, H., Yoshizaki, R., Hussain, Z., and Shen, Z. X. (2000). Evidence for an energy scale for quasiparticle dispersion in $Bi_2Sr_2CaCu_2O_8$. Physical Review Letters, 85(12):2581–2584.

[Bogdanov et al., 2002] Bogdanov, P. V., Lanzara, A., Zhou, X. J., Yang, W. L., Eisaki, H., Hussain, Z., and Shen, Z. X. (2002). Anomalous momentum dependence of the quasiparticle scattering rate in overdoped $Bi_2Sr_2CaCu_2O_8$. Physical Review Letters, 89(16):167002.

[Bok et al., 2010] Bok, J. M., Yun, J. H., Choi, H.-Y., Zhang, W., Zhou, X. J., and Varma, C. M. (2010). Momentum dependence of the single-particle self-energy and fluctuation spectrum of slightly underdoped $Bi_2Sr_2CaCu_2O_{8+\delta}$ from high-resolution laser angle-resolved photoemission. Physical Review B: Solid State, 81(17):174516.

[Borisenko et al., 2000] Borisenko, S. V., Golden, M. S., Legner, S., Pichler, T., Dürr, C., Knupfer, M., Fink, J., Yang, G., Abell, S., and Berger, H. (2000). Joys and pitfalls of Fermi surface mapping in $Bi_2Sr_2CaCu_2O_{8+\delta}$ using angle resolved photoemission. Physical Review Letters, 84(19):4453–4456.

[Borisenko et al., 2006] Borisenko, S. V., Kordyuk, A. A., Zabolotnyy, V., Geck, J., Inosov, D., Koitzsch, A., Fink, J., Knupfer, M., Büchner, B., Hinkov, V., Lin, C. T., Keimer, B., Wolf, T., Chiuzbăian, S. G., Patthey, L., and Follath, R. (2006). Kinks, nodal bilayer splitting, and interband scattering in $YBa_2Cu_3O_{6+x}$. Physical Review Letters, 96(11):117004.

[Boyer et al., 2007] Boyer, M. C., Wise, W. D., Chatterjee, K., Yi, M., Kondo, T., Takeuchi, T., Ikuta, H., and Hudson, E. W. (2007). Imaging the two gaps of the high-temperature superconductor $Bi_2Sr_2CuO_{6+x}$. Nature Physics, 3(11):802–806.

[Broun, 2008] Broun, D. M. (2008). What lies beneath the dome? Nature Physics, 4(3):170–172.

[Bulut and Scalapino, 1996] Bulut, N. and Scalapino, D. J. (1996). $d_{x^2-y^2}$ symmetry and the pairing mechanism. Physical Review B: Solid State, 54(21):14971–14973.

[Byczuk et al., 2007] Byczuk, K., Kollar, M., Held, K., Yang, Y.-F., Nekrasov, I. A., Pruschke, T., and Vollhardt, D. (2007). Kinks in the dispersion of strongly correlated electrons. Nature Physics, 3(3):168–171.

[Casey et al., 2008] Casey, P. A., Koralek, J. D., Plumb, N. C., Dessau, D. S., and Anderson, P. W. (2008). Accurate theoretical fits to laser-excited photoemission spectra in the normal phase of high-temperature superconductors. Nature Physics, 4:210–212.

[Chainani et al., 2000] Chainani, A., Yokoya, T., Kiss, T., and Shin, S. (2000). Photoemission spectroscopy of the strong-coupling superconducting transitions in lead and niobium. Physical Review Letters, 85(9):1966–1969.

[Chang et al., 2008] Chang, J., Sassa, Y., Guerrero, S., Månsson, M., Shi, M., Pailhès, S., Bendounan, A., Mottl, R., Claesson, T., Tjernberg, O., Patthey, L., Ido, M., Oda, M., Momono, N., Mudry, C., and Mesot, J. (2008). Electronic structure near the 1/8-anomaly in La-based cuprates. New Journal of Physics, 10(10):103016.

[Chuang et al., 2001] Chuang, Y.-D., Gromko, A. D., Fedorov, A., Aiura, Y., Oka, K., Ando, Y., Eisaki, H., Uchida, S. I., and Dessau, D. S. (2001). Doubling of the bands in overdoped $Bi_2Sr_2CaCu_2O_{8+\delta}$: Evidence for c-axis bilayer coupling. Physical Review Letters, 87(11):117002.

[Chubukov and Eremin, 2008] Chubukov, A. and Eremin, I. (2008). Strong-coupling theory of the universal linear temperature dependence of the nodal Fermi velocity in layered cuprates. Physical Review B: Solid State, 78(6):060509(R).

[Chubukov, 1995] Chubukov, A. V. (1995). Quasiparticle spectrum in a nearly antiferromagnetic Fermi liquid: Shadow and flat bands. Physical Review B: Solid State, 52(6):R3840–R3843.

[Chubukov and Maslov, 2003] Chubukov, A. V. and Maslov, D. L. (2003). Nonanalytic corrections to the Fermi liquid behavior. Physical Review B: Solid State, 68:155113.

[Chubukov and Norman, 2004] Chubukov, A. V. and Norman, M. R. (2004). Dispersion anomalies in cuprate superconductors. Physical Review B: Solid State, 70(17):174505.

[Cuk et al., 2004] Cuk, T., Baumberger, F., Lu, D. H., Ingle, N., Zhou, X. J., Eisaki, H., Kaneko, N., Hussain, Z., Devereaux, T. P., Nagaosa, N., and Shen, Z.-X. (2004). Coupling of the B_{1g} phonon to the antinodal electronic states of $Bi_2Sr_2Ca_{0.92}Y_{0.08}Cu_2O_{8+\delta}$. Physical Review Letters, 93(11):117003.

[Dahm et al., 2009] Dahm, T., Hinkov, V., Borisenko, S. V., Kordyuk, A. A., Zabolotnyy, V. B., Fink, J., Buchner, B., Scalapino, D. J., Hanke, W., and Keimer, B. (2009). Strength of the spin-fluctuation-mediated pairing interaction in a high-temperature superconductor. Nature Physics, 5(3):217–221.

[Damascelli, 2004] Damascelli, A. (2004). Probing the electronic structure of complex systems by ARPES. Physica Scripta, 2004(T109):61–74.

[Damascelli et al., 2003] Damascelli, A., Hussain, Z., and Shen, Z.-X. (2003). Angle-resolved photoemission studies of the cuprate superconductors. Review of Modern Physics, 75(2):473–541.

[Devereaux et al., 2004] Devereaux, T. P., Cuk, T., Shen, Z.-X., and Nagaosa, N. (2004). Anisotropic electron-phonon interaction in the cuprates. Physical Review Letters, 93(11):117004.

[Ding et al., 1996a] Ding, H., Norman, M. R., Campuzano, J. C., Randeria, M., Bellman, A. F., Yokoya, T., Takahashi, T., Mochiku, T., and Kadowaki, K. (1996a). Angle-resolved photoemission spectroscopy study of the superconducting gap anisotropy in $Bi_2Sr_2CaCu_2O_{8+x}$. Physical Review B: Solid State, 54(14):R9678–R9681.

[Ding et al., 1996b] Ding, H., Yokoya, T., Campuzano, J. C., Takahashi, T., Randeria, M., Norman, M. R., Mochiku, T., Kadowaki, K., and Giapintzakis, J. (1996b). Spectroscopic evidence for a pseudogap in the normal state of underdoped high-T_c superconductors. Nature, 382(6586):51–54.

[Doiron-Leyraud et al., 2007] Doiron-Leyraud, N., Proust, C., LeBoeuf, D., Levallois, J., Bonnemaison, J.-B., Liang, R., Bonn, D. A., Hardy, W. N., and Taillefer, L. (2007). Quantum oscillations and the Fermi surface in an underdoped high-T_c superconductor. Nature, 447(7144):565–568.

[Falter, 2005] Falter, C. (2005). Phonons, electronic charge response and electron-phonon interaction in the high-temperature superconductors. Physica Status Solidi B: Basic Research, 242(1):78–117.

[Falter and Schnetgöke, 2003] Falter, C. and Schnetgöke, F. (2003). Infrared- and Raman-active modes of Bi-based cuprate superconductors calculated in a microscopic model. Journal of Physics: Condensed Matter, 15(49):8495.

[Fedorov et al., 1999] Fedorov, A. V., Valla, T., Johnson, P. D., Li, Q., Gu, G. D., and Koshizuka, N. (1999). Temperature dependent photoemission studies of optimally doped $Bi_2Sr_2CaCu_2O_8$. Physical Review Letters, 82(10):2179–2182.

[Feng et al., 2001] Feng, D. L., Armitage, N. P., Lu, D. H., Damascelli, A., Hu, J. P., Bogdanov, P., Lanzara, A., Ronning, F., Shen, K. M., Eisaki, H., Kim, C., Shen, Z.-X., Shimoyama, J.-i., and Kishio, K. (2001). Bilayer splitting in the electronic structure of heavily overdoped $Bi_2Sr_2CaCu_2O_{8+\delta}$. Physical Review Letters, 86(24):5550–5553.

[Fetter and Walecka, 1971] Fetter, A. L. and Walecka, J. D. (1971). Quantum Theory of Many-Particle Systems. McGraw-Hill, San Francisco.

[Feuerbacher and Fitton, 1972] Feuerbacher, B. and Fitton, B. (1972). Photoemission from surface states on tungsten. Physical Review Letters, 29(12):786–789.

[Fong et al., 1999] Fong, H. F., Bourges, P., Sidis, Y., Regnault, L. P., Ivanov, A., Gu, G. D., Koshizuka, N., and Keimer, B. (1999). Neutron scattering from magnetic excitations in $Bi_2Sr_2CaCu_2O_{8+\delta}$. Nature, 398(6728):588–591.

[Garcia et al., 2010] Garcia, D. R., Graf, J., Jozwiak, C., Hwang, C. G., Eisaki, H., and Lanzara, A. (2010). Crossover region between nodal and antinodal states at the Fermi level of optimally doped and overdoped $Bi_2Sr_{1.6}Nd_{0.4}CuO_{6+\delta}$. Physical Review B: Solid State, 81(18):184527.

[Giustino et al., 2008] Giustino, F., Cohen, M. L., and Louie, S. G. (2008). Small phonon contribution to the photoemission kink in the copper oxide superconductors. Nature, 452:975–978.

[Graf et al., 2008] Graf, J., d'Astuto, M., Jozwiak, C., Garcia, D. R., Saini, N. L., Krisch, M., Ikeuchi, K., Baron, A. Q. R., Eisaki, H., and Lanzara, A. (2008). Bond stretching phonon softening and kinks in the angle-resolved photoemission spectra of optimally doped $Bi_2Sr_{1.6}La_{0.4}Cu_2O_{6+\delta}$ superconductors. Physical Review Letters, 100(22):227002.

[Graf et al., 2007] Graf, J., Gweon, G.-H., McElroy, K., Zhou, S. Y., Jozwiak, C., Rotenberg, E., Bill, A., Sasagawa, T., Eisaki, H., Uchida, S., Takagi, H., Lee, D.-H., and Lanzara, A. (2007). Universal high energy anomaly in the angle-resolved photoemission spectra of high temperature superconductors: Possible evidence of spinon and holon branches. Physical Review Letters, 98(6):067004.

[Gromko, 2001] Gromko, A. D. (2001). The Electronic Structure of High Temperature Superconductors Revealed: the Fermi Surface and Magnetically Mediated Pairing. PhD thesis, University of Colorado at Boulder.

[Gromko et al., 2003] Gromko, A. D., Fedorov, A. V., Chuang, Y.-D., Koralek, J. D., Aiura, Y., Yamaguchi, Y., Oka, K., Ando, Y., and Dessau, D. S. (2003). Mass-renormalized electronic

excitations at $(\pi, 0)$ in the superconducting state of $Bi_2Sr_2CaCu_2O_{8+\delta}$. Physical Review B: Solid State, 68(17):174520.

[Hansen et al., 1998] Hansen, E. D., Miller, T., and Chiang, T.-C. (1998). Observation of photoemission line widths narrower than the inverse lifetime. Physical Review Letters, 80(8):1766–1769.

[Hashimoto et al., 2010] Hashimoto, M., He, R.-H., Tanaka, K., Testaud, J.-P., Meevasana, W., Moore, R. G., Lu, D., Yao, H., Yoshida, Y., Eisaki, H., Devereaux, T. P., Hussain, Z., and Shen, Z.-X. (2010). Particle-hole symmetry breaking in the pseudogap state of Bi2201. Nature Physics, 6(6):414–418.

[Hayden et al., 2004] Hayden, S. M., Mook, H. A., Dai, P., Perring, T. G., and Dogan, F. (2004). The structure of the high-energy spin excitations in a high-transition-temperature superconductor. Nature, 429(6991):531–534.

[Hinkov et al., 2007] Hinkov, V., Bourges, P., Pailhes, S., Sidis, Y., Ivanov, A., Frost, C. D., Perring, T. G., Lin, C. T., Chen, D. P., and Keimer, B. (2007). Spin dynamics in the pseudogap state of a high-temperature superconductor. Nature Physics, 3(11):780–785.

[Hüfner, 2003] Hüfner, S. (2003). Photoelectron Spectroscopy: Principles And Applications. Springer, Berlin, 3rd edition.

[Hüfner et al., 1999] Hüfner, S., Claessen, R., Reinert, F., Straub, T., Strocov, V. N., and Steiner, P. (1999). Photoemission spectroscopy in metals: band structure — Fermi surface — spectral function. Journal of Electron Spectroscopy and Related Phenomena, 100(1-3):191–213.

[Hwang et al., 2004] Hwang, J., Timusk, T., and Gu, G. D. (2004). High-transition-temperature superconductivity in the absence of the magnetic-resonance mode. Nature, 427(6976):714–717.

[Ingle et al., 2005] Ingle, N. J. C., Shen, K. M., Baumberger, F., Meevasana, W., Lu, D. H., Shen, Z.-X., Damascelli, A., Nakatsuji, S., Mao, Z. Q., Maeno, Y., Kimura, T., and Tokura, Y. (2005). Quantitative analysis of Sr_2RuO_4 angle-resolved photoemission spectra: Many-body interactions in a model Fermi liquid. Physical Review B: Solid State, 72:205114.

[Inglesfield and Plummer, 1992] Inglesfield, J. and Plummer, E. (1992). The physics of photoemission. In Kevan, S., editor, Angle-Resolved Photoemission — Theory and Current Applications, volume 74 of Studies in Surface Science and Catalysis, chapter 2, pages 15–61. Elsevier, Amsterdam.

[Ino et al., 2002] Ino, A., Kim, C., Nakamura, M., Yoshida, T., Mizokawa, T., Fujimori, A., Shen, Z.-X., Kakeshita, T., Eisaki, H., and Uchida, S. (2002). Doping-dependent evolution of the electronic structure of $La_{2-x}Sr_xCuO_4$ in the superconducting and metallic phases. Physical Review B: Solid State, 65(9):094504.

[Inosov et al., 2007a] Inosov, D. S., Borisenko, S. V., Eremin, I., Kordyuk, A. A., Zabolotnyy, V. B., Geck, J., Koitzsch, A., Fink, J., Knupfer, M., Büchner, B., Berger, H., and Follath, R. (2007a). Relation between the one-particle spectral function and dynamic spin susceptibility of superconducting $Bi_2Sr_2CaCu_2O_{8-\delta}$. Physical Review B: Solid State, 75(17):172505.

[Inosov et al., 2007b] Inosov, D. S., Fink, J., Kordyuk, A. A., Borisenko, S. V., Zabolotnyy, V. B., Schuster, R., Knupfer, M., Büchner, B., Follath, R., Dürr, H. A., Eberhardt, W., Hinkov, V.,

Keimer, B., and Berger, H. (2007b). Momentum and energy dependence of the anomalous high-energy dispersion in the electronic structure of high temperature superconductors. Physical Review Letters, 99(23):237002.

[Inosov et al., 2008] Inosov, D. S., Schuster, R., Kordyuk, A. A., Fink, J., Borisenko, S. V., Zabolotnyy, V. B., Evtushinsky, D. V., Knupfer, M., Büchner, B., Follath, R., and Berger, H. (2008). Excitation energy map of high-energy dispersion anomalies in cuprates. Physical Review B: Solid State, 77(21):212504.

[Iwasawa et al., 2008] Iwasawa, H., Douglas, J. F., Sato, K., Masui, T., Yoshida, Y., Sun, Z., Eisaki, H., Bando, H., Ino, A., Arita, M., Shimada, K., Namatame, H., Taniguchi, M., Tajima, S., Uchida, S., Saitoh, T., Dessau, D. S., and Aiura, Y. (2008). Isotopic fingerprint of electron-phonon coupling in high-T_c cuprates. Physical Review Letters, 101(15):157005.

[Iye, 1992] Iye, Y. (1992). Transport properties of high T_c cuprates. In Ginsberg, D. M., editor, Physical Properties of High Temperature Superconductors, volume III, chapter 4, pages 285–361. World Scientific, Singapore.

[Johnson, 1997] Johnson, P. D. (1997). Spin-polarized photoemission. Reports on Progress in Physics, 60(11):1217.

[Johnson et al., 2001] Johnson, P. D., Valla, T., Fedorov, A. V., Yusof, Z., Wells, B. O., Li, Q., Moodenbaugh, A. R., Gu, G. D., Koshizuka, N., Kendziora, C., Jian, S., and Hinks, D. G. (2001). Doping and temperature dependence of the mass enhancement observed in the cuprate $Bi_2Sr_2CaCu_2O_{8+\delta}$. Physical Review Letters, 87(17):177007.

[Johnston et al., 2010] Johnston, S., Vernay, F., Moritz, B., Shen, Z.-X., Nagaosa, N., Zaanen, J., and Devereaux, T. P. (2010). Systematic study of electron-phonon coupling to oxygen modes across the cuprates. Physical Review B: Solid State, 82(6):064513.

[Johnston et al., 2011] Johnston, S., Vishik, I. M., Lee, W. S., Schmitt, F., Uchida, S., Fujita, K., Ishida, S., Nagaosa, N., Shen, Z. X., and Devereaux, T. P. (2011). Evidence for forward scattering and coupling to acoustic phonon modes in high-T_c cuprate superconductors. arXiv:1101.1302.

[Kamihara et al., 2006] Kamihara, Y., Hiramatsu, H., Hirano, M., Kawamura, R., Yanagi, H., Kamiya, T., and Hosono, H. (2006). Iron-based layered superconductor: LaOFeP. Journal of the American Chemical Society, 128(31):10012–10013.

[Kamihara et al., 2008] Kamihara, Y., Watanabe, T., Hirano, M., and Hosono, H. (2008). Iron-based layered superconductor $La[O_{1-x}F_x]FeAs$ ($x = 0.05$–0.12) with $T_c = 26$ K. Journal of the American Chemical Society, 130(11):3296–3297.

[Kaminski et al., 2005] Kaminski, A., Fretwell, H. M., Norman, M. R., Randeria, M., Rosenkranz, S., Chatterjee, U., Campuzano, J. C., Mesot, J., Sato, T., Takahashi, T., Terashima, T., Takano, M., Kadowaki, K., Li, Z. Z., and Raffy, H. (2005). Momentum anisotropy of the scattering rate in cuprate superconductors. Physical Review B: Solid State, 71(1):014517.

[Kaminski et al., 2001] Kaminski, A., Randeria, M., Campuzano, J. C., Norman, M. R., Fretwell, H., Mesot, J., Sato, T., Takahashi, T., and Kadowaki, K. (2001). Renormalization of spectral line shape and dispersion below T_c in $Bi_2Sr_2CaCu_2O_{8+\delta}$. Physical Review Letters, 86(6):1070–1073.

[Kampf and Schrieffer, 1990] Kampf, A. P. and Schrieffer, J. R. (1990). Spectral function and photoemission spectra in antiferromagnetically correlated metals. Physical Review B: Solid State, 42(13):7967–7974.

[Kanigel et al., 2006] Kanigel, A., Norman, M. R., Randeria, M., Chatterjee, U., Souma, S., Kaminski, A., Fretwell, H. M., Rosenkranz, S., Shi, M., Sato, T., Takahashi, T., Li, Z. Z., Raffy, H., Kadowaki, K., Hinks, D., Ozyuzer, L., and Campuzano, J. C. (2006). Evolution of the pseudogap from Fermi arcs to the nodal liquid. Nature Physics, 2(7):447–451.

[Kevan, 1983] Kevan, S. D. (1983). Design of a high-resolution angle-resolving electron energy analyzer. Review of Scientific Instruments, 54(11):1441–1445.

[Kim et al., 2003] Kim, T. K., Kordyuk, A. A., Borisenko, S. V., Koitzsch, A., Knupfer, M., Berger, H., and Fink, J. (2003). Doping dependence of the mass enhancement in $(Pb,Bi)_2Sr_2CaCu_2O_8$ at the antinodal point in the superconducting and normal states. Physical Review Letters, 91(16):167002.

[King et al., 2011] King, P. D. C., Rosen, J. A., Meevasana, W., Tamai, A., Rozbicki, E., Comin, R., Levy, G., Fournier, D., Yoshida, Y., Eisaki, H., Shen, K. M., Ingle, N. J. C., Damascelli, A., and Baumberger, F. (2011). Structural origin of apparent Fermi surface pockets in angle-resolved photoemission of $Bi_2Sr_{2-x}La_xCuO_{6+\delta}$. Physical Review Letters, 106(12):127005.

[Kiss et al., 2005] Kiss, T., Kanetaka, F., Yokoya, T., Shimojima, T., Kanai, K., Shin, S., Onuki, Y., Togashi, T., Zhang, C., Chen, C. T., and Watanabe, S. (2005). Photoemission spectroscopic evidence of gap anisotropy in an f-electron superconductor. Physical Review Letters, 94(5):057001.

[Kittel, 1996] Kittel, C. (1996). Introduction to Solid State Physics. John Wiley & Sons, Inc., New York, 7th edition.

[Koitzsch et al., 2004a] Koitzsch, A., Borisenko, S. V., Kordyuk, A. A., Kim, T. K., Knupfer, M., Fink, J., Berger, H., and Follath, R. (2004a). Doping dependence of many-body effects along the nodal direction in the high-T_c cuprate $(Bi,Pb)_2Sr_2CaCu_2O_8$. Physical Review B: Solid State, 69(14):140507.

[Koitzsch et al., 2004b] Koitzsch, A., Borisenko, S. V., Kordyuk, A. A., Kim, T. K., Knupfer, M., Fink, J., Golden, M. S., Koops, W., Berger, H., Keimer, B., Lin, C. T., Ono, S., Ando, Y., and Follath, R. (2004b). Origin of the shadow Fermi surface in Bi-based cuprates. Physical Review B: Solid State, 69(22):220505.

[Kondo et al., 2007] Kondo, T., Takeuchi, T., Kaminski, A., Tsuda, S., and Shin, S. (2007). Evidence for two energy scales in the superconducting state of optimally doped $(Bi,Pb)_2(Sr,La)_2CuO_{6+\delta}$. Physical Review Letters, 98(26):267004.

[Koralek, 2006] Koralek, J. D. (2006). Laser Based Angle-Resolved Photoemission Spectroscopy and High T_c Superconductivity. PhD thesis, University of Colorado at Boulder.

[Koralek et al., 2007] Koralek, J. D., Douglas, J. F., Plumb, N. C., Griffith, J. D., Cundiff, S. T., Kapteyn, H. C., Murnane, M. M., and Dessau, D. S. (2007). Experimental setup for low-energy laser-based angle resolved photoemission spectroscopy. Review of Scientific Instruments, 78(5):053905.

[Koralek et al., 2006] Koralek, J. D., Douglas, J. F., Plumb, N. C., Sun, Z., Fedorov, A. V., Murnane, M. M., Kapteyn, H. C., Cundiff, S. T., Aiura, Y., Oka, K., Eisaki, H., and Dessau, D. S. (2006). Laser based angle-resolved photoemission, the sudden approximation, and quasiparticle-like spectral peaks in $Bi_2Sr_2CaCu_2O_{8+\delta}$. Physical Review Letters, 96(1):017005.

[Kordyuk and Borisenko, 2005] Kordyuk, A. A. and Borisenko, S. V. (2005). Details of the photoemission spectra analysis. ArXiv Condensed Matter e-prints. http://arxiv.org/abs/cond-mat/0510421.

[Kordyuk et al., 2002] Kordyuk, A. A., Borisenko, S. V., Golden, M. S., Legner, S., Nenkov, K. A., Knupfer, M., Fink, J., Berger, H., Forró, L., and Follath, R. (2002). Doping dependence of the Fermi surface in $(Bi,Pb)_2Sr_2CaCu_2O_{8+\delta}$. Physical Review B: Solid State, 66(1):014502.

[Kordyuk et al., 2005] Kordyuk, A. A., Borisenko, S. V., Koitzsch, A., Fink, J., Knupfer, M., and Berger, H. (2005). Bare electron dispersion from experiment: Self-consistent self-energy analysis of photoemission data. Physical Review B: Solid State, 71(21):214513.

[Kordyuk et al., 2004] Kordyuk, A. A., Borisenko, S. V., Yaresko, A. N., Drechsler, S.-L., Rosner, H., Kim, T. K., Koitzsch, A., Nenkov, K. A., Knupfer, M., Fink, J., Follath, R., Berger, H., Keimer, B., Ono, S., and Ando, Y. (2004). Evidence for CuO conducting band splitting in the nodal direction of $Bi_2Sr_2CaCu_2O_{8+\delta}$. Physical Review B: Solid State, 70(21):214525.

[Kovaleva et al., 2004] Kovaleva, N. N., Boris, A. V., Holden, T., Ulrich, C., Liang, B., Lin, C. T., Keimer, B., Bernhard, C., Tallon, J. L., Munzar, D., and Stoneham, A. M. (2004). c-axis lattice dynamics in Bi-based cuprate superconductors. Physical Review B: Solid State, 69(5):054511.

[Langer et al., 1995] Langer, M., Schmalian, J., Grabowski, S., and Bennemann, K. H. (1995). Theory for the excitation spectrum of high-T_c superconductors: Quasiparticle dispersion and shadows of the Fermi surface. Physical Review Letters, 75(24):4508–4511.

[Lanzara et al., 2001] Lanzara, A., Bogdanov, P. V., Zhou, X. J., Kellar, S. A., Feng, D. L., Lu, E. D., Yoshida, T., Eisaki, H., Fujimori, A., Kishio, K., Shimoyama, J.-I., Noda, T., Uchida, S., Hussain, Z., and Shen, Z.-X. (2001). Evidence for ubiquitous strong electron-phonon coupling in high-temperature superconductors. Nature, 412(6846):510–514.

[Laughlin and Pines, 2000] Laughlin, R. B. and Pines, D. (2000). The theory of everything. Proceedings of the National Academy of Sciences of the United States of America, 97(1):28–31.

[Le Tacon et al., 2006] Le Tacon, M., Sacuto, A., Georges, A., Kotliar, G., Gallais, Y., Colson, D., and Forget, A. (2006). Two energy scales and two distinct quasiparticle dynamics in the superconducting state of underdoped cuprates. Nature Physics, 2(8):537–543.

[LeBoeuf et al., 2007] LeBoeuf, D., Doiron-Leyraud, N., Levallois, J., Daou, R., Bonnemaison, J.-B., Hussey, N. E., Balicas, L., Ramshaw, B. J., Liang, R., Bonn, D. A., Hardy, W. N., Adachi, S., Proust, C., and Taillefer, L. (2007). Electron pockets in the Fermi surface of hole-doped high-T_c superconductors. Nature, 450(7169):533–536.

[Lee et al., 2008] Lee, W. S., Meevasana, W., Johnston, S., Lu, D. H., Vishik, I. M., Moore, R. G., Eisaki, H., Kaneko, N., Devereaux, T. P., and Shen, Z. X. (2008). Superconductivity-induced self-energy evolution of the nodal electron of optimally doped $Bi_2Sr_2Ca_{0.92}Y_{0.08}Cu_2O_{8+\delta}$. Physical Review B: Solid State, 77(14):140504.

[Lee et al., 2007] Lee, W. S., Vishik, I. M., Tanaka, K., Lu, D. H., Sasagawa, T., Nagaosa, N., Devereaux, T. P., Hussain, Z., and Shen, Z.-X. (2007). Abrupt onset of a second energy gap at the superconducting transition of underdoped bi2212. Nature, 450(7166):81–84.

[Li et al., 2006] Li, J.-X., Wu, C.-Q., and Lee, D.-H. (2006). Checkerboard charge density wave and pseudogap of high-T_c cuprate. Physical Review B: Solid State, 74(18):184515.

[Littlewood and Varma, 1992] Littlewood, P. B. and Varma, C. M. (1992). Phenomenology of the superconductive state of a marginal Fermi liquid. Physical Review B: Solid State, 46(1):405–420.

[Liu et al., 1992] Liu, R., Klein, M. V., Han, P. D., and Payne, D. A. (1992). Raman scattering from A_g and B_{1g} phonons in $Bi_2Sr_2Ca_{n-1}Cu_nO_{2n+4}$ ($n = 1, 2$). Physical Review B: Solid State, 45(13):7392–7396.

[Loeser et al., 1996] Loeser, A. G., Shen, Z.-X., Dessau, D. S., Marshall, D. S., Park, C. H., Fournier, P., and Kapitulnik, A. (1996). Excitation gap in the normal state of underdoped $Bi_2Sr_2CaCu_2O_{8+\delta}$. Science, 273(5273):325–329.

[Loeser et al., 1997] Loeser, A. G., Shen, Z.-X., Schabel, M. C., Kim, C., Zhang, M., Kapitulnik, A., and Fournier, P. (1997). Temperature and doping dependence of the Bi-Sr-Ca-Cu-O electronic structure and fluctuation effects. Physical Review B: Solid State, 56(21):14185–14189.

[Louie, 1992] Louie, S. G. (1992). Quasiparticle excitations and photoemission. In Kevan, S., editor, Angle-Resolved Photoemission — Theory and Current Applications, volume 74, chapter 3, pages 63–98. Elsevier.

[Lucy, 1974] Lucy, L. B. (1974). An iterative technique for the rectification of observed distributions. Astronomical Journal, 79:745.

[Ma et al., 2008] Ma, J.-H., Pan, Z.-H., Niestemski, F. C., Neupane, M., Xu, Y.-M., Richard, P., Nakayama, K., Sato, T., Takahashi, T., Luo, H.-Q., Fang, L., Wen, H.-H., Wang, Z., Ding, H., and Madhavan, V. (2008). Coexistence of competing orders with two energy gaps in real and momentum space in the high temperature superconductor $Bi_2Sr_{2-x}La_xCuO_{6+\delta}$. Physical Review Letters, 101(20):207002.

[Mahan, 2000] Mahan, G. D. (2000). Many-Particle Physics. Plenum Press, New York, 3rd edition.

[Mannella et al., 2004] Mannella, N., Marchesini, S., Kay, A., Nambu, A., Gresch, T., Yang, S.-H., Mun, B., Bussat, J., Rosenhahn, A., and Fadley, C. (2004). Correction of non-linearity effects in detectors for electron spectroscopy. Journal of Electron Spectroscopy and Related Phenomena, 141(1):45–59.

[Mans et al., 2006] Mans, A., Santoso, I., Huang, Y., Siu, W. K., Tavaddod, S., Arpiainen, V., Lindroos, M., Berger, H., Strocov, V. N., Shi, M., Patthey, L., and Golden, M. S. (2006). Experimental proof of a structural origin for the shadow Fermi surface of $Bi_2Sr_2CaCu_2O_{8+\delta}$. Physical Review Letters, 96(10):107007.

[Manske et al., 2001] Manske, D., Eremin, I., and Bennemann, K. H. (2001). Analysis of the elementary excitations in high-T_c cuprates: Explanation of the new energy scale observed by angle-resolved photoemission spectroscopy. Physical Review Letters, 87(17):177005.

[Markiewicz, 2004] Markiewicz, R. S. (2004). Bridging k and q space in the cuprates: Comparing angle-resolved photoemission and STM results. Physical Review B: Solid State, 69(21):214517.

[Meevasana et al., 2008] Meevasana, W., Baumberger, F., Tanaka, K., Schmitt, F., Dunkel, W. R., Lu, D. H., Mo, S.-K., Eisaki, H., and Shen, Z.-X. (2008). Extracting the spectral function of the cuprates by a full two-dimensional analysis: Angle-resolved photoemission spectra of $Bi_2Sr_2CuO_6$. Physical Review B: Solid State, 77(10):104506.

[Meevasana et al., 2006] Meevasana, W., Ingle, N. J. C., Lu, D. H., Shi, J. R., Baumberger, F., Shen, K. M., Lee, W. S., Cuk, T., Eisaki, H., Devereaux, T. P., Nagaosa, N., Zaanen, J., and Shen, Z.-X. (2006). Doping dependence of the coupling of electrons to bosonic modes in the single-layer high-temperature $Bi_2Sr_2CuO_6$ superconductor. Physical Review Letters, 96(15):157003.

[Meng et al., 2009] Meng, J., Liu, G., Zhang, W., Zhao, L., Liu, H., Jia, X., Mu, D., Liu, S., Dong, X., Zhang, J., Lu, W., Wang, G., Zhou, Y., Zhu, Y., Wang, X., Xu, Z., Chen, C., and Zhou, X. J. (2009). Coexistence of Fermi arcs and Fermi pockets in a high-t_c copper oxide superconductor. Nature, 462(7271):335–338.

[Misochko and Sherman, 2000] Misochko, O. V. and Sherman, E. Y. (2000). Resonant electronic Raman scattering in optimally doped $Bi_2Sr_2CaCu_2O_{8+x}$ superconductor. Journal of Physics: Condensed Matter, 12(42):9095.

[Mook et al., 1993] Mook, H. A., Yethiraj, M., Aeppli, G., Mason, T. E., and Armstrong, T. (1993). Polarized neutron determination of the magnetic excitations in $YBa_2Cu_3O_7$. Physical Review Letters, 70(22):3490–3493.

[Moritz et al., 2010] Moritz, B., Johnston, S., and Devereaux, T. (2010). Insights on the cuprate high energy anomaly observed in ARPES. Journal of Electron Spectroscopy and Related Phenomena, 181(1):31–34.

[Müller and Bednorz, 1987] Müller, K. A. and Bednorz, J. G. (1987). The discovery of a class of high-temperature superconductors. Science, 237(4819):1133–1139.

[Nakayama et al., 2007] Nakayama, K., Dobashi, T., Sato, T., Takahashi, T., Kondo, T., Takeuchi, T., Kudo, K., and Kobayashi, N. (2007). Origin of shadow bands in high-T_c cuprate superconductors studied by high-resolution angle-resolved photoemission spectroscopy. Physica C: Superconductivity, 463-465:48–51.

[Nakayama et al., 2006] Nakayama, K., Sato, T., Dobashi, T., Terashima, K., Souma, S., Matsui, H., Takahashi, T., Campuzano, J. C., Kudo, K., Sasaki, T., Kobayashi, N., Kondo, T., Takeuchi, T., Kadowaki, K., Kofu, M., and Hirota, K. (2006). Shadow bands in single-layered $Bi_2Sr_2CuO_{6+\delta}$ studied by angle-resolved photoemission spectroscopy. Physical Review B: Solid State, 74(5):054505.

[Nakayama et al., 2009] Nakayama, K., Sato, T., Sekiba, Y., Terashima, K., Richard, P., Takahashi, T., Kudo, K., Okumura, N., Sasaki, T., and Kobayashi, N. (2009). Evolution of a pairing-induced pseudogap from the superconducting gap of $(Bi,Pb)_2Sr_2CuO_6$. Physical Review Letters, 102(22):227006.

[Nazarenko and Dagotto, 1996] Nazarenko, A. and Dagotto, E. (1996). Possible phononic mechanism for $d_{x^2-y^2}$ superconductivity in the presence of short-range antiferromagnetic correlations. Physical Review B: Solid State, 53(6):R2987–R2990.

[Norman, 2010] Norman, M. R. (2010). Fermi-surface reconstruction and the origin of high-temperature superconductivity. Physics, 3:86.

[Norman and Ding, 1998] Norman, M. R. and Ding, H. (1998). Collective modes and the superconducting-state spectral function of $Bi_2Sr_2CaCu_2O_8$. Physical Review B: Solid State, 57(18):R11089–R11092.

[Norman et al., 1998] Norman, M. R., Ding, H., Randeria, M., Campuzano, J. C., Yokoya, T., Takeuchi, T., Takahashi, T., Mochiku, T., Kadowaki, K., Guptasarma, P., and Hinks, D. G. (1998). Destruction of the fermi surface in underdoped high-tc superconductors. Nature, 392(6672):157–160.

[Normand et al., 1996] Normand, B., Kohno, H., and Fukuyama, H. (1996). Spin-phonon coupling in the single-layer extended $t - J$ model. Physical Review B: Solid State, 53(2):856–870.

[Nunner et al., 1999] Nunner, T. S., Schmalian, J., and Bennemann, K. H. (1999). Influence of electron-phonon interaction on spin-fluctuation-induced superconductivity. Physical Review B: Solid State, 59(13):8859–8868.

[Orenstein and Vishwanath, 2010] Orenstein, J. and Vishwanath, A. (2010). Doped Mott insulators: Breaking through to the other side. Nature Physics, 6(8):566–567.

[Osterwalder et al., 1995] Osterwalder, J., Aebi, P., Schwaller, P., Schlapbach, L., Shimoda, M., Mochiku, T., and Kadowaki, K. (1995). Angle-resolved photoemission experiments on $Bi_2Sr_2CaCu_2O_{8+\delta}$(001). Applied Physics A: Materials Science & Processing, 60(3):247–254.

[Pailhès et al., 2004] Pailhès, S., Sidis, Y., Bourges, P., Hinkov, V., Ivanov, A., Ulrich, C., Regnault, L. P., and Keimer, B. (2004). Resonant magnetic excitations at high energy in superconducting $YBa_2Cu_3O_{6.85}$. Physical Review Letters, 93(16):167001.

[Pintschovius, 2005] Pintschovius, L. (2005). Electron-phonon coupling effects explored by inelastic neutron scattering. Physica Status Solidi B: Basic Research, 242(1):30–50.

[Plumb et al., 2010] Plumb, N. C., Reber, T. J., Koralek, J. D., Sun, Z., Douglas, J. F., Aiura, Y., Oka, K., Eisaki, H., and Dessau, D. S. (2010). Low-energy (< 10 meV) feature in the nodal electron self-energy and strong temperature dependence of the Fermi velocity in $Bi_2Sr_2CaCu_2O_{8+\delta}$. Physical Review Letters, 105(4):046402.

[Powell, 1974] Powell, C. (1974). Attenuation lengths of low-energy electrons in solids. Surface Science, 44(1):29–46.

[Rameau et al., 2009] Rameau, J. D., Yang, H.-B., Gu, G. D., and Johnson, P. D. (2009). Coupling of low-energy electrons in the optimally doped $Bi_2Sr_2CaCu_2O_{8+\delta}$ superconductor to an optical phonon mode. Physical Review B: Solid State, 80(18):184513.

[Reber et al., 2010a] Reber, T. J., Plumb, N. C., and Dessau, D. S. (2010a). An algorithm to correct the counting rate nonlinearity in a popular electron spectrometer. Unpublished.

[Reber et al., 2010b] Reber, T. J., Plumb, N. C., Sun, Z., Iwasawa, H., Gu, G., Eisaki, H., Aiura, Y., and Dessau, D. S. (2010b). Intrinsic gaps and scattering rates of $Bi_2Sr_2CaCu_2O_8$ from ARPES tunneling spectra. Unpublished.

[Reichardt, 1996] Reichardt, W. (1996). Cu-O bond-stretching vibrations in $YBa_2Cu_3O_7$ studied by inelastic neutron scattering. Journal of Low Temperature Physics, 105(3):807–812.

[Reinert and Hüfner, 2005] Reinert, F. and Hüfner, S. (2005). Photoemission spectroscopy — from early days to recent applications. New Journal of Physics, 7(1):97.

[Reinert and Hüfner, 2007] Reinert, F. and Hüfner, S. (2007). Photoemission spectroscopy with very high energy resolution: Studying the influence of electronic correlations on the millielectronvolt scale. In Hüfner, S., editor, Very High Resolution Photoelectron Spectroscopy, volume 715 of Lecture Notes in Physics, chapter 2, pages 13–53. Springer, Berlin.

[Reznik, 2010] Reznik, D. (2010). Giant electron-phonon anomaly in doped La_2CuO_4 and other cuprates. Advances in Condensed Matter Physics, 2010:523549.

[Reznik et al., 2004] Reznik, D., Bourges, P., Pintschovius, L., Endoh, Y., Sidis, Y., Masui, T., and Tajima, S. (2004). Dispersion of magnetic excitations in optimally doped superconducting $YBa_2Cu_3O_6.95$. Physical Review Letters, 93(20):207003.

[Richardson, 1972] Richardson, W. H. (1972). Bayesian-based iterative method of image restoration. Journal of the Optical Society of America, 62:55.

[Rossat-Mignod et al., 1991] Rossat-Mignod, J., Regnault, L., Vettier, C., Bourges, P., Burlet, P., Bossy, J., Henry, J., and Lapertot, G. (1991). Neutron scattering study of the $YBa_2Cu_3O_{6+x}$ system. Physica C: Superconductivity, 185-189(Part 1):86–92.

[Ruiz and Badía-Majós, 2009] Ruiz, H. S. and Badía-Majós, A. (2009). Nature of the nodal kink in angle-resolved photoemission spectra of cuprate superconductors. Physical Review B: Solid State, 79(5):054528.

[Sahrakorpi et al., 2005] Sahrakorpi, S., Lindroos, M., Markiewicz, R. S., and Bansil, A. (2005). Evolution of midgap states and residual three dimensionality in $La_{2-x}Sr_xCuO_4$. Physical Review Letters, 95(15):157601.

[Saitoh et al., 2000] Saitoh, Y., Kimura, H., Suzuki, Y., Nakatani, T., Matsushita, T., Muro, T., Miyahara, T., Fujisawa, M., Soda, K., Ueda, S., Harada, H., Kotsugi, M., Sekiyama, A., and Suga, S. (2000). Performance of a very high resolution soft x-ray beamline BL25SU with a twin-helical undulator at SPring-8. Review of Scientific Instruments, 71(9):3254–3259.

[Sato et al., 2007] Sato, T., Terashima, K., Nakayama, K., Takahashi, T., Kadowaki, K., Kofu, M., and Hirota, K. (2007). Bogoliubov quasiparticle and low-energy dispersion kink in the superconducting state of $La_{1.85}Sr_{0.15}CuO_4$. Physica C: Superconductivity, 460-462(Part 2):864–865.

[Sawatzky, 2005] Sawatzky, G. A. (2005). Private communication.

[Schabel et al., 1998] Schabel, M. C., Park, C.-H., Matsuura, A., Shen, Z.-X., Bonn, D. A., Liang, R., and Hardy, W. N. (1998). Angle-resolved photoemission on untwinned $YBa_2Cu_3O_{6.95}$. II. Determination of Fermi surfaces. Physical Review B: Solid State, 57(10):6107–6115.

[Schachinger and Carbotte, 2008] Schachinger, E. and Carbotte, J. P. (2008). Finite band inversion of angular-resolved photoemission in $Bi_2Sr_2CaCu_2O_{8+\delta}$ and comparison with optics. Physical Review B: Solid State, 77(9):094524.

[Schachinger and Carbotte, 2009] Schachinger, E. and Carbotte, J. P. (2009). Energy of the bosonic kinks in the quasiparticle spectrum of cuprate superconductors. Physical Review B: Solid State, 80(9):094521.

[Schachinger et al., 2009] Schachinger, E., Carbotte, J. P., and Timusk, T. (2009). Characteristics of oxygen isotope substitutions in the quasiparticle spectrum of $Bi_2Sr_2CaCu_2O_{8+\delta}$. Europhysics Letters, 86(6):67003.

[Seah and Dench, 1979] Seah, M. P. and Dench, W. A. (1979). Quantitative electron spectroscopy of surfaces: A standard data base for electron inelastic mean free paths in solids. Surface and Interface Analysis, 1(1):2–11.

[Seah et al., 1999] Seah, M. P., Gilmore, I. S., and Spencer, S. J. (1999). Signal linearity in XPS counting systems. Journal of Electron Spectroscopy and Related Phenomena, 104(1-3):73–89.

[Seah and Tosa, 1992] Seah, M. P. and Tosa, M. (1992). Linearity in electron counting and detection systems. Surface and Interface Analysis, 18(3):240–246.

[Shen et al., 2005] Shen, K. M., Ronning, F., Lu, D. H., Baumberger, F., Ingle, N. J. C., Lee, W. S., Meevasana, W., Kohsaka, Y., Azuma, M., Takano, M., Takagi, H., and Shen, Z.-X. (2005). Nodal quasiparticles and antinodal charge ordering in $Ca_{2-x}Na_xCuO_2Cl_2$. Science, 307(5711):901–904.

[Shen et al., 1993] Shen, Z.-X., Dessau, D. S., Wells, B. O., King, D. M., Spicer, W. E., Arko, A. J., Marshall, D., Lombardo, L. W., Kapitulnik, A., Dickinson, P., Doniach, S., DiCarlo, J., Loeser, T., and Park, C. H. (1993). Anomalously large gap anisotropy in the $a-b$ plane of $Bi_2Sr_2CaCu_2O_{8+\delta}$. Physical Review Letters, 70(10):1553–1556.

[Shi et al., 2004] Shi, J., Tang, S.-J., Wu, B., Sprunger, P. T., Yang, W. L., Brouet, V., Zhou, X. J., Hussain, Z., Shen, Z.-X., Zhang, Z., and Plummer, E. W. (2004). Direct extraction of the Eliashberg function for electron-phonon coupling: A case study of Be($10\bar{1}0$). Physical Review Letters, 92(18):186401.

[Shimojima et al., 2005] Shimojima, T., Yokoya, T., Kiss, T., Chainani, A., Shin, S., Togashi, T., Watanabe, S., Zhang, C., Chen, C. T., Takada, K., Sasaki, T., Sakurai, H., and Takayama-Muromachi, E. (2005). Laser-excited ultrahigh-resolution photoemission spectroscopy of $Na_xCoO_2 \cdot yH_2O$: Evidence for pseudogap formation. Physical Review B: Solid State, 71(2):020505.

[Smith and Kevan, 1992] Smith, N. and Kevan, S. (1992). Introduction. In Kevan, S., editor, Angle-Resolved Photoemission — Theory and Current Applications, volume 74 of Studies in Surface Science and Catalysis, chapter 1, pages 1–14. Elsevier, Amsterdam.

[Smith et al., 1993] Smith, N. V., Thiry, P., and Petroff, Y. (1993). Photoemission linewidths and quasiparticle lifetimes. Physical Review B: Solid State, 47(23):15476–15481.

[Souma et al., 2007] Souma, S., Sato, T., Takahashi, T., and Baltzer, P. (2007). High-intensity xenon plasma discharge lamp for bulk-sensitive high-resolution photoemission spectroscopy. Review of Scientific Instruments, 78(12):123104.

[Stock et al., 2005] Stock, C., Buyers, W. J. L., Cowley, R. A., Clegg, P. S., Coldea, R., Frost, C. D., Liang, R., Peets, D., Bonn, D., Hardy, W. N., and Birgeneau, R. J. (2005). From incommensurate to dispersive spin-fluctuations: The high-energy inelastic spectrum in superconducting $YBa_2Cu_3O_{6.5}$. Physical Review B: Solid State, 71(2):024522.

[Strocov et al., 2010] Strocov, V. N., Schmitt, T., Flechsig, U., Schmidt, T., Imhof, A., Chen, Q., Raabe, J., Betemps, R., Zimoch, D., Krempasky, J., Wang, X., Grioni, M., Piazzalunga, A., and Patthey, L. (2010). High-resolution soft X-ray beamline ADRESS at the Swiss Light Source for resonant inelastic X-ray scattering and angle-resolved photoelectron spectroscopies. Journal of Synchrotron Radiation, 17(5):631–643.

[Strocov et al., 1997] Strocov, V. N., Starnberg, H. I., Nilsson, P. O., Brauer, H. E., and Holleboom, L. J. (1997). New method for absolute band structure determination by combining photoemission with very-low-energy electron diffraction: Application to layered VSe_2. Physical Review Letters, 79(3):467–470.

[Sun et al., 2006] Sun, X. F., Ono, S., Abe, Y., Komiya, S., Segawa, K., and Ando, Y. (2006). Electronic inhomogeneity and breakdown of the universal thermal conductivity of cuprate superconductors. Physical Review Letters, 96(1):017008.

[Tanaka et al., 2006] Tanaka, K., Lee, W. S., Lu, D. H., Fujimori, A., Fujii, T., Risdiana, Terasaki, I., Scalapino, D. J., Devereaux, T. P., Hussain, Z., and Shen, Z.-X. (2006). Distinct Fermi-momentum-dependent energy gaps in deeply underdoped Bi2212. Science, 314(5807):1910–1913.

[Tinkham, 1996] Tinkham, M. (1996). Introduction to Superconductivity. McGraw-Hill, New York, 2 edition.

[Tranquada et al., 1995] Tranquada, J. M., Sternlieb, B. J., Axe, J. D., Nakamura, Y., and Uchida, S. (1995). Evidence for stripe correlations of spins and holes in copper oxide. Nature, 375(6532):561–563.

[Tranquada et al., 2004] Tranquada, J. M., Woo, H., Perring, T. G., Goka, H., Gu, G. D., Xu, G., Fujita, M., and Yamada, K. (2004). Quantum magnetic excitations from stripes in copper oxide superconductors. Nature, 429:534–538.

[Tsuei and Kirtley, 2008] Tsuei, C. C. and Kirtley, J. R. (2008). Phase-sensitive tests of pairing symmetry in cuprate superconductors. In Bennemann, K. H. and Ketterson, J. B., editors, Superconductivity, volume 1: Conventional and Unconventional Superconductors, pages 869–921–921. Springer, Berlin.

[Tsvetkov et al., 1999] Tsvetkov, A. A., Dulić, D., van der Marel, D., Damascelli, A., Kaljushnaia, G. A., Gorina, J. I., Senturina, N. N., Kolesnikov, N. N., Ren, Z. F., Wang, J. H., Menovsky, A. A., and Palstra, T. T. M. (1999). Systematics of *c*-axis phonons in the thallium- and bismuth-based cuprate superconductors. Physical Review B: Solid State, 60(18):13196–13205.

[Valla et al., 2000] Valla, T., Fedorov, A. V., Johnson, P. D., Li, Q., Gu, G. D., and Koshizuka, N. (2000). Temperature dependent scattering rates at the Fermi surface of optimally doped $Bi_2Sr_2CaCu_2O_{8+\delta}$. Physical Review Letters, 85(4):828–831.

[Valla et al., 2007] Valla, T., Kidd, T. E., Yin, W.-G., Gu, G. D., Johnson, P. D., Pan, Z.-H., and Fedorov, A. V. (2007). High-energy kink observed in the electron dispersion of high-temperature cuprate superconductors. Physical Review Letters, 98(16):167003.

[van Delft and Kes, 2010] van Delft, D. and Kes, P. (2010). The discovery of superconductivity. Physics Today, 63(9):38–43.

[Varma et al., 1989] Varma, C. M., Littlewood, P. B., Schmitt-Rink, S., Abrahams, E., and Ruckenstein, A. E. (1989). Phenomenology of the normal state of Cu-O high-temperature superconductors. Physical Review Letters, 63(18):1996–1999.

[Veenstra et al., 2010] Veenstra, C. N., Goodvin, G. L., Berciu, M., and Damascelli, A. (2010). Elusive electron-phonon coupling in quantitative analyses of the spectral function. Physical Review B: Solid State, 82(1):012504.

[VG Scienta AB, 2009] VG Scienta AB (2009). Electron spectrometer: Scienta R4000. Online at `http://www.vgscienta.com/_resources/File/R4000%20data%20sheet%20v3.5%20+%20model%20overview%20v1.4%20web.pdf`. Brochure.

[Vishik et al., 2010] Vishik, I. M., Lee, W. S., Schmitt, F., Moritz, B., Sasagawa, T., Uchida, S., Fujita, K., Ishida, S., Zhang, C., Devereaux, T. P., and Shen, Z. X. (2010). Doping-dependent nodal Fermi velocity of the high-temperature superconductor $Bi_2Sr_2CaCu_2O_{8+\delta}$ revealed using high-resolution angle-resolved photoemission spectroscopy. Physical Review Letters, 104(20):207002.

[Vos et al., 2009] Vos, M., Went, M. R., and Weigold, E. (2009). Electron spectroscopy using two-dimensional electron detection and a camera in a single electron counting mode. Review of Scientific Instruments, 80(6):063302.

[Wang et al., 2009] Wang, Q., Sun, Z., Rotenberg, E., Berger, H., Eisaki, H., Aiura, Y., and Dessau, D. S. (2009). Energy-dependent scaling of incoherent spectral weight and the origin of the waterfalls in high-T_c cuprates. ArXiv e-prints. http://arxiv.org/abs/0910.2787.

[Wannberg, 2009] Wannberg, B. (2009). Electron optics development for photo-electron spectrometers. Nuclear Instruments and Methods in Physics Research Section A: Accelerators, Spectrometers, Detectors and Associated Equipment, 601(1-2):182–194.

[Wells et al., 1992] Wells, B. O., Shen, Z. X., Dessau, D. S., Spicer, W. E., Mitzi, D. B., Lombardo, L., Kapitulnik, A., and Arko, A. J. (1992). Evidence for k-dependent, in-plane anisotropy of the superconducting gap in $Bi_2Sr_2CaCu_2O_{8+\delta}$. Physical Review B: Solid State, 46(18):11830–11834.

[Withers et al., 1988] Withers, R. L., Thompson, J. G., Wallenberg, L. R., FitzGerald, J. D., Anderson, J. S., and Hyde, B. G. (1988). A transmission electron microscope and group theoretical study of the new Bi-based high-T_c superconductors and some closely related Aurivillius phases. Journal of Physics C: Solid State Physics, 21(36):6067.

[Wolf, 1997] Wolf, M. (1997). Femtosecond dynamics of electronic excitations at metal surfaces. Surface Science, 377-379:343–349.

[Xiao et al., 2007] Xiao, Y., Sato, T., Terashima, K., Matsui, H., Takahashi, T., Kofu, M., and Hirota, K. (2007). Single-particle excitation gap in $La_{2-x}Sr_xCuO_4$ studied by high-resolution angle-resolved photoemission. Physica C: Superconductivity, 463-465:44–47.

[Xu et al., 2009] Xu, G., Gu, G. D., Hucker, M., Fauque, B., Perring, T. G., Regnault, L. P., and Tranquada, J. M. (2009). Testing the itinerancy of spin dynamics in superconducting $Bi_2Sr_2CaCu_2O_{8+\delta}$. Nature Physics, 5(9):642–646.

[Yamamoto et al., 1990] Yamamoto, A., Onoda, M., Takayama-Muromachi, E., Izumi, F., Ishigaki, T., and Asano, H. (1990). Rietveld analysis of the modulated structure in the superconducting oxide $Bi_2(Sr,Ca)_3Cu_2O_{8+x}$. Physical Review B: Solid State, 42(7):4228–4239.

[Yamasaki et al., 2007] Yamasaki, T., Yamazaki, K., Ino, A., Arita, M., Namatame, H., Taniguchi, M., Fujimori, A., Shen, Z.-X., Ishikado, M., and Uchida, S. (2007). Unmasking the nodal quasiparticle dynamics in cuprate superconductors using low-energy photoemission. Physical Review B: Solid State, 75(14):140513(R).

[Yang et al., 2008] Yang, H.-B., Rameau, J. D., Johnson, P. D., Valla, T., Tsvelik, A., and Gu, G. D. (2008). Emergence of preformed Cooper pairs from the doped Mott insulating state in $Bi_2Sr_2CaCu_2O_{8+\delta}$. Nature, 456(7218):77–80.

[Yokoya et al., 2001] Yokoya, T., Fukushima, A., Kiss, T., Kobayashi, K., Shin, S., Moriguchi, K., Shintani, A., Fukuoka, H., and Yamanaka, S. (2001). Electronic structure and superconducting gap of silicon clathrate Ba_8Si_{46} studied with ultrahigh-resolution photoemission spectroscopy. Physical Review B: Solid State, 64(17):172504.

[Yokoya et al., 2000] Yokoya, T., Kiss, T., Watanabe, T., Shin, S., Nohara, M., Takagi, H., and Oguchi, T. (2000). Ultrahigh-resolution photoemission spectroscopy of Ni borocarbides: Direct observation of the superconducting gap and a change in gap anisotropy by impurity. Physical Review Letters, 85(23):4952–4955.

[Zhang et al., 2008a] Zhang, W., Liu, G., Meng, J., Zhao, L., Liu, H., Dong, X., Lu, W., Wen, J. S., Xu, Z. J., Gu, G. D., Sasagawa, T., Wang, G., Zhu, Y., Zhang, H., Zhou, Y., Wang, X., Zhao, Z., Chen, C., Xu, Z., and Zhou, X. J. (2008a). High energy dispersion relations for the high temperature $Bi_2Sr_2CaCu_2O_8$ superconductor from laser-based angle-resolved photoemission spectroscopy. Physical Review Letters, 101(1):017002.

[Zhang et al., 2008b] Zhang, W., Liu, G., Zhao, L., Liu, H., Meng, J., Dong, X., Lu, W., Wen, J. S., Xu, Z. J., Gu, G. D., Sasagawa, T., Wang, G., Zhu, Y., Zhang, H., Zhou, Y., Wang, X., Zhao, Z., Chen, C., Xu, Z., and Zhou, X. J. (2008b). Identification of a new form of electron coupling in the $Bi_2Sr_2CaCu_2O_8$ superconductor by laser-based angle-resolved photoemission spectroscopy. Physical Review Letters, 100(10):107002.

[Zhou et al., 2010] Zhou, X. J., Meng, J., Peng, Y., He, J., and Yu, L. (2010). Comment on arXiv:1012.1484v1 Structural origin of apparent Fermi surface pockets in angle-resolved photoemission of Bi_2Sr_{2-x}La_xCuO_{6+\delta} by King et al. ArXiv e-prints. http://arxiv.org/abs/1012.3602v1.

[Zhou et al., 2005] Zhou, X. J., Shi, J., Yoshida, T., Cuk, T., Yang, W. L., Brouet, V., Nakamura, J., Mannella, N., Komiya, S., Ando, Y., Zhou, F., Ti, W. X., Xiong, J. W., Zhao, Z. X., Sasagawa, T., Kakeshita, T., Eisaki, H., Uchida, S., Fujimori, A., Zhang, Z., Plummer, E. W., Laughlin, R. B., Hussain, Z., and Shen, Z.-X. (2005). Multiple bosonic mode coupling in the electron self-energy of $(La_{2-x}Sr_x)CuO_4$. Physical Review Letters, 95(11):117001.

[Zhou et al., 2003] Zhou, X. J., Yoshida, T., Lanzara, A., Bogdanov, P. V., Kellar, S. A., Shen, K. M., Yang, W. L., Ronning, F., Sasagawa, T., Kakeshita, T., Noda, T., Eisaki, H., Uchida, S., Lin, C. T., Zhou, F., Xiong, J. W., Ti, W. X., Zhao, Z. X., Fujimori, A., Hussain, Z., and Shen, Z.-X. (2003). High-temperature superconductors: Universal nodal Fermi velocity. Nature, 423(6938):398–398.

[Zouros and Benis, 2002] Zouros, T. J. M. and Benis, E. P. (2002). The hemispherical deflector analyser revisited. I. Motion in the ideal $1/r$ potential, generalized entry conditions, Kepler orbits and spectrometer basic equation. Journal of Electron Spectroscopy and Related Phenomena, 125(3):221–248.

Appendix A

Electron-boson interactions: Kink energy location in the presence of an anisotropic gap

So far, we have been discussing the quantities $A(\boldsymbol{k},\omega)$ and $\Sigma(\boldsymbol{k},\omega)$ in the context of the electrons. However, at this point, it becomes necessary to make a distinction: $A(\boldsymbol{k},\omega)$, as the single-electron removal spectrum, really is the spectrum of the excitations in the electronic dispersion generated from removing an electron. These excitations are actually holes, not electrons, since the electrons are frozen by the Pauli exclusion principle until a hole is injected into the band. At first this can be a somewhat difficult pill to swallow. After all, it is the electrons that are actually detected. We must go back to section 2.5 and remind ourselves that $A(\boldsymbol{k},\omega) = -\frac{1}{\pi}\mathrm{Im}G(\boldsymbol{k},\omega)$ and that $G(\boldsymbol{k},\omega)$ comes from the overlap of the hole-injected state $\hat{c}_{\boldsymbol{k}}|\Psi_i^N\rangle$ with the superposition of excited states of the $(N-1)$-electron system $\langle\Psi_m^{N-1}|$.

In terms of what ARPES sees, this difference between electrons and holes is subtle and does not reveal itself most of the time. Indeed, it is most probable to create a photohole from a state where there is a high likelihood of finding an electron — hence why $A(\boldsymbol{k},\omega)$ reveals the dispersion of the electrons. This dispersion, in turn, relates to the effective mass, and therefore $\Sigma'(\omega)$, and by Kramers-Kronig relation, also $\Sigma''(\omega)$. All these properties of the holes, then, are also properties of the electrons and vice versa. So we were not really being too imprecise previously in talking about $A(\boldsymbol{k},\omega)$ and $\Sigma(\omega)$ with respect to the electrons.

This issue about the holes is only brought up to help illustrate the reasoning behind a crucial aspect in the analysis of the self-energy. Consider, in particular, a boson mode Ω_{boson} coupled to

the electrons at $T = 0$. In the Migdal approximation [Fetter and Walecka, 1971, Mahan, 2000], the leading term of the electron-boson coupling is just a single interaction that scatters electrons from $\boldsymbol{k_1}$ to $\boldsymbol{k_2} = \boldsymbol{k_1} + \boldsymbol{q}$. In a typical system with no gap at E_F, the coupling of this mode will lead to a step in $\Sigma''(\omega)$ at $\omega = -\Omega_{\text{boson}}$. (By Kramers-Kronig relation, there will be a feature in $\Sigma'(\omega)$ peaked at the same energy.) The reason for the step can be understood in terms of the lifetimes of the (photo)holes: If $\omega > -\Omega_{\text{boson}}$, then there are no electron states which can decay by emitting a phonon with energy Ω_{boson}. (This would require an electron to decay from above E_F, which doesn't exist at zero Kelvin.) As a result, holes in this energy range have infinite lifetimes (i.e., $\Sigma'' = 0$).[1] You can see where this is going: For $\omega > -\Omega_{\text{boson}}$, electrons are available below E_F to annihilate the holes, leading to finite hole lifetimes (i.e., $\Sigma'' \neq 0$). The situation is illustrated in Fig. A.1.

If an isotropic gap Δ is introduced centered at E_F, then clearly the step is simply located at $\omega = -\Omega_{\text{boson}} - \Delta$. In cuprates, however, the gap is $\boldsymbol{k}$-dependent. It is therefore necessary to consider that electrons must decay by exciting a boson $\Omega_{\text{boson}}(\boldsymbol{q})$ at a particular momentum transfer $\boldsymbol{q} = \boldsymbol{k_2} - \boldsymbol{k_1}$. ARPES data collected at $\boldsymbol{k_1}$ therefore sees the kink at $\omega = -\Omega_{\text{boson}}(\boldsymbol{q}) - \Delta(\boldsymbol{k_2})$ (c.f. Eq. 4.3). See Fig. A.2.

The band structure has been left out of the discussion up to this point. It would at first seem that including the band structure would place new constraints on the decay processes depicted in Fig. A.2, and the problem would become vastly more complex. However, in cuprates the phonon dispersion linewidths, though often sharp in energy, tend to be broad in momentum (which can be deduced from their energy widths by dividing by the dispersion slope) in comparison to the momentum ranges spanned by the electronic dispersion (in the nodal region) over the energy window of interest to phonon interactions. This seems to be true even over portions of the phonon dispersions where there is no significant "softening" [Reznik, 2010]. As a result, to a good approximation, the electronic band structure can be neglected in the problem at hand, and Fig. A.2 and Eq. 4.3 should do a good job of modeling the gap-shifting of the ARPES kink energy in the nodal region

[1] We are only talking about the boson excitation decay channel. Other interactions will of course give these states a finite lifetime.

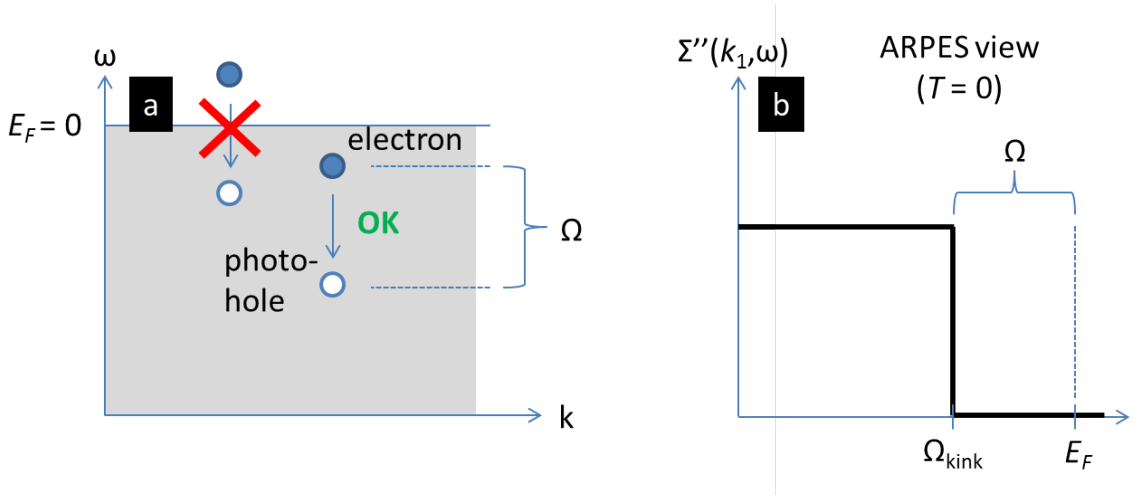

Figure A.1: Simple picture for the location of the ARPES kink. ARPES normally observes a kink due to an electron-boson interaction at an energy $\Omega_{\text{kink}} = -\Omega_{\text{boson}}$. (a) This occurs because photoholes at energy $\omega > -\Omega_{\text{boson}}$ cannot be annihilated by an electron decaying via emitting Ω_{boson}. However, this process can occur for $\omega < -\Omega_{\text{boson}}$. (b) As a result, $\Sigma''(\omega)$ has a step at $\Omega_{\text{kink}} = -\Omega_{\text{boson}}$.

of cuprates. On the downside, this line of reasoning implies that the inferred values of $\Omega^*_{\text{boson}}(\boldsymbol{q})$ in Ch. 4 perhaps have rather large error bars along the $\boldsymbol{q}$ axis. Fortunately, in Ch. 4 we are only interested in the overall qualitative character of $\Omega^*_{\text{boson}}(\boldsymbol{q})$, so this should not harm the analysis in too badly.

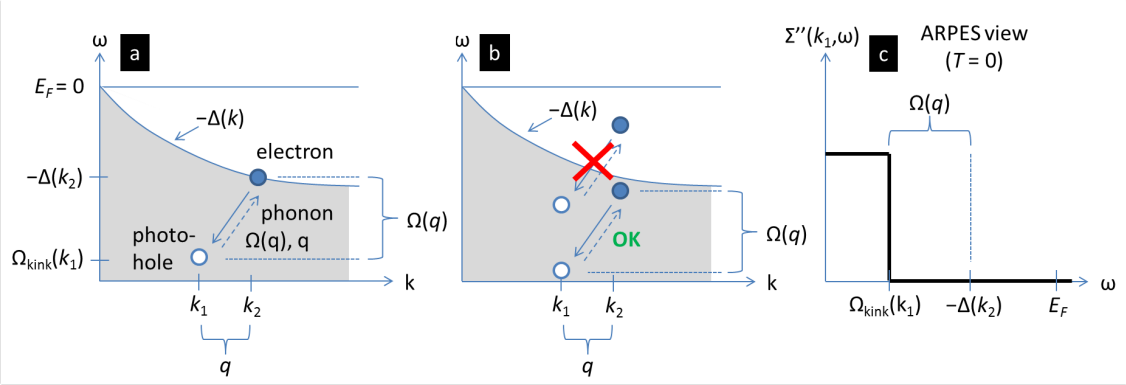

Figure A.2: ARPES kink location in the presence of an anisotropic gap. (a) The lowest-energy electron that can possibly decay to a hole at $\Omega_{\mathrm{kink}}(\boldsymbol{k_1})$ via boson emission $\Omega_{\mathrm{boson}}(\boldsymbol{q})$ is located at $\omega = -\Delta(\boldsymbol{k_2} = \boldsymbol{k_1} + \boldsymbol{q})$. (b) Other allowed and disallowed transitions. (c) Corresponding step in $\Sigma''(\boldsymbol{k_1}, \omega)$ at $\omega = -\Omega_{\mathrm{boson}}(\boldsymbol{q}) - \Delta(\boldsymbol{k_2})$.

Appendix B

Simulating the effects of energy resolution on the measured v_F

Prior to use of the the Richardson-Lucy image deconvolution technique in section 5.2.4, we attempted to account for the effects of resolution on the MDC-derived near-E_F dispersion by direct simulations of the spectra. Later on, when the RL technique was applied, these simulations provided an immediate indication that the results of the deconvolution were quite reasonable.

For the simulations in Fig. B.1, a Fermi liquid model of the underlying spectrum was used: $\Sigma_{\rm FL} = \alpha E + i[\gamma + \beta(E^2 + \pi^2 k_B^2 T^2)]$. This differs from the usual Fermi liquid equation only in that it includes an "impurity" scattering term γ to allow the possibility of finite broadening at E_F in the intrinsic spectrum. This form for the self-energy can be re-written in terms of the E-vs.-$\boldsymbol{k}$ spectral function as

$$A_{\rm FL}(\boldsymbol{k}, E) = Z \frac{\gamma' + \beta'(\omega^2 + \pi^2 k_B^2 T^2)}{[\omega - E'(\boldsymbol{k})]^2 + [\gamma' + \beta'(E^2 + \pi^2 k_B^2 T^2)]^2} \tag{B.1}$$

where $Z = 1/(\alpha - 1)$, $E'(\boldsymbol{k}) = ZE(\boldsymbol{k})$, $\beta' = Z\beta$, and $\gamma' = Z\gamma$ [Koralek, 2006].[1] For the simulation results shown here, the parameters are $\beta' = 5$, $\gamma' = 0.015$, and angular resolution (FWHM) of 0.2°. However, it was found the results were not particularly sensitive to these parameters, nor to the specific model of the self-energy — e.g., E vs. E^2 dependence of $\Sigma''(E)$.

[1] The quantity Z turns out to be the Fermi liquid "quasiparticle residue", which is related to the height of the step discontinuity at $\boldsymbol{k_F}$ in the energy-integrated density of states $n(\boldsymbol{k})$.

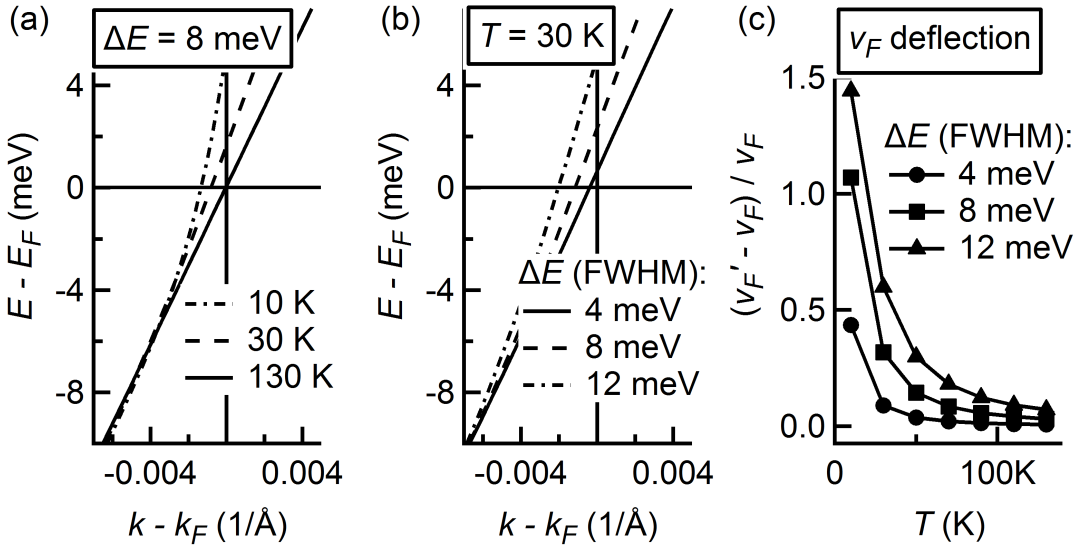

Figure B.1: Simulations of energy resolution effects on v_F. A two-dimensional intrinsic ARPES spectrum is simulated, then convolved with an energy and momentum resolution function, and finally analyzed with Lorentzian MDC fitting analysis. The model used for the simulations of the ARPES spectra is described in the text. The artificial deflection of the MDC peaks to low $|k|$ becomes more drastic as (a) the energy resolution is worsened or as (b) the temperature of the simulation is lowered. A correction factor $C = (v_F' - v_F)/v_F$ can be extracted from the simulations, where v_F' is the measured Fermi velocity, and v_F is the intrinsic value. The measured values of the Fermi velocity can then be corrected via $v_F = v_F'/[C(T) + 1]$. The "true" $v_F(T)$ values obtained from this type of correction agree well with the data in Fig. 5.6. Namely, v_F drops suddenly for temperatures below T_c.